A SEARCH FOR DOUBLE BETA DECAY IN ^{136}XE WITH A TIME PROJECTION CHAMBER

Thesis by

Henry Tsz-king Wong

in Partial Fulfillment of the Requirements

for the Degree of

Doctor of Philosophy

California Institute of Technology

Pasadena, California

1991

(Submitted September 27, 1990)

Acknowledgements

I would like to express special thanks to Professor Felix Boehm for his guidance, support, encouragement and help throughout the project. I wish to thank all my collaborators whose devotion and contributions to the experiment make this thesis possible. In particular, Dr. Zafar Iqbal and Mr. Herb Henrikson, both of whom I hold in deepest respect, have taught me much on experimental techniques, insights and tricks. Thanks also go to Professor Val Telegdi for stimulating ideas at the initial phase of the experiment, to Dr. Petr Vogel for enlightening discussions, to Mrs. Elsa Garcia for her superb secretarial assistance, and to Professor Jean-Luc Vuilleumier for his hospitality during my stay at the Institut de Physique of Neuchâtel.

I feel privileged and honoured to have received my higher education and scientific training in two of the finest academic institutions on Earth, Oxford and Caltech. I will cherish forever every single moment in learning about the Truth of Nature - and the Nature of Truth - from the most learned and august of scholars. I wish to acknowledge the financial support provided by the Hong Kong S.K. Lee Scholarship Foundation and by the California Institute of Technology during these periods.

I am indeed very fortunate to have a happy family and very good friends, who all believe in what I have been doing even though they cannot understand. To achieve is to honour them. I am forever grateful to my parents and brother for their love and support. My parents, through their real life examples, have shown me the single most significant quality needed in research - how to confront the unpleasant situations in life, and to confront them with dignity and grace. I worship them. Various friends have made my life enjoy-

able and stimulating during these years. I should particularly thank Dr. Tony Page and Mrs. Grace Lam who, through our regular correspondence, provide me with many healthy digressions and remind me of all the other important aspects of life besides, if not beyond, physics, from music and literature and philosophy to the joys and turmoils of parenthood. Finally and ultimately, I wish to express my heartfelt affection to Miss Judy Wu, and thank her, with her love, tenderness and faith, for bringing me much peace, comfort and joy.

Abstract

This thesis describes an experimental study of both the 0ν and 2ν double beta decay in ^{136}Xe with a Time Projection Chamber (TPC). The excellent track reconstruction capability of the TPC enables powerful background rejection. The construction and performance of the TPC, as well as the experimental features for background control are described. The TPC with its lead shielding has been installed in the Gotthard Tunnel Underground Laboratory in May 1990. Results from early background measurements using 5 atm of xenon depleted in ^{136}Xe are presented. Based on the background data, the projected sensitivities to the 0ν and 2ν modes with one year of run time in 60% enriched ^{136}Xe are 3.2×10^{23} years and 1.2×10^{21} years, respectively. Both numbers represent an order of magnitude improvements over previous experiments. Adopting the nuclear matrix elements from Vogel, the 0ν sensitivity implies a Majorana neutrino mass parameter of 4.5 eV.

我們注定要為一個什麼而燃燒，
我們要狠狠地愛一場，
只是，去愛什麼呢？
　　去為什麼而自焚呢？
為一個不存在的謊言？
抑或為一則確鑿的信仰？

張曉風「你還沒有愛過」

Destined are we to ignite ourselves
　　fervently for a something.
Destined are we to dedicate ourselves
　　passionately to a something.

Yet –

　To what do we devote ourselves,
　　body and soul?
　For what do we kindle ourselves,
　　to the whole?

For a pack of illusive lies –
　　Or for a well-founded faith?

Zhang Xiaofeng: "You Have Not Loved Yet"

CONTENTS

CHAPTER 1

OVERVIEW

1.1 Neutrino Physics

The existence of the neutrino was postulated by Pauli in 1930[1], and experimentally demonstrated by Reines and collaborators in 1956[2]. Since then, three flavors of neutrinos have been discovered, each with its own antiparticle. Recent results from the LEP experiments at CERN confirmed that there are exactly three flavors of light neutrinos[3]. Although our knowledge on the properties of neutrinos has improved substantially, there are still many open questions yet to be confronted by future research. A detailed discussion on the physics of neutrinos can be found in Ref. 4.

One of the open questions is related to neutrino mass. In the Minimal Standard Model of electroweak interaction[5], neutrinos are massless and purely left-handed. There are no neutrino mixings and each of the three lepton numbers is conserved. Therefore, observations of a neutrino mass or of neutrino mixings would clearly signify new physics beyond the Standard Model. At the sensitivity of present experiments, no such effects have been observed.

The question of neutrino mass also has cosmological and astrophysical consequences. The observed expansion rate of the Universe gives an upper limit to the average mass density, from which the constraint $\Sigma m_\nu < 100$ eV can be deduced, where the summation is over all flavors of light (< 1 MeV) neutrinos. Moreover, massive neutrinos may explain the Dark Matter problem and are crucial in the formation and development of the inhomogeneities in the Universe. Laboratory experiments aimed at determining the neutrino mass have

been going on for more than twenty years. Latest results from the kinematic measurements of the beta spectrum of ^{3}H indicate that the mass of $\bar{\nu}_e$ cannot exceed 10 eV[6]. Upper limits for the masses m_{ν_μ} and m_{ν_τ} are 0.25 MeV and 35 MeV, respectively. The neutrino bursts from supernova 1987a suggest that $m_{\nu_e} \leq 11 - 15$ eV, depending on specific models[7]. In addition, the various possibilities of neutrino mixings have been investigated experimentally. The Solar Neutrino Puzzle can be possibly explained in terms of neutrino flavor oscillations in vacuum or matter.

Besides neutrino mass, another pressing issue in neutrino physics is the question whether neutrinos are Dirac or Majorana particles. For neutral fermions such as neutrinos, the most general mass term that respects Lorentz invariance in the Lagrangian has two parts:

$$L_{mass} = L_D + L_M ,$$

in which the particles described by L_D are called Dirac neutrinos, which are different from their antiparticles, whereas those by L_M are Majorana neutrinos, which are identical to their antiparticles[8]. All experimental data obtained so far are consistent with the idea of a Dirac neutrino. However, the distinction between Dirac and Majorana neutrinos is important only if at least one neutrino has a finite mass. Most Grand Unified Theories do indeed favor massive Majorana neutrinos.

There is one process that is particularly suitable in distinguishing between the Dirac and Majorana properties of the neutrino, namely, neutrinoless double beta decay of a nucleus. Only if neutrinos are Majorana particles can the process of neutrinoless double beta decay occur. This process does not just indicate some fundamental properties of the neutrinos but also signifies lepton number violation. This thesis has as its goal to study double beta decay of the

nucleus ^{136}Xe and to enhance our knowledge of the mass and other properties of the neutrino.

1.2 Double Beta Decay

The possibility of nuclear double beta ($\beta\beta$) decay was first discussed by Wigner, while the first theoretical estimates were made by Goeppert-Mayer and Furry[9]. It is a process in which a nucleus (A,Z) decays spontaneously to a daughter nucleus (A,Z$\pm$2)[10]. While there are four different ways a nucleus may transfer two charge units (emission of two electrons, emission of two positrons, nuclear capture of two electrons, and capture of one electron with the emission of one positron), the two-electron emission has been investigated most extensively because this mode has the highest decay energies and thus the highest expected rates. Hereafter, "$\beta\beta$ decay" means specifically this transition.

The condition of lepton number conservation requires that the emission of two electrons is accompanied by the simultaneous emission of two antineutrinos. This process, referred to as "$2\nu\beta\beta$", is allowed by the Standard Model and thus expected to exist. On the other hand, if neutrinos are Majorana particles, a new, so far unobserved "$0\nu\beta\beta$" may be possible. This decay mode is characterized by the emission of two electrons without any neutrino.

In order for $\beta\beta$ decay to take place, the transition (A,Z)$\rightarrow$(A,Z+2) must be energetically allowed. To facilitate the experimental investigations, the ordinary beta decay (A,Z)$\rightarrow$(A,Z+1)+e^-+$\bar{\nu}_e$ must be energetically forbidden or strongly suppressed by spin and parity selection rules, so that $\beta\beta$ is the dom-

inant decay channel. The isobaric states of a typical $\beta\beta$ decay candidate are shown in Fig. 1.1. Such characteristic states are possible only if both (A,Z) and (A,Z+2) are even-even nuclei, so that $\beta\beta$ decays between ground states are all $0^+ \rightarrow 0^+$ transitions. Besides, if kinematically allowed, the parent nuclei can decay to the excited states of the daughters as well, giving rise to $\beta\beta$ $0^+ \rightarrow 1^+$ and $0^+ \rightarrow 2^+$ transitions.

1.2.1 Mechanisms

We now elaborate on the mechanisms that give rise to 2ν and 0ν $\beta\beta$ decay, as well as one of the several more speculative modes, $\beta\beta$ decay with the emission of a majoron.

1. *Two-neutrino mode ($2\nu\beta\beta$):* This is the transition with the emission of two electrons and two $\bar{\nu}_e$, as shown in Fig. 1.2a, that is,

$$(A, Z) \rightarrow (A, Z+2) + e_1^- + e_2^- + \bar{\nu}_{e_1} + \bar{\nu}_{e_2} .$$

   This is a second order weak interaction, allowed by the Standard Model. Lepton number is conserved in the process. The spectrum of the summed kinetic energies of the two electrons is continuous and peaked at about one-third of the transition energy, and is 0.8 MeV for the case of ^{136}Xe, as shown in Fig. 1.3.

2. *Zero-neutrino mode ($0\nu\beta\beta$):* The parent nucleus decays with the emission of only two electrons. A virtual neutrino is exchanged between the two nucleons, as shown in Fig. 1.2b, that is,

$$(A, Z) \rightarrow (A, Z+2) + e_1^- + e_2^- .$$

The summed energy spectrum is a delta function at the transition energy T_0, which is 2.48 MeV for ^{136}Xe, as shown in Fig. 1.3. In the Standard Model, a purely right-handed electron antineutrino is emitted in the first vertex, whereas the second vertex can only absorb a left-handed neutrino. Hence, the process can proceed only if neutrinos and antineutrinos are identical, that is, if neutrinos are Majorana particles. In addition, to account for the helicity mismatch between the emitted and absorbed neutrinos, either one of the following conditions must be satisfied:

(a) *Mass Mechanism:* There exists at least one neutrino with non-zero mass, so that it is a linear combination of two helicity states, with mixing amplitude of the admixture helicity state $\sim \frac{m_\nu}{E_\nu}$, where m_ν is the Majorana neutrino mass. This mechanism can only give rise to $0\nu\beta\beta$ $0^+ \rightarrow 0^+$ transitions.

(b) *Right-Handed Weak Couplings:* Weak interactions consist of both left and right-handed currents, so that the general Hamiltonian describing semileptonic weak interactions at low (below the W boson mass) energies can be expressed as

$$H_W = \frac{4G}{\sqrt{2}}\left[j_L^\mu(J_{L\mu}^\dagger + \kappa J_{R\mu}^\dagger) + j_R^\mu(\eta J_{L\mu}^\dagger + \lambda J_{R\mu}^\dagger)\right] + h.c.,$$

where

$$j_{R/L}^\mu = \frac{1}{2}\bar{\psi}_{\nu_e}\gamma^\mu(1 \pm \gamma^5)\psi_e\,, \text{ and}$$

$$J_{R/L}^\mu = \frac{1}{2}\bar{\psi}_u\gamma_\mu(1 \pm \gamma^5)\psi_d\,,$$

are the lepton and quark right/left-handed weak currents respectively. The fields ψ_x where $x = \nu, e, u, d$ describe the neutrinos, electrons, up and down quarks. The weak coupling constant G equals

$G_F \cos\theta_C$, where G_F is the Fermi constant and θ_C, the Cabbibo angle. Deviations from the Standard Model are parametrized by the dimensionless right-handed couplings κ, η, and λ. Moreover, this process also involves mixings of the emitted and absorbed neutrinos, which in turn requires the existence of at least one massive Majorana neutrino. This mechanism can lead to all the $0^+ \rightarrow 0^+$, 1^+, 2^+ transitions.

Therefore, both conditions require the existence of at least one massive Majorana neutrino as a necessary condition for the occurrence of $0\nu\beta\beta$ decay. Observations of the $0^+ \rightarrow 1^+$ or 2^+ channels also indicate weak interactions contain right-handed currents.

3. *Majoron mode ($\chi^0\beta\beta$):* This is the transition involving the emission of a neutral particle χ^0 called the majoron, together with the two electrons, as shown in Fig. 1.2c, that is,

$$(A, Z) \rightarrow (A, Z+2) + e_1^- + e_2^- + \chi^0 .$$

The summed energy spectrum of the electrons is continuous and peaked at about 2 MeV for ^{136}Xe, as shown in Fig. 1.3. The majoron is the massless Goldstone boson generated by the spontaneous breakdown of B−L (baryon number minus lepton number) symmetry[11], a process that produces the Majorana mass of the neutrinos. The conjecture for the existence of majoron was ruled out recently by the LEP experiments[3].

From the discussions above, it can be seen that there are strong motivations for the studies of $0\nu\beta\beta$, which offer a sensitive test for the Standard Model. Using the "*see-saw*" mechanism[12], many GUTs expect a light neutrino mass

$$m_\nu \sim \frac{(light\ lepton\ mass)^2}{M_{GUT}} ,$$

where M_{GUT} is the grand unification scale. The coming generation of $0\nu\beta\beta$ decay experiments may be sensitive to $m_\nu \sim 1$ eV, and for lepton mass $\sim 10^{-3} - 1$ GeV, these efforts should be able to probe physics on the scale of $10^3 - 10^9$ GeV, an energy range not accessible to accelerator experiments of the foreseeable future. The $2\nu\beta\beta$ decays, though allowed by the Standard Model, are also worthwhile for studies, because their lifetimes will give information on the nuclear structure, which in turn may help to interpret the measurements of the $0\nu\beta\beta$ experiments.

1.2.2 Transition Rates

The $0^+ \rightarrow 0^+$ transitions for $2\nu\beta\beta$ with transition energy T_0 have a rate given by[4]

$$\omega^{2\nu}_{\frac{1}{2}} = \left[T^{2\nu}_{\frac{1}{2}}(0^+ \rightarrow 0^+)\right]^{-1} = G^{2\nu}(T_0, Z)\left|M^{2\nu}_{GT} - \frac{g_V^2}{g_A^2} M^{2\nu}_F\right|,$$

where $G^{2\nu}(T_0, Z)$ is the leptons' four-body phase space factor, and the nuclear structure information is contained in the Gamow-Teller and Fermi matrix elements $M^{2\nu}_{GT}$ and $M^{2\nu}_F$, given by

$$M^{2\nu}_{GT} = \sum_n \frac{\langle 0^+_f | \sum_l \vec{\sigma}_l \tau^+_l | 1^+_n \rangle \langle 1^+_n | \sum_k \vec{\sigma}_k \tau^+_k | 0^+_i \rangle}{E_n - \frac{1}{2}(M_i + M_f)}, \text{ and}$$

$$M^{2\nu}_F = \sum_n \frac{\langle 0^+_f | \sum_l \tau^+_l | 1^+_n \rangle \langle 1^+_n | \sum_k \tau^+_k | 0^+_i \rangle}{E_n - \frac{1}{2}(M_i + M_f)},$$

where $|0^+_i\rangle(|0^+_f\rangle)$ is the 0^+ initial (final) nucleus with mass $M_i(M_f)$, and the $|1^+_n\rangle$s are the 1^+ states in the intermediate odd-odd nucleus with energies E_n.

Similarly, the decay rate for $0\nu\beta\beta$ transitions can be given by the general formula

$$\left[T^{0\nu}_{\frac{1}{2}}(0^+ \rightarrow 0^+)\right]^{-1} = C_1 \frac{\langle m_\nu \rangle^2}{m_e^2} + C_2 \langle \lambda \rangle \langle m_\nu \rangle m_e \cos\psi_1 + C_3 \langle \eta \rangle \langle m_\nu \rangle m_e \cos\psi_2$$

$$+C_4\langle\lambda\rangle^2 + C_5\langle\eta\rangle^2 + C_6\langle\lambda\rangle\langle\eta\rangle\cos(\psi_1 - \psi_2)\,.$$

Here ψ_1 and ψ_2 are the phase angles between the generally complex numbers m_ν and λ, and m_ν and η, respectively, whereas $\langle m_\nu\rangle$, $\langle\lambda\rangle$ and $\langle\eta\rangle$ are the effective parameters for the neutrino mass and right-handed coupling constants. For example, in the case of mass mechanism and CP invariance,

$$\langle m_\nu\rangle \;=\; \sum_{j=1}^{2N} \lambda_j^{CP} |U_{ej}^L|^2 m_j\,,$$

where λ_j^{CP} is the CP relative phase, and m_j the mass, of the Majorana neutrino mass eigenstate ϕ_j. The phases are equal to ± 1. In the special case of two mass degenerate Majorana neutrinos of opposite CP phases combining to form a Dirac neutrino, the cancellation between the two terms is exact.

The functions C_n contain the nuclear matrix elements and the phase space integrals. For instance, the mass mechanism term can be expressed as

$$C_1 \;=\; \left| M_{GT}^{0\nu} - \frac{g_V^2}{g_A^2} M_F^{0\nu} \right| G^{0\nu}(T_0, Z) m_e^2\,, \text{ in which}$$

$$M_{GT}^{0\nu} \;=\; \langle 0_f^+ | R \sum_{k,l} K_{k,l} \vec{\sigma}_k \cdot \vec{\sigma}_l \tau_k^+ \tau_l^+ | 0_i^+ \rangle\,, \text{ and}$$

$$M_F^{0\nu} \;=\; \langle 0_f^+ | R \sum_{k,l} K_{k,l} \tau_k^+ \tau_l^+ | 0_i^+ \rangle\,,$$

where R is the nuclear radius, and $K_{k,l} = H(\bar{E}, |\vec{r}_k - \vec{r}_l|)$. Here $\bar{E} = \langle E\rangle - \frac{1}{2}(M_i + M_f)$ where $\langle E\rangle$ is the "*typical*" excitation energy of the intermediate nucleus, and the function $H(\bar{E}, r)$, which characterizes the neutrino propagator, is given by

$$H(\bar{E}, r) \;=\; \frac{1}{4\pi} \int d^3\vec{k} \frac{e^{i\vec{k}\cdot\vec{r}}}{k(k + \bar{E})}\,.$$

The integral $G^{2\nu}$ varies with T_0^{11}, while $G^{0\nu}$ varies with T_0^5 (with the mass mechanism) or T_0^7 (with right-handed couplings), in the leading order, making

the lifetimes of the $\beta\beta$ decay isotopes extremely sensitive to the transition energies.

In the predictions of $\beta\beta$ decay rates, the phase space integrals are straightforward and can be evaluated exactly. The Fermi matrix elements $M_F^{2\nu}$ are negligibly small since they do not connect states of different isospins. The other matrix elements, however, are non-trivial and difficult to calculate. Various authors have done calculations[13] but their predictions do not agree. [See Appendix I for a brief description of the calculations performed by Engel, Vogel and Zirnbauer.] Table 1.1 gives the predictions for several $\beta\beta$ decay candidate isotopes that are under more intense experimental study. This problem is still under active research and certainly needs more input values from experiments.

1.2.3 Experimental Searches

Experimental searches for $\beta\beta$ decays can be dated as early as the 50's, but have received greater interest only in the past decade. These experiments can be classified crudely into three categories:

1. *Geochemical Experiments:* The total $\beta\beta$ decay lifetimes are determined by measuring the abundance of daughter isotopes, using advanced mass spectrometry, in an ore containing the parent. This technique has the advantage of long accumulation time ($\sim 10^9$ years), but cannot distinguish between the various modes. Besides, the lack of knowledge of the precise history of the sample is also a restriction. This method has been successfully applied to three cases (^{82}Se$\rightarrow^{82}$Kr, ^{128}Te$\rightarrow^{128}$Xe and ^{130}Te$\rightarrow^{130}$Xe)[14], where the daughters are noble gases. Positive results are reported in ^{82}Se ($T_{\frac{1}{2}}^{\beta\beta} = 1.3 \times 10^{20}$ yr) and ^{130}Te ($T_{\frac{1}{2}}^{\beta\beta} = 2.6 \times 10^{21}$

yr). The results are summarized in Table 1.2.

2. *Radiochemical Experiments:* Total $\beta\beta$ lifetimes are determined by counting the number of daughter isotopes accumulated in a known period of time in a sample of parent nuclei under laboratory conditions. The only experiment done is on the transition $^{238}\mathrm{U}\rightarrow^{238}\mathrm{Pu}$ with a limit of $T^{\beta\beta}_{\frac{1}{2}} > 6 \times 10^{18}$ years[15].

3. *Spectroscopic Experiments:* This category of experiments measures the energy of electrons emitted from the $\beta\beta$ decay isotopes and thus is able to distinguish between the various modes. A large range of techniques are adopted for these experiments. In spectroscopy experiments, like ^{76}Ge[16], very good energy resolution is achieved using germanium detectors. In track recognition experiments, like the Irvine Time Projection Chamber for ^{82}Se[17] (at present, ^{100}Mo is being measured[18]), $\beta\beta$ trajectories can be distinguished from single electron ones. In coincidence experiments[18] in ^{100}Mo, background rejection is achieved by sandwiching thin wafers of silicon detectors and foils of candidate isotopes. The only positive result published so far comes from the $2\nu\beta\beta$ mode of ^{82}Se[17], and gives $T^{2\nu}_{\frac{1}{2}} = 1.1 \times 10^{20}$ yr. Recent preliminary results from various ^{100}Mo experiments indicate a 2ν half-life on the order of 10^{18} years[18]. The measured half-life limits are tabulated in Table 1.2.

By far the most stringent limits for $0\nu\beta\beta$ decay are obtained from ^{76}Ge experiments. As an illustration to show the level of sensitivity, assuming CP invariance, (that is, $\psi_1 = \psi_2 = 0$) and adopting the set of matrix elements by Haxton and Stephenson, the most recent lifetime limit of $T^{0\nu}_{\frac{1}{2}} > 1.2 \times 10^{24}$ years for ^{76}Ge implies that $\langle m_\nu \rangle \leq 1.3$ eV, $|\langle \eta \rangle| \leq 0.23 \times 10^{-6}$, and $|\langle \lambda \rangle| \leq$

0.23×10^{-5}.

1.3 Time Projection Chamber

Based on the work of Charpak on Multiwire Proportional Chamber[19], and that of Allison on Multiwire Drift Chamber[20], the idea of the Time Projection Chamber (TPC)[21] was originated by Nygren at Berkeley in 1975 as a detector for PEP (positron electron project). The detector can perform track reconstruction for charged particles in three dimensions, and simultaneously identify them by measuring the ionization energies deposited along the trajectories. Track reconstruction can cover a large solid angle and is possible even in events with enormously high multiplicity. This wide range of capability earns it the name "bubble chamber of the 80s and 90s."

The general features of a TPC are shown in Fig. 1.4. Basically, a TPC is a cylindrical chamber filled with a detector gas that has high mobility and small attenuation for the drifting electrons. An electric field is applied in the axial direction so that when a charged particle passes through the gas and ionizes the atoms, the secondary electrons produced will drift along the axis of the cylinder towards the end cap. The field shaping rings ensure that the electric field is uniform throughout the active volume of the chamber. At the end, the secondary electrons undergo charge multiplication near a set of anode wires at positive high voltage. The field shaping wires (or strips) in between are at ground or low voltage to prevent cross-talks among the anodes, and to provide a high local electric field. The charge multiplication will then induce signals on an orthogonal set of readout pads (or wires) a few mm away.

Signals from anodes and pads will give information about two coordinates [(X,Y) or (r,rϕ)] of the tracks, whereas a start trigger signal together with the arrival timing of the pulses will give the z-coordinate (hence the name Time Projection Chamber). As a result, track reconstruction is achieved. The value dE/dx can be measured by considering the charge depositions along the tracks. In addition, a magnetic field is applied parallel to the drift field for most TPCs. This can reduce the diffusion of the drift electrons by keeping them in helical confinement. The curvature of the track will give the momentum of the particle. With information on both dE/dx and momentum, particle identification can be done readily.

TPCs have been applied to various experiments in particle and nuclear physics[22], a partial list of which includes:

1. central detectors in accelerator experiments such as ALEPH at LEP,

2. search for lepton number violating nuclear muon capture, the process $\mu^- + (A, Z) \rightarrow e^- + (A, Z)$, at TRIUMF.

3. measurement of very high statistics positron spectrum for normal muon decay at LAMPF,

4. $\beta\beta$ decay search in ^{82}Se at UC Irvine,

5. development of liquid argon TPCs, with possible applications as neutrino detectors and in proton decay searches.

Isotope	Klapdor[13]		Vogel[13]	
	$T_{\frac{1}{2}}^{2\nu}$ (yr)	$T_{\frac{1}{2}}^{0\nu}$ (yr)	$T_{\frac{1}{2}}^{2\nu}$ (yr)	$T_{\frac{1}{2}}^{0\nu}$ (yr)
^{76}Ge	3.0×10^{21}	2.3×10^{24}	1.3×10^{21}	9.2×10^{24}
^{82}Se	1.1×10^{20}	6.0×10^{23}	1.2×10^{20}	7.3×10^{24}
^{100}Mo	1.1×10^{18}	1.3×10^{24}	6.0×10^{18}	1.9×10^{24}
^{128}Te	2.6×10^{24}	7.8×10^{24}	5.5×10^{23}	1.8×10^{25}
^{130}Te	1.8×10^{21}	4.9×10^{23}	2.2×10^{20}	1.1×10^{24}
^{136}Xe	4.6×10^{21}	2.2×10^{24}	8.2×10^{20}	6.3×10^{24}

Table 1.1 Theoretical predictions of the 0ν and 2ν half-lives of several double beta decay candidate isotopes. The neutrino mass parameter $\langle m_\nu \rangle$ is assumed to be 1 eV in the calculations of $T_{\frac{1}{2}}^{0\nu}$.

Isotope	Spectroscopic Experiments		Geochemical Experiments
	$T_{\frac{1}{2}}^{0\nu}$ (yr)	$T_{\frac{1}{2}}^{2\nu}$ (yr)	$T_{\frac{1}{2}}^{0\nu+2\nu}$ (yr)
^{48}Ca	$> 2.0 \times 10^{21}$	$> 3.6 \times 10^{19}$	-
^{76}Ge	$> 1.2 \times 10^{24}$	$> 8 \times 10^{20}$	-
^{82}Se	$> 7 \times 10^{21}$	$(1.1 \pm^{0.8}_{0.3}) \times 10^{20}$	$(1.2 \pm 0.05) \times 10^{20}$
^{100}Mo	$> 4.0 \times 10^{21}$	($\sim 10^{18}$)	-
^{128}Te	-	-	$> 8 \times 10^{24}$
^{130}Te	-	-	$(2.6 \pm 0.3) \times 10^{21}$
^{136}Xe	$> 9 \times 10^{21}$	$> 8.4 \times 10^{19}$	-

Table 1.2 Experimental half-lives for some double beta decay candidate isotopes. The 2ν half-life for ^{100}Mo is only preliminary.

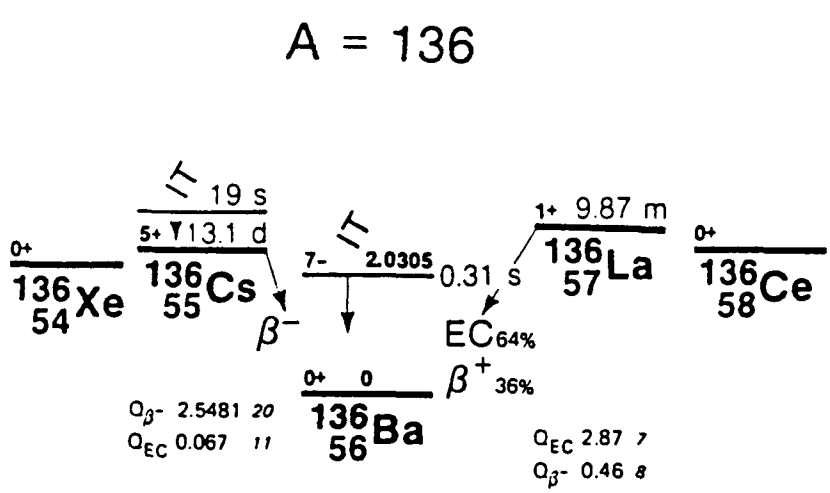

Figure 1.1 Isobaric nuclei with A=136. The isotopes ^{136}Xe and ^{136}Ce should have double beta decay as their dominant decay mode. For ^{136}Xe, $Q_{\beta-\beta-}$=2.481 MeV, whereas for ^{136}Ce, $Q_{\beta+\beta+}$=2.41 MeV.

a)

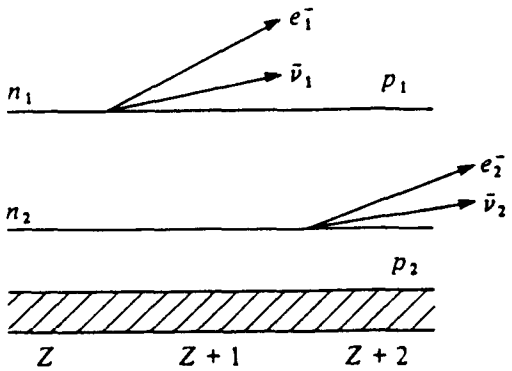

b)

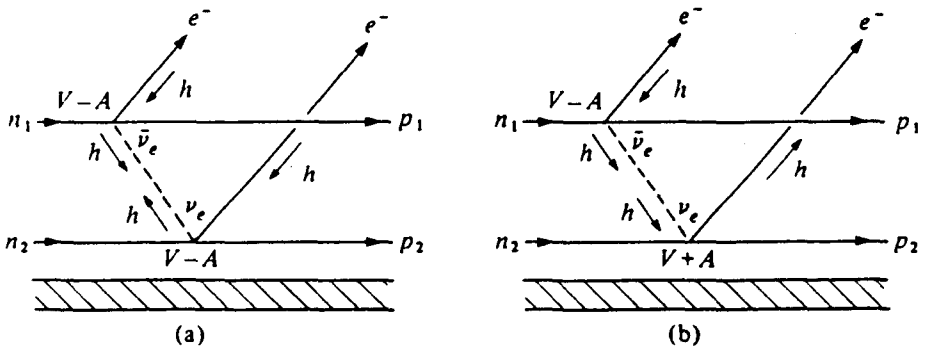

c)

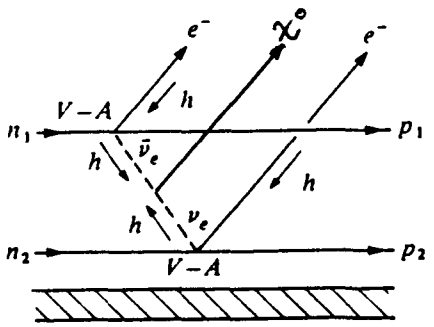

Figure 1.2 Schematic diagram for the various modes of double beta decay: (a) 2ν, (b.a) 0ν with the mass mechanism, (b.b) 0ν with the right-handed weak currents, and (c) 0ν with the emission of Majoron. The arrows labelled with 'h' represent the dominant neutrino helicities.

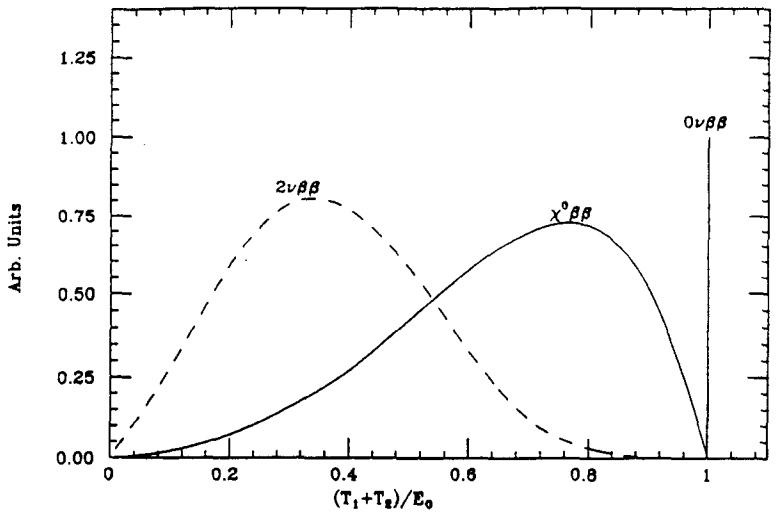

Figure 1.3 Typical spectra of the total kinetic energy of the two electrons emitted in the various modes of double beta decay. For ^{136}Xe, the transition energy E_0=2.481 MeV.

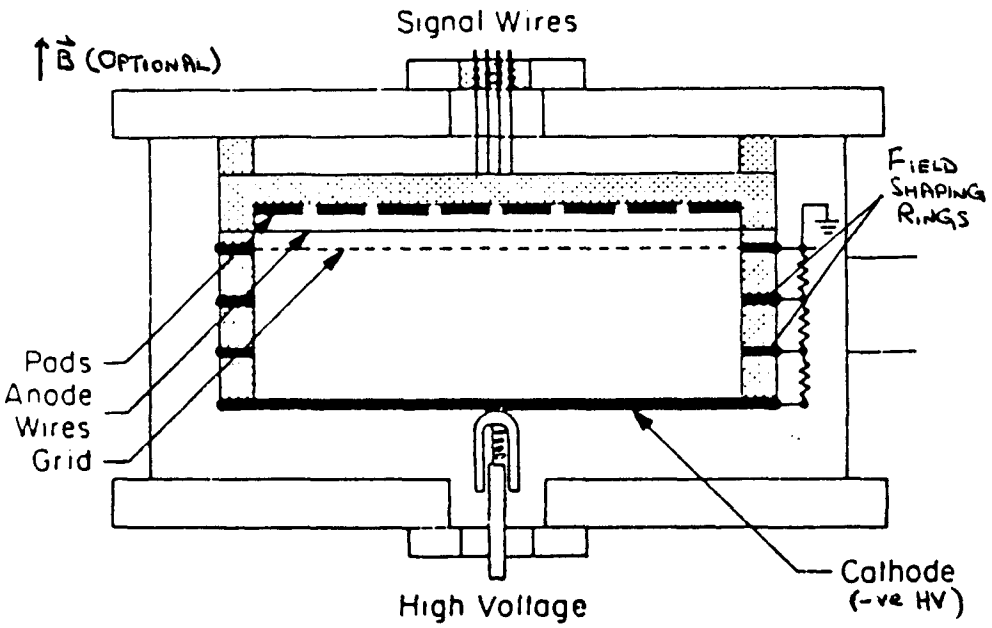

Figure 1.4 A schematic diagram showing the general features of a Time Projection Chamber.

CHAPTER 2

DOUBLE BETA DECAY IN ^{136}Xe

2.1 Motivations and Approach

The number of $\beta\beta$ decay candidate isotopes are very limited in nature.

There are several reasons why ^{136}Xe is a good case for experimental studies:

1. The natural isotopic abundance of ^{136}Xe is appreciable (8.87%). Furthermore, enriched xenon is commercially available in large quantities.

2. The transition energy T_0 for $\beta\beta$ decay of ^{136}Xe to ^{136}Ba is relatively large (2.48 MeV). This gives rise to a favorable phase space factor that enhances the decay rate.

3. Xenon is a good proportional counter gas and also possesses good electron drifting properties. Therefore it can act as both the source and the detector in a TPC.

The possibility of conducting a double beta search in ^{136}Xe was first investigated in 1976[23], with the use of a helium-xenon cloud chamber. In 1984, the Milano and Caltech groups independently proposed using a TPC to do the experiment[24]. Owing to its track reconstruction abilities, a TPC is an ideal device to study $\beta\beta$ decay in ^{136}Xe[25] (and indeed, in any proportional gas). A typical electron track from a TPC is given in Fig. 6.7a. It is minimum ionizing and relatively straight in the beginning, but has high charge depositions and undergoes large-angle scatterings near the end. Tracks like these can be differentiated easily from cosmic rays muons, which are straight, and alpha particles, which are short and with highly localized charge deposi-

tions, shown respectively in Figs. 6.11a and 6.10. Since the beginning of an electron trajectory differs drastically from the end, one can use this characteristic feature as a powerful background suppression of single electron tracks (due to beta decays, Compton scatterings, photoelectric emissions, etc.) from real $\beta\beta$ decay ones. A $\beta\beta$ event will be identified as a continuous trajectory with high charge depositions and large angle scatterings (that is, high second derivatives) at both ends.

2.2 Experimental Objectives

In order to perform a sensitive search for $\beta\beta$ decay in ^{136}Xe, the TPC must be capable of achieving three goals:

1. *Energy Resolution:* The total energy of the two electrons from $0\nu\beta\beta$ of ^{136}Xe is 2.48 MeV. In order to distinguish these events from background, a good energy resolution is crucial. The energy of an event is obtained by integrating the signals from the anode wires during the drift time (typically $\sim$60 μs). For most TPCs, each anode wire is independent, and so it gives information about one of the coordinates as well. In our case, all anode wires are connected together and the signal is fed to a single current-sensitive preamplifier. This scheme will lower the electronic noise and minimize the efforts and errors in calibrating hundreds of preamplifiers, with the trade-off of losing all position information. We consider a resolution of 5% at 2.5 MeV a realistic goal.

2. *Track Reconstruction:* Track reconstruction provides a powerful method of background suppression. Since all the anode wires are connected to-

gether, we will extract both the X and Y coordinates from a single readout plane. This is achieved by an orthogonal array of copper strips etched on a circuit board, as described in Sect. 3.3.3. Detailed Monte Carlo[26] studies have been done to simulate electron trajectories at high pressure xenon gas. The results indicate that a spatial resolution of about 10 mm is needed to resolve the structure of an electron track. The ultimate limit is about 2 mm due to the inevitable diffusion of the secondary electrons over the drift distance.

3. *dE/dx Measurement:* To distinguish single electron trajectories from $\beta\beta$ ones, measurements of dE/dx along the trajectories are necessary. A $\beta\beta$ event will be characterized by high charge depositions (or "*charge blobs*") and large second derivatives at both ends. Our Monte Carlo simulation suggests that, with 3 mm resolution in all directions, the charge deposited in the ends of a $\beta\beta$ track is at least four times larger than that along the track. This indicates that, with such resolution, a readout system of two threshold levels, instead of full digitization, should be able to distinguish the charge blobs with good efficiency. We have adopted such a two-level system and a spatial resolution of 3.5 mm in X and Y direction, although the design of the electronics is flexible enough to incorporate full digitization of the signals if necessary.

Besides building a high pressure xenon TPC that meets the requirements above, another important challenge of the experiment is to have proper control and understanding of the background. The chamber has been built with known low background materials and shielded by lead and copper, while the experiment is being conducted in the Gotthard Tunnel Underground Laboratory. Xenon enriched to 62% ^{136}Xe has been purchased to increase the source size.

Anticipating a control experiment, xenon depleted in ^{136}Xe (the by-product of the isotopic separation) is also obtained.

The experimental efforts are shared by a collaboration of three institutions: Caltech, University of Neuchâtel and the Paul Scherrer Institute (PSI, formerly SIN). The physics objective is to reach a lifetime sensitivity of at least 10^{23} years in one year of run time, which corresponds to a sensitivity of the parameter $\langle m_\nu \rangle$ at the level of a few eV.

2.3 Other ^{136}Xe Experiments

Besides the Caltech TPC, $\beta\beta$ decay in ^{136}Xe is also being investigated experimentally by several groups. A brief description of their experiments and current results is summarized below:

1. *High Pressure Ionization Chamber:* A Moscow group has built a high pressure xenon ionization chamber[27] to look for $\beta\beta$ decay of ^{136}Xe at the Baksan Neutrino Observatory. The chamber has an active volume of 3.14 l and is filled with 93% enriched ^{136}Xe to 25 atm, with an admixture of 0.8% H_2 to increase the electron drift velocity. The energy resolution is 3.8% at 2.5 MeV. The limits obtained, with 700 hours of run time, are $T^{2\nu}_{\frac{1}{2}} > 8.4 \times 10^{19}$y and $T^{0\nu}_{\frac{1}{2}} > 3.3 \times 10^{21}$y.

2. *Multi-element Proportional Chamber:* The Milano group has built a multi-element proportional chamber[28] with 61 proportional cells, hexagonal in cross-section. It is operating at 10 atm with 64% enriched ^{136}Xe and a fiducial volume of 45 l, in the Gran Sasso Underground Laboratory. Some background rejection is achieved by requiring that at least

three and less than nine adjacent cells are triggered by the same event. The energy resolution is 5% at 2.5 MeV. The half-life limit obtained to date is $T^{0\nu}_{\frac{1}{2}} > 2.0 \times 10^{22}$ yr at 90% confidence level.

3. *Liquid Xenon Ionization Chamber:* Several groups are currently developing liquid xenon ionization chambers[29]. The main motivation is for applications in gamma ray astronomy, but they can also be used as double beta decay experiments. The best energy resolution achieved so far is 6% at 569 keV.

CHAPTER 3

DESIGN AND CONSTRUCTION

In this and the following chapters, we discuss the design and development of the hardware, electronics and software components of the TPC. Starting in summer 1985 at Caltech, this was a joint effort in which H. Henrikson, M.Z. Iqbal, B.M. O'Callaghan, J. Thomas and myself have played a major role. In summer 1988, the experiment was moved to Neuchâtel, and I was joined by P. Fisher, L. Mitchell, M. Treichel and J.-C. Vuilleumier to continue the efforts. The experiment was installed at the Gotthard Tunnel Underground Laboratory in March, 1990. I have been involved directly and indirectly in all aspects of the experiment. My major contributions include the CAMAC modules, trigger system, data acquisition and analysis software, tests and measurements during the development phase, as well as maintenance and data taking at Gotthard after the experiment was installed there.

3.1 Preliminary Studies

In order to determine the various design features and parameters of the Time Projection Chamber for the search of double beta decay in ^{136}Xe, a prototype chamber has been built and Monte Carlo programs have been developed. Details of both studies can be found in Ref. 30. This section summarizes the results of the studies.

3.1.1 Prototype TPC

A 16-channel TPC of 1 liter in volume has been constructed[31] to investigate the performance of the device as well as the design of the final version. The general scheme of the hardware, gas handling system and readout electronics was developed.

One of the main questions addressed with the prototype has to do with the scintillating property of xenon gas. The initial plans were to make use of the scintillation light created by the ionizing particles as a time-zero trigger. However, it was found that pure xenon is not suitable as the fill gas for the TPC for various reasons described in the discussion of gas composition in Section 3.2.7. It was decided that xenon with an admixture of 4% CH_4 is to be used. The disadvantage of this is the absence of a time-zero trigger for the experiment, that is, there is no absolute Z measurement for the events.

3.1.2 Monte Carlo Simulations

Extensive Monte Carlo programs are developed[26] to determine some of the design parameters of the experiment. The programs simulate electron trajectories in a gaseous medium, the Physics ingredients of which are the Molière theory of multiple scattering[32] for angular deflection of the electrons, the Bethe-Bloch[33] formula for their dE/dx due to ionization, and bremsstrahlung cross section formulae[34] for the dE/dx due to radiation. Details of the studies on delta (or "knock-on") electrons and bremsstrahlung effects are given in Appendix 2. The results of the Monte Carlo studies will be described in the relevant discussions in Section 3.2.

3.2 Design Parameters

3.2.1 Pressure

Among the primary requirements for a successful double beta decay experiment with a xenon TPC are large source size (several moles of candidate nuclei) and good detection efficiency. These requirements suggest that the experiment should be carried out at high pressure. However, at higher pressure the electron tracks are shorter. Since spatial resolution is primarily limited by diffusion of the drifting electrons, some trajectory and dE/dx information is lost for shorter tracks. In addition, other practical considerations limit the pressure to less than 10 atm: at higher pressures the attenuation of the drifting electrons by electronegative contaminants, which varies with the square of pressure, becomes more serious; and the higher voltages required for drift field and for proportional multiplication become more difficult to handle. To optimize various requirements, a working pressure of 5 atm has been chosen. However, the design of the chamber allows the pressure to be increased to 10 atm, should that be desirable.

The operating pressure of 5-10 atm suggests that the application of an external magnetic field is not very useful for the experiment. A $\sim$1 MeV electron undergoes a lot of multiple scattering along its course. This makes the measurement of its energy with a magnetic field impossible, and the event vertex recognition inefficient. Besides, this involves other experimental complications. A large B-field (several kG) is needed; spatial resolution has to be better; track reconstruction is even more difficult; and the $\vec{E} \times \vec{B}$ effects[35] will smear out the trajectories along the anode wires. Consequently, it has been decided that the experiment is to be conducted without an external magnetic field.

3.2.2 Volume

Once the operating pressure is chosen to be 5 atm, considerations of construction difficulties and detection efficiency will determine the volume of the chamber. A cylindrical active volume of 60 cm in diameter and 70 cm in height has been chosen. With this geometry, Monte Carlo studies show that the detection efficiency of $0\nu\beta\beta$ events in 5 atm of xenon gas is 25% (33% of the events are completely enclosed, 24% of which have radiation loss due to bremsstrahlung). Therefore, with an admixture of 4% methane, the fiducial number of xenon atoms is about 6.7×10^{24} or 11.1 moles, corresponding to 4×10^{24} ^{136}Xe in the case of 62% isotopic enrichment.

For comparison, at a pressure of 10 atm, the detection efficiency is 53% (65% enclosed events, 18% of which have radiation loss). The variation of efficiency with pressure and energy for both $\beta\beta$ and single electron events is shown in Figs. 3.1 and 3.2, respectively. It should be noted that at higher pressure, the rate of background (single electron) events also increases, and their rejection is more difficult since the tracks are shorter.

3.2.3 Spatial Resolution

The spatial resolution is 3.6 mm in the X and Y, and about 2 mm in the Z (drift) direction, at a clock frequency of 8 MHz and drift velocity of $\sim$ 1.5 cm μs^{-1}. The spatial resolution is limited by the diffusion of the drifting electrons, which is about 2 mm for a drift distance of 70 cm at some realistic field strength[36]. From Monte Carlo studies, with a spatial resolution of 3 mm in all three directions, a rejection efficiency of 95% for single electron events at

2.5 MeV in 5 atm of xenon is possible, by summing up and comparing charge depositions at both ends of the trajectories, as shown in Figs. 3.3a and 3.3b.

3.2.4. Energy Resolution

From measurements using a Multiple Wire Proportional Chamber (MWPC)[37], with comparable wire spacings and lengths to the TPC, the main contribution to the energy resolution is caused by the gain variation between different wires ($\sim$4%). Therefore, we choose 5% at 2.5 MeV as the goal for the energy resolution of the TPC. At this resolution, the Compton edge (2381 keV) and the photoelectron peak (2614 keV) of the ^{208}Tl gamma rays are outside the range $T_0 \pm \frac{1}{2}FWHM$ (the photo-peak is even above $T_0 + FWHM$) where T_0=2481 keV. Consequently, one expects that the γ-induced events due to ^{208}Tl will not contribute significantly to the background in the 0ν energy region.

From extensive studies and measurements with various anode systems, we learn that in order to achieve good energy resolution, that is, uniform charge multiplication, the following requirements must be met:

1. Good geometrical precision is crucial for the anode system, details of which are described in Section 3.3.2. Our goal is a tolerance of $< 25\,\mu$m for the wire spacings, and the grid-anode plane-readout pad separation.

2. All insulators (like the edge of the mounting frame for the anode) must be at least 1 cm away from the effective measuring area of the TPC, since their presence suppresses the charge multiplication over a length scale of 1 cm.

3. All wires used in the anode system must be clean.

4. Surfaces between high voltage fine wires and ground must be smooth and clean, and the separation maximized, to avoid leakage currents.

5. All wires must be tensioned (> 70 g) to prevent oscillation and vibration when the high voltage is applied to the anode wires.

6. The charge multiplication should be kept low at a 10^3 - 10^4 level, to maximize the dynamic range on linear response, and to minimize space charge effects.

7. Electronegative contaminants in the gas shoul be kept below a 0.2 ppm level.

Quantitative studies of the changes in proportional gain with various parameters are described in detail in Ref. 30.

3.2.5 Proportional Multiplication

To maximize the dynamic range of linear response in charge multiplication (that is, to minimize space charge effects due to positive ions), the multiplication factor should be kept low, but nevertheless sufficient to induce reasonable signals on the XY readout pads. A multiplication of 10^3-10^4 is adequate. This corresponds to an anode voltage of less than 3 kV at 5 atm in the anode system described in Section 3.3.2.

3.2.6 Electric Field Strength

In most TPCs, a large drift field is necessary to increase the drift velocity of the secondary electrons and hence allow a higher trigger rate. This is not

crucial in this experiment because of the expected low count rate (a few per second). However, the diffusion of the drifting electrons can be serious at low drift velocities. An acceptable drift velocity of 1 cm μs^{-1} and diffusion of 2 mm over 70 cm drift distance at 5 atm will require a voltage of about 70 kV (that is, about 200 V cm^{-1} atm^{-1}) at the cathode.

The electric field in the chamber must be uniform to ensure that all secondary electrons drift parallel to the axis and at constant velocity. This can be achieved by layers of field shaping rings, which define the active volume of the chamber. Calculations based on relaxation techniques[38] have been made to investigate the geometry of the rings. The design criteria is that the trajectory distortion is smaller than the maximum diffusion width of 2 mm.

3.2.7 Gas Composition

From the studies with the prototype system, it has been concluded that pure xenon is not suitable for the experiment[31]. A quenching gas must be added to reduce electron diffusion, increase drift velocity, absorb the UV scintillations from xenon and enhance stability against high voltage breakdown. The quenching gas used is methane (CH_4) at a ratio of 4%. With this composition, the drift velocity increases by an order of magnitude to $\sim$1 cm μs^{-1} at an electric field of $\sim$200 $Vcm^{-1}atm^{-1}$, while the diffusion is suppressed by a factor of 10, as shown in Figs. 3.4a and 3.4b.

3.2.8 Gas Purification

Traces of electronegative contaminants (especially oxygen) can attenuate

the electron drifting in xenon, through the process:

$$e^- + O_2 \rightarrow O_2^{*-},$$

The details of electron attachment to oxygen are discussed in Appendix 3.

To keep the attenuation below 5% at 5 atm over a drift distance of 70 cm, oxygen contaminations must be below 0.2 ppm level. However, oxygen is continuously "*outgassed*" from various components inside the chamber and so continuous purification is necessary. An additional requirement for the purification system is that it should not affect the methane concentration.

3.2.9 Calibration and Monitor

We anticipate a vertical muon rate of a few per day in the Tunnel, and these events are saved for various calibration purposes. The length of the muon signal indicates the time taken by the secondary electrons to drift from the cathode to the anode (a length of 70 cm). This gives an on-line monitor for the drift velocity and hence the compositions of the gas. In addition, the slope of the anode signals for such vertical muon events is also a quantitative measure of the gas purity. A gas degraded by electronegative contaminants will give muons whose signals are attenuated with increasing drift length.

The energy spectrum is calibrated by putting gamma sources near the chamber at regular intervals. The dE/dx values for the minimum ionizing muons provide an on-line monitor. The pressure, temperature, and various trigger rates are also recorded. The trigger rates are sensitive measures of the stability of the system with time. The various procedures of monitoring the stability of the TPC are discussed in more detail in Section 6.3.

3.3 Descriptions of Hardware

The schematic diagram of the TPC together with the shielding, and the associated gas handling and purification systems are shown in Fig. 3.5. The various components[39] are described below.

3.3.1 Main Chamber

The main chamber of the TPC is a cylindrical OFHC (Oxygen Free High Conductivity) copper vessel (dealer: Mac Kellar Materials Co., Los Angeles) of 72.9 cm diameter, 78.7 cm height and 5.3 cm wall thickness, weighing 1 ton. The vessel is designed to withstand a pressure of 15 atm. The lower cover contains the high voltage feedthrough to the cathode, while the readout pad and the anode system are mounted from the top cover. The chamber is connected to the gas handling system by two right-angled fittings, to prevent direct illumination of background gamma rays from outside. There are four view-ports on the side for calibration and various purposes.

3.3.2 Anode System

Two anode systems have been built to learn about the requirements involved and to optimize various parameters, and they are described in Ref. 30. The geometry of the final anode system is shown in Fig. 3.6a.

All the wires are made of gold-plated tungsten. The anode and grid wires are 20 μm in diameter and under about 70 g of tension (breaking tension about 100 g), whereas the field wires are 50 μm in diameter and under about 90 g of

tension. The anode wires are separated by 5 mm spacing. In between adjacent anode wires are the field wires that are grounded to enhance proportional multiplication, to collect the positive ions produced, and to localize electrostatic induction to those XY channels directly facing the point of multiplication. The readout pad and the grid wires plane are separated from the anode/field wires plane by 3.5 mm. The grid wires are orthogonal to the anode/field wires direction. Their purposes is to isolate the anode system from the drift region, and to collect the positive ions produced in multiplication. The tolerance for all the separations mentioned above is 25 μm.

The mounting frame (manufacturer: Stesalit, Switzerland) is constructed by moulding a low background epoxy (Aradit AW 103) to a copper ring. The design is shown in Fig 3.6b. All the wires are soldered on the copper strips glued on to the epoxy. Stainless steel pins attached to the strips define the alignment of the wires. The surface distance from an anode wire to the adjacent field and grid wires is increased by machining away the epoxy around the copper strips. The solder is covered with epoxy to provide further electrical shielding. Copper rings at the perimeter provide an additional anchor and connect the wires together electrically.

The anode wires are connected together to a single current sensitive preamplifier outside the chamber. The field wires and grid wires are grounded externally, so that one can remove the terminator to look at the signals induced, or to apply some voltage to optimize the field.

3.3.3 Readout System

The design of the XY readout system is shown in Fig. 3.7. The XY

strips pattern is etched on one side of a Rexolite board (Rexolite 1422, Oak Materials Group Inc.). An identical pattern, shifted by half a unit in both X and Y directions, is etched on the other side of the board. The holes are plated-through to make the channels continuous. Adjacent channels are separated by 3.6 mm, and the pattern fills up a circle 60 cm in diameter, giving a total of 336 channels, that is, 168 channels in each of X and Y axes. The entire pattern consists of about 45000 holes. To ensure that each of these holes is properly connected, the capacitance of the channel is measured. The capacitance varies with the length of the channel, so that an anomalously high capacitance indicates the channel is shorted to some other ones, whereas a low value signifies that the channel is broken.

The circuit board is the largest grounded surface near the high voltage anode wires. Therefore, it has to be made flat to provide uniform charge multiplication across the entire anode plane. To achieve this, a "honey-comb" structure made of Delrin (Delrin is the Dupont trade name of a standard acetal) is sandwiched between the circuit board and another OFHC copper sheet. The assembly is held together by a low-background high-vacuum epoxy (Shell 826 epon resin and Versamid 140 polyamide resin). The circuit board is flattened to within 25 μm with this assembly.

3.3.4 Cathode and Field-Shaping Rings

The cathode is a thin (1.6 mm) OFHC plate, 63 cm in diameter. Its perimeter is curled (that is, no sharp edge) to hold a higher voltage without discharging to the chamber wall. The field-shaping rings are also made of OFHC, also 1.6 mm in thickness. There are 70 of those, with adjacent ones

separated by 1 cm, and connected by 10 MΩ resistors. The rings and the cathode are supported by six Delrin poles resting on the bottom cover.

The cathode voltage (Spellman RHR 100*100) is applied through a high frequency RC filter to the high voltage feedthrough at the bottom cover. The filter consists of two stages, with R=1 MΩ and C= 750 pF, and attenuates the 50 kHz ripple by 98%.

3.3.5 Veto System

The XY readout strips are surrounded by a 2 mm copper ring (the "veto ring") which defines the radius of the measuring area. When a trajectory leaves the active volume of the TPC through the field shaping ring assembly, or enters it from outside, signals will be induced in the veto ring, and thus can be used to veto the event. Details concerning the processing of the veto and trigger signals will be discussed in Chapter 4. However, events starting or terminatin on the XY pad or the cathode cannot be vetoed.

During the test runs at Caltech, an additional liquid scintillator panel is placed on top of the chamber, to reject events caused by cosmic rays. This is not necessary in the Tunnel where the muon flux is reduced by a factor of 2×10^5.

3.3.6 Gas Handling System

The schematic diagram of the gas handling system is shown in Fig. 3.8. It consists of a gas manifold connected to a turbomolecular pump, pressure gauges, cylinders of xenon-methane and argon-methane, and a gas circulation

pump and purifier. The whole chamber is pumped down to vacuum before the fill gas is introduced.

Xenon is an expensive gas (even more so for enriched xenon), and so a two-stage recovery system is built. The main recovery tank is cooled down to liquid nitrogen temperature (77 K), and will absorb most of the xenon (m.p. 166 K) in the chamber when the valve is opened. With 1800 liters of gas to be recovered, this process will typically stop at about 0.5 atm. This is due to the vapour pressure substained in the recovery tank. The rest of the gas is then recovered by the absorption pump, also at liquid nitrogen temperature. The absorption pump is then warmed up and the evaporating gas is forced to the main recovery tank. These procedures are typically repeated three or four times until no more gas is absorbed. The final pressure reached can be as low as 10^{-3} atm, equivalent to less than half a liter of gas at STP.

As explained in Section 3.2.8, continuous purification of the xenon-methane mixture is necessary. The gas is circulated through a getter material with a piston pump driven by a magnet (Nitto Air Compressor AC0102). For safety, the pump is housed in another pressure vessel also filled with xenon, so that there is no moving seal. The getter must be able to remove oxygen and water while keeping methane intact. We have found two getter materials that suit these requirements: 1) the "HYDROX" (Matheson Hydrox Purifier Model 8301) - an alloy of zirconium, titanium and nickel operating at 500 °C; 2) the "OXISORB" and "HUMISORB" (Messer Griesheim GmbH, Oxisorb Gas Purifier System), which operates at room temperature. However, from measurements described in detail in Section 6.4, it is found that the OXISORB cartridges have an enormous rate of radon emission. Therefore, the HYDROX is used during data taking.

3.3.7 Enriched and Depleted Xenon

During the development and testing phase, natural xenon is used. To increase the source size during data taking, xenon enriched with 62% ^{136}Xe is purchased from Monsanto Research Corporation (Mound, Oak Ridge), where isotopic separation is done with a centrifuge plant. The amount is 1800 STP liters at a cost of US$ 125 per liter. In addition, the by-product of the separation, xenon depleted in ^{136}Xe is also obtained, at a cost of US$ 5 per liter. The depleted xenon will be used as a control measurement for further background identification and rejection.

3.3.8 Shielding

The active volume of the TPC is shielded by the chamber itself (5.3 cm copper). There are 30 cm of lead (from a Swedish mine, vendor: Scheller, Zürich) surrounding the chamber in an octagonal layout, and this will attenuate the gamma flux at 2.5 MeV by a factor of 10^7. The schematic diagram of the shielding is shown in Fig. 3.9. The entire "lead house" weighs about 18 tons, and rests on a stainless steel plate 3 cm in thickness. In the initial phase, 20 cm of the lead shielding is installed.

The shielding is equipped with a calibration port through which a gamma source can be inserted for the purpose of energy calibration. Two plastic scintillators are placed on the top and bottom of the house. Coincidence signals from the scintillators provide triggers for vertical muons, used for monitoring the drift velocity, and therefore the gas composition. The electronics and the gas handling system are all outside the shielding. The top part consists of

two semi-circular discs each with 20 cm of lead on a copper plate, and can be moved sideways when the chamber has to be opened. Two similar plates with 10 cm of lead will be added at a later stage. All the cables and gas pipes are bent through right angles before connecting to the main chamber, to prevent direct illumination of the background gamma rays.

Ultimately, the entire shielding will be surrounded by a radon shield, which is a thin sheet of aluminium. The volume inside will be slightly pressurized by dry nitrogen to prevent radioactive radon gas from diffusing in. A hole is dug in the ground directly facing the high voltage feedthrough at the bottom, and is filled up with lead bricks.

a)

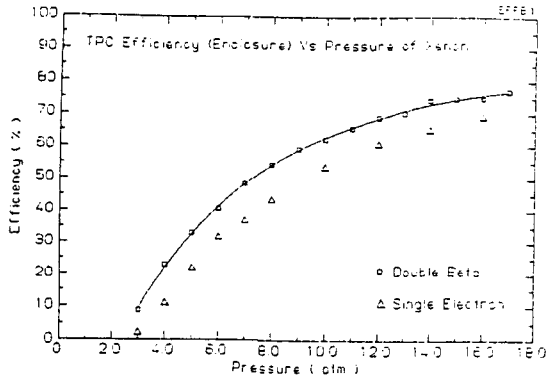

b)

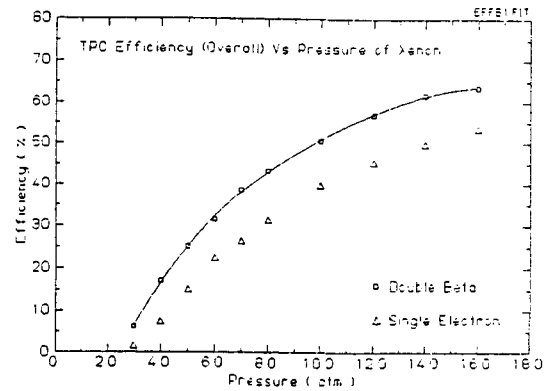

c)

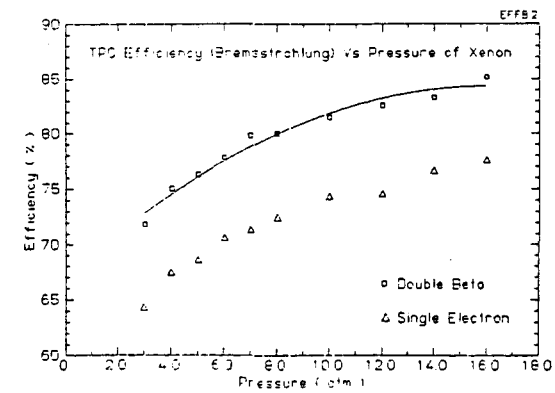

Figure 3.1 Results from Monte Carlo simulations, showing the variations of TPC efficiencies against the pressure of xenon: (a) efficiencies of trajectories being completely enclosed, (b) efficiencies of all the photons emitted through bremsstrahlung being enclosed, and (c) net efficiencies. The transition energy is 2.5 MeV. The continuous line is a fit to double beta decay efficiencies.

a)

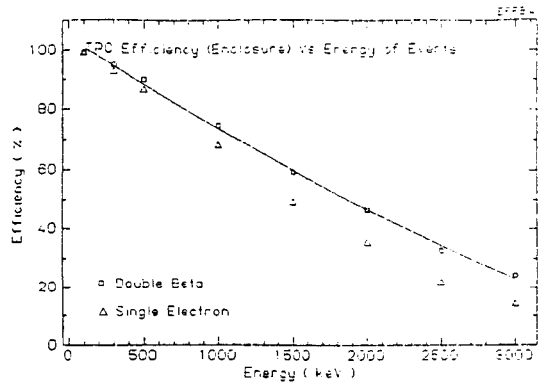

b)

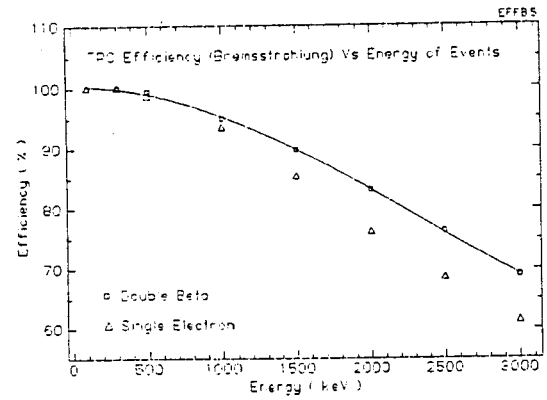

c)

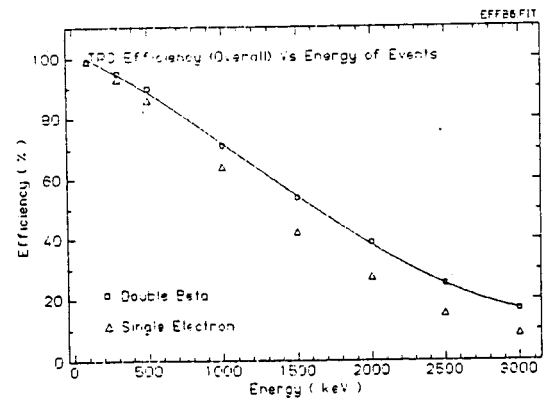

Figure 3.2 Results from Monte Carlo simulations, showing the variations of TPC efficiencies against the transition energies of the events: (a) efficiencies of trajectories being completely enclosed, (b) efficiencies of all the photons emitted through bremsstrahlung being enclosed, and (c) net efficiencies. The pressure of xenon is 5 atm. The continuous line is a fit to double beta decay efficiencies.

a)

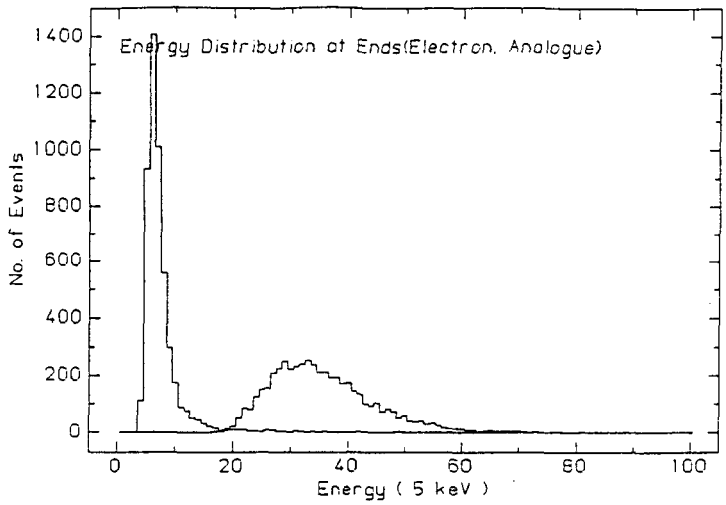

b)

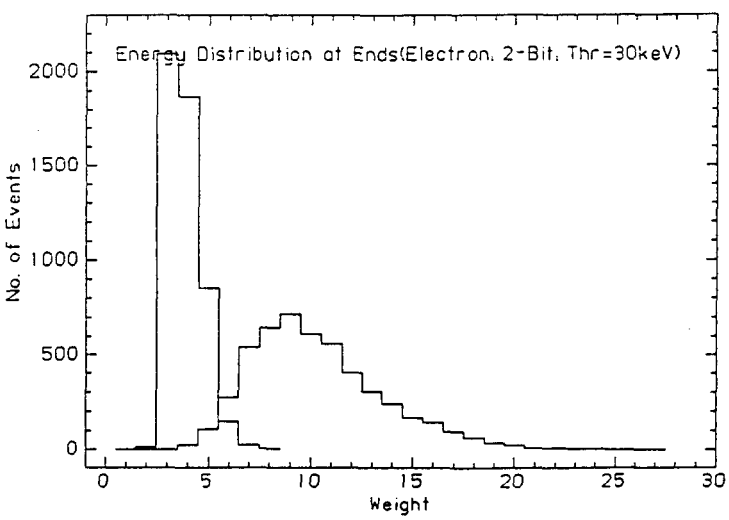

Figure 3.3 Results from Monte Carlo simulations, showing the charge depositions at the beginning and end of 2.5 MeV single electron trajectories in 5 atm of xenon. The sampling volume is $1.5 \times 1.5 \times 1.5$ cm^3, divided into 125 unit cells, and centered at the beginning/end of the tracks. Graph (a) shows the total charge depositions, as if analogue electronics are used, whereas (b) shows the histograms of a 2-bit digitization system, with a threshold per unit cell of 30 keV, and the weights of "tracks" and "blobs" being 1 and 2 respectively.

a)

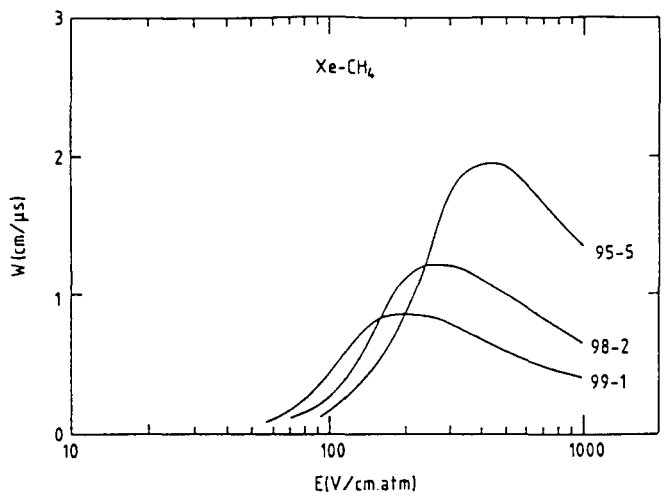

b)

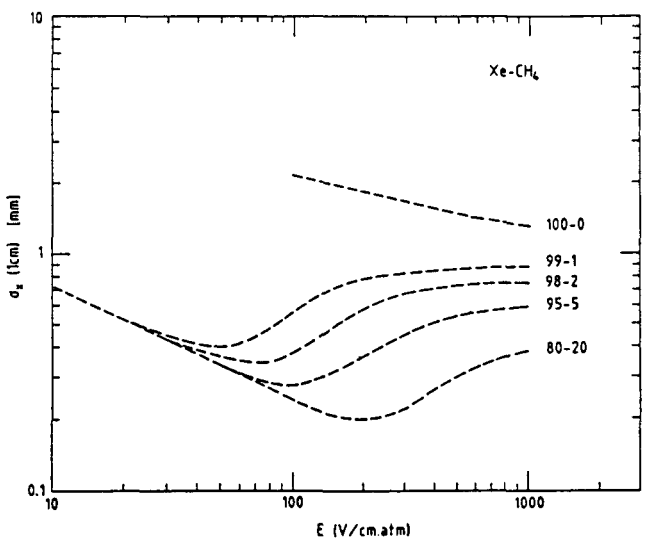

Figure 3.4 (a) Drift velocity of electrons versus drift field, at various xenon-methane compositions. (b) Diffusion of drifting electrons versus drift field, at various xenon-methane compositions.

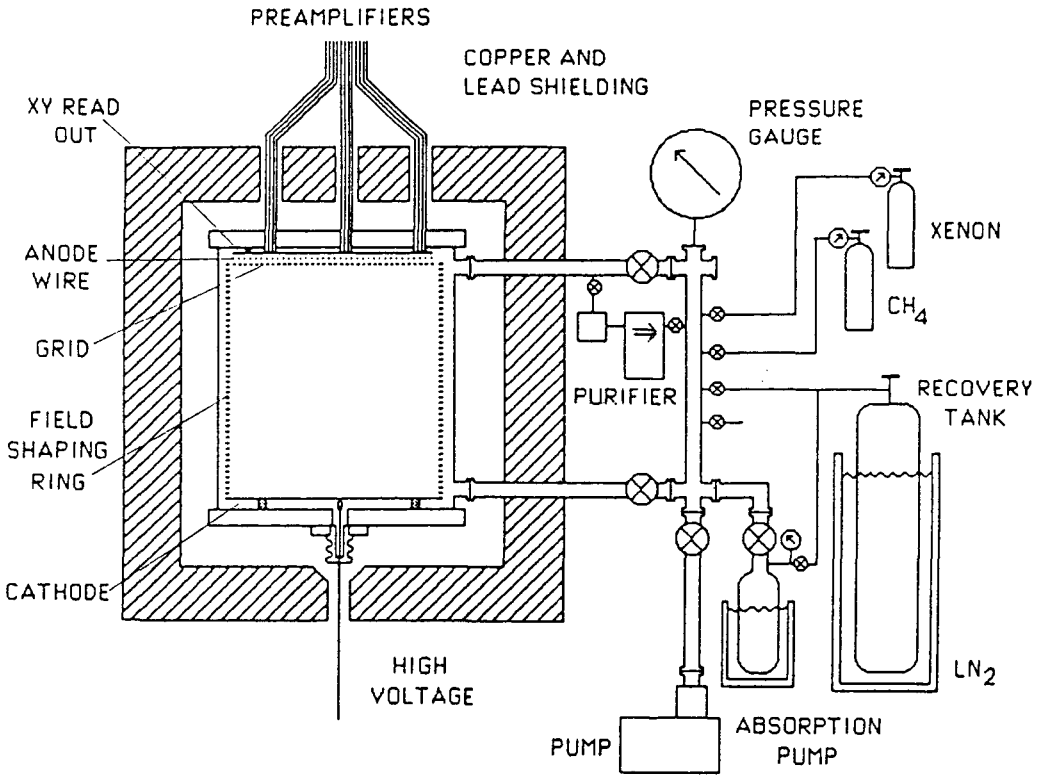

Figure 3.5 The schematic diagram of the experimental set up, including the main chamber, shieldings and the gas handling and purification system.

a)

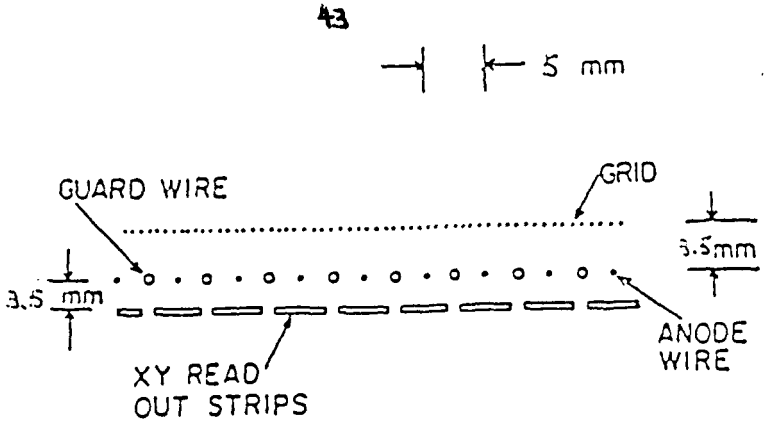

b)

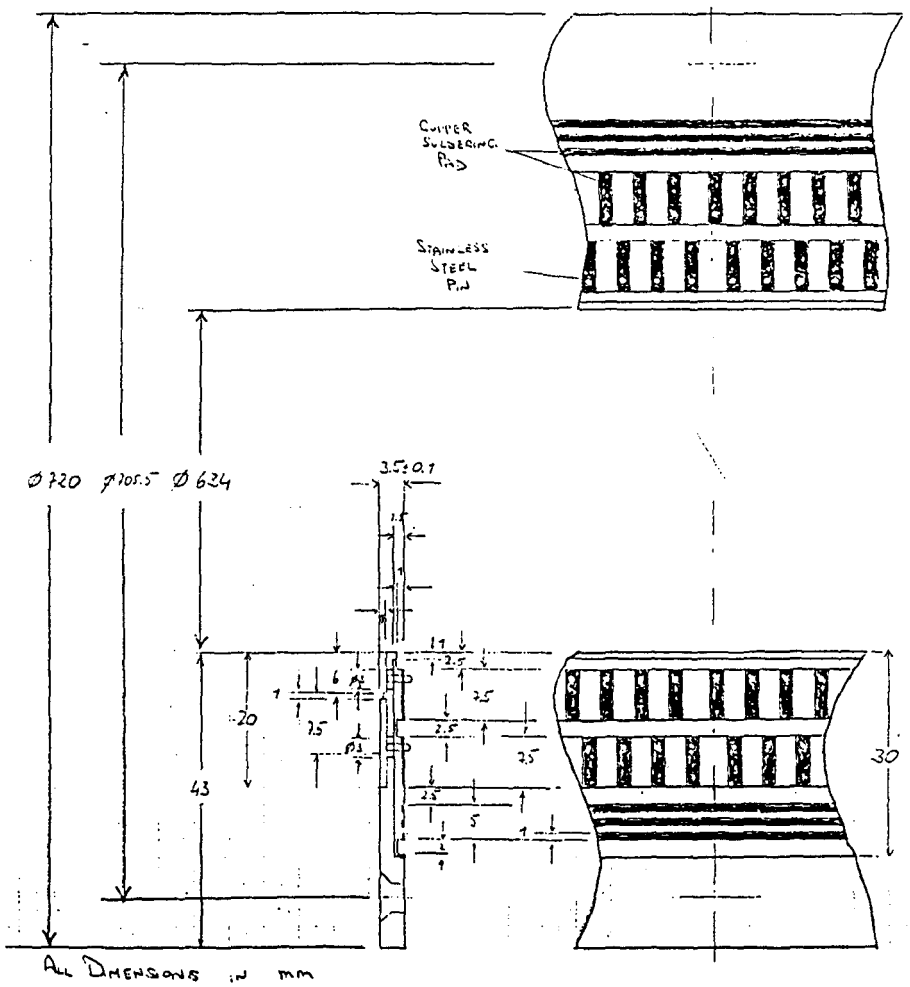

Figure 3.6 The anode system: (a) the geometry, and (b) the wire mounting scheme.

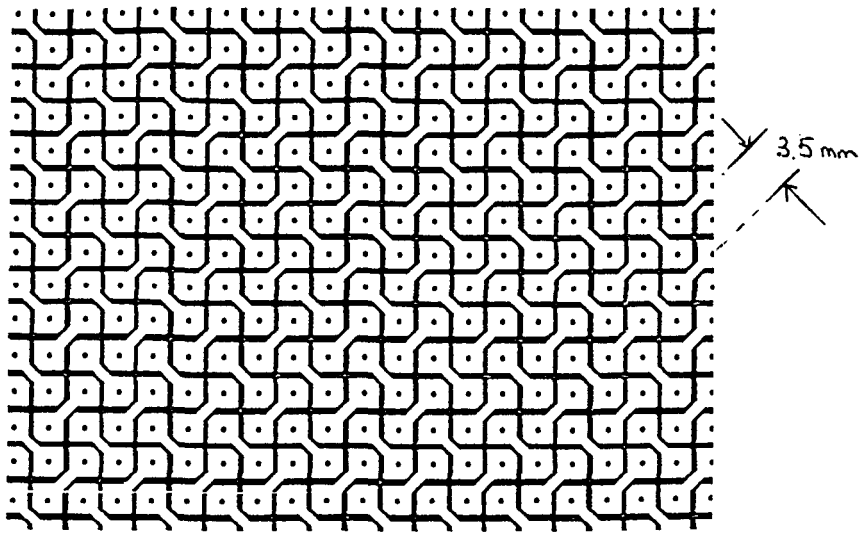

Figure 3.7 The design of the XY readout pads. The same pattern is etched on both sides of a Rexolite board, and is shifted by half a unit in both X and Y. The holes are plated through with copper to provide electrical continuity in one channel.

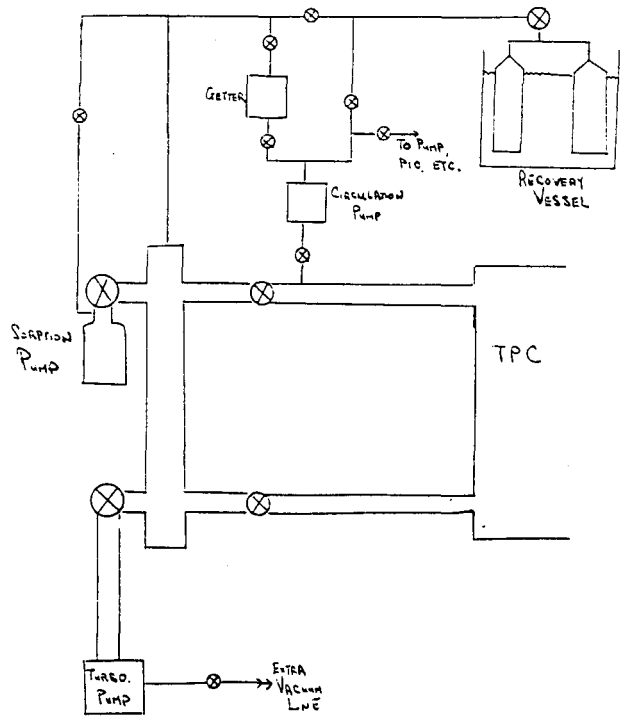

Figure 3.8 Detailed layout of the gas handling and purification manifolds.

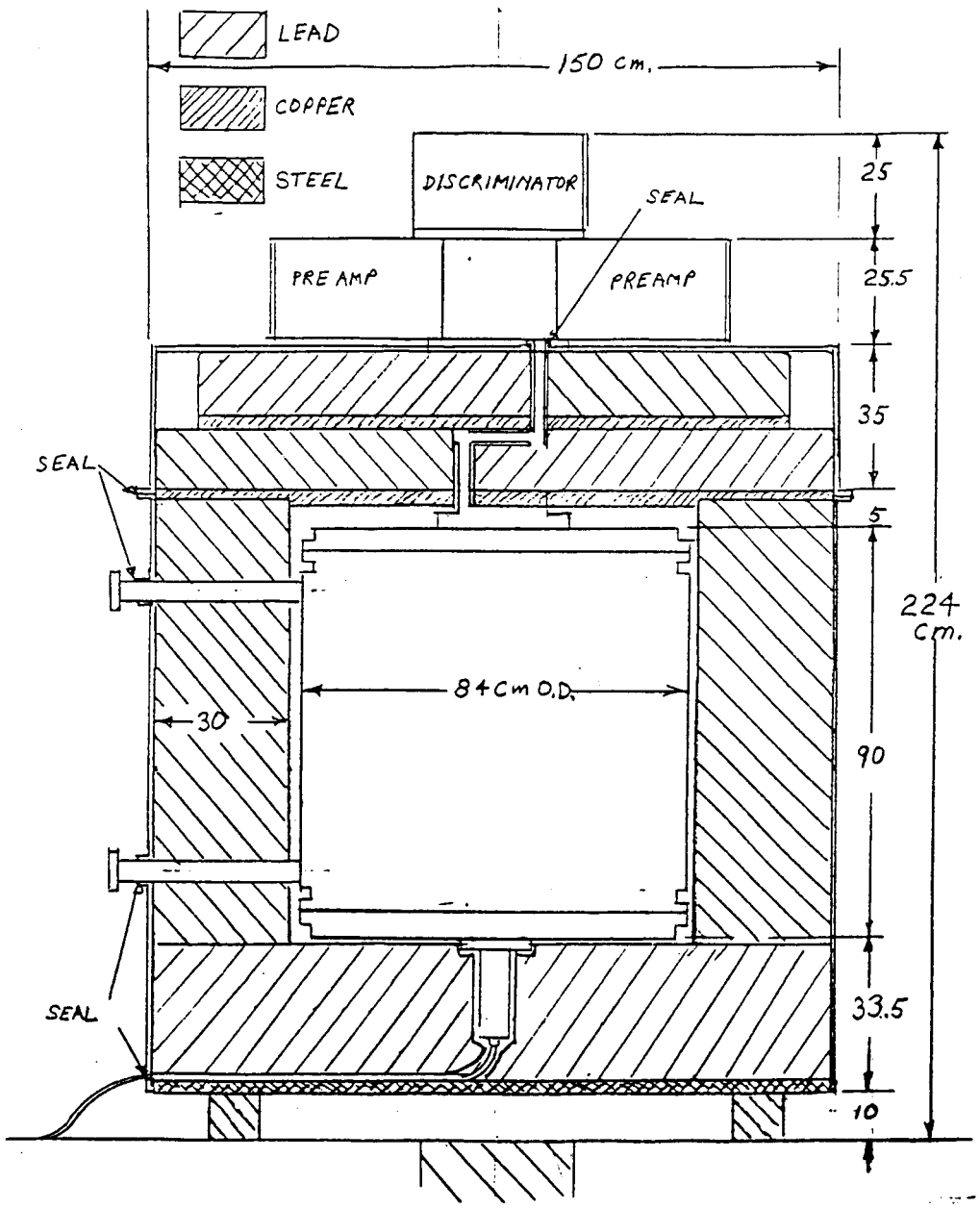

Figure 3.9 The design of the TPC shieldings.

CHAPTER 4

SIGNALS AND DATA PROCESSING

In this chapter, we discuss the electronics[40] and data acquisition system[41] of the TPC. The schematic diagram is shown in Fig. 4.1. The TPC does not have a time zero trigger, so that the starting time of an event is defined by the beginning of the signals from the anode wires. Data within the next 64 μs are recorded. The inverted (positive) output of the anode preamplifier is digitized continuously by a transient recorder at a rate of 8 MHz. During that time, signals from the XY channels are processed by the preamplifiers and discriminators. The digitized outputs are stored temporarily in the CAMAC interface modules. If a LAM (Look At Me) signal is generated, the event is considered good and the system will wait for 4 ms to record delayed events before the memory is read off by the front-end processor (PDP 11/73). The PDP 11/73 then compresses the data and sends them to a UNIX host (Tektronix 6130) via Ethernet. The data transfer consumes about 15% of the CPU time of the Tek 6130, while the rest of the time can be used for on-line data analysis to select events to be saved on cartridge tapes (61TC01), if this is necessary.

The system can handle about 5 events per second. The design allows the discriminators to be replaced conveniently by flash ADCs. Individual components of the system are discussed in detail in subsequent sections. The working parameters are listed in Table 4.1.

4.1 Electronics

4.1.1 Preamplifiers

In 5 atm of xenon gas, a minimum ionizing electron deposits about 30 keV of energy in one cm, corresponding to the production of about 1000 ion-electron pairs. At a drift speed of about 1 cm μs^{-1}, a vertical trajectory will produce a current of about 0.2 nA. A modest charge multiplication of 1000 in the anode boosts the current up to μA level. Therefore, in order to have an output signal of reasonable size, a current sensitive preamplifier with a gain of the order of 100 mV μA^{-1} is needed.

The preamplifier makes use of the IC LeCroy TRA1000 and the circuit is shown in Fig. 4.2. The inputs are connected to the XY channels and veto ring through edge connectors. The veto ring is divided into four sectors, each having its own preamplifier. The circuit is capable of producing 800 mV pulses with a noise level of about 5-10 mV, although the typical output voltage is about 200 mV. The gain is 270 mV μA^{-1}. Twelve preamplifiers are packed onto a single board mounted in a modified NIM crate with $\pm$12 V power supplies. Complete electronics include 28 such boards, each of which is replaceable if necessary. Since electronic components contain radioactive materials, the NIM crates are assembled 30 cm on top of the TPC, outside the lead shielding.

The same circuit is used for the anode signals, except that there is an additional high voltage blocking capacitor (6 kV, 100 pf). The high voltage is applied through a 22 MΩ resistor to limit the current drawn from the power supply and to block the anode signals from reaching it. This preamplifier is placed in a shielded box and is powered separately.

4.1.2 Discriminators

In this experiment, we are interested in a spatial resolution of a few mm, corresponding to a drift time of a few hundred ns. Therefore, 100 ns discriminators are adequate.

The discriminator uses a low cost voltage comparator IC (LM319) and the circuit is shown in Fig. 4.3. Each input signal is fed into two comparators each with its own threshold level. Reasons for adopting this two-level digitization scheme have been discussed in Section 2.2. Eight channels are grouped together and share the two common thresholds, adjustable by trim pots on the front panel. Three such groups, that is, 24 channels, are packed together onto a circuit board mounted in a single-width NIM module. The output is TTL (Transistor-Transistor Logic) compatible, with TTL low as the signal configuration (that is, the normal state is 5 V while the signal state is 0 V). The output is driven by a line driver (IC 74LS240) and can be transmitted through 3 m of ribbon cable.

The amplified signals of the anode and veto ring also pass through identical discriminators but each is in its own shielded box. The output from the lower threshold level of the anode discriminator provides the *Start Trigger* for the CAMAC Controller Circuit, whereas that of the higher one gives the *Blob Trigger*. Output from the four veto ring discriminators goes to the *VETO* line through a one-fold coincidence.

4.1.3 Transient Recorder

The inverted (positive) signals from the anode preamplifier go to a commercial transient recorder, LeCroy TR8837F, which has 8-bit digitization. It

is a single-width CAMAC module and operates with standard CAMAC commands. It is equipped with programmable sampling speed (32 MHz maximum), memory size (8 k maximum) and pretrigger size. The *Stop* line receives pulses defining the end-point of any valid event from the CAMAC Controller circuit. These pulses synchronize all the modules in the CAMAC bus.

4.1.4 CAMAC Interface Circuit

The TTL output of the discriminators is stored in the memory banks housed in single-width CAMAC modules. Each module has 48 input lines to match the output from a single discriminator box, thus handling 24 channels. There are 14 such modules in a single CAMAC crate for the complete electronics. They can operate with a maximum clock speed of 8 MHz, and have a memory size of 2048. The design of the circuit is flexible enough to incorporate full digitization with a flash ADC system replacing the discriminators, if necessary. The CAMAC Controller circuit provides all the modules with trigger, veto and clock signals through the unused lines of the CAMAC bus (the P1, P3, P4 and P5 lines).

The schematic diagram of the CAMAC Interface circuit is shown in Fig. 4.4. The circuit can be in either *Write* or *Read* state, selected by CAMAC command F24 (or Crate-C) and F25 (or Crate-Z) respectively. In the *Write* state, the modules start storing data when they receive a *Start Trigger* originating from the anode wires. An event is rejected if *Veto* signals are received within one drift time before or during the event. A LAM state is generated if a *LAM Trigger* is received during the event, in the absence of any *Veto*. This instructs the PDP 11/73 to read the memory, after a post-trigger delay of 4

ms. An event only occupies a fraction of the memory bank. The remaining portion of the memory is used for storing delayed activities that might occur within some specified time after the first event. Such delayed events are useful for identifying some possible decay chains contributing to the background. After that, the circuit is reset to the *Read* state.

The TTL input signals from the low and high threshold levels of the discriminators are stored in two different memory blocks (the *tracks* and the *blobs*) in each module. In the *Read* state, the two memory blocks are separately tested to check if they contain any data for the event, using the CAMAC commands F8*A1 for the *tracks* and F8*A2 for the *blobs*. If the test is positive, that particular block is read by the CAMAC Direct Memory Access (DMA) commands, F1*A1 for the *tracks* and F1*A2 for the *blobs*. This testing procedure saves reading time by skipping over those memory blocks without any data.

4.1.5 CAMAC Controller Circuit

The CAMAC Controller circuit provides four control signals, *Clock, Start Trigger, LAM Trigger* and *Veto*, to the CAMAC modules through the P-lines of the CAMAC bus, using the IC 74S04 as current driver. The schematic diagram of the circuit is shown in Fig. 4.5.

The *Clock* frequency is selected by a switch on the front panel. The *Start Trigger* is the TTL output of the lower threshold level of the anode discriminator, and defines the starting point of an event. The *Veto* signal is generated by a one-fold coincidence of the four input veto lines connected to the veto ring discriminators. The *LAM Trigger* is generated by any combination of the following trigger options:

1. *Blob Trigger*, produced by the anode discriminator with higher threshold level. This can reject all minimum ionizing events, such as muons.

2. *Energy Trigger*, generated when the integrated anode signal is higher than a certain threshold. This is to reject all events of less than 500 keV.

3. *Length Trigger*, produced when the *Start Trigger* is continuous and longer than a time selected by a switch on the front panel. This is to reject all short events due to noise and low energy (< 100 keV) electron tracks.

An additional requirement is that none of the veto lines fires, signifying that the event is totally contained in the active volume of the TPC. The *Muon Trigger* can start and trigger an event, and disable the *Veto*. This trigger is produced by the coincidence signals from the plastic scintillators on the top and bottom of the chamber, and can capture vertical muon events. Such events are useful for the purpose of calibration and monitor.

The *LAM Trigger* will generate a *Stop* pulse at the end of an event, which in turn, generate a LAM. Then the CAMAC interface will wait for a fixed period of time, selected by software (typically 4 ms), to look for delayed events. The number of *Stop* pulses is the total number of events within this time. This number, together with the time delay between the first and second events, is then read off by the CAMAC command F1. However, since the transient recorder cycles continuously, no energy information can be extracted for the delayed events.

4.2 Data Acquisition

4.2.1 Front End Processor

A PDP 11/73 works as a front end processor to read the CAMAC modules, compress the data and send them to the host computer, Tektronix 6130, via Ethernet.

Several control parameters like memory size, transient recorder clock speed, and post-trigger wait time, are also sent into the CAMAC modules through the 11/73. After an event finishes, the 11/73 sets the modules to *Read* state. It then accesses the transient recorder for the energy signals, the CAMAC boards for the *tracks* and *blobs* data, as well as other miscellaneous information, using a standard CAMAC DMA Interface. A typical event consists of about 50 kbytes of data. The system is designed to handle 5 events per second, in which case the raw data rate would be about 250 kbytes per second.

Most of the data from the *tracks* and *blobs* memory blocks are zeros corresponding to inactive channels, and so data compression to reduce the data size is necessary before any further processing. The data compression routines remove all the zeros and reformat each point in *tracks* and *blobs* into two bytes of information: 5 bits (0 - 31) for X or Y channel number in a particular module (24 channels per module), 11 bits (0 - 2 k) for the Z-coordinate. The state X/Y equals 31 and Z equals 0 is an increment flag for the module number. The data are then packed in the following characteristic order: (X,Z) for *tracks*, (Y,Z) for *tracks*, (X,Z) for *blobs* and (Y,Z) for *blobs*. Within each of these sectors, for instance (X,Y) for *tracks*, the data is in ascending order in X, and for each X, ascending order in Z. This scheme is very efficient and can reduce the data size of a typical event to about 3 kbytes.

The data will then be transmitted to the host computer via Ethernet, using the DEQNA board that resides on the 11/73 Q-bus. The User Datagram Pro-

tocol (UDP) level of the TCP (Transmission Control Protocol)/IP (Internet Protocol) is chosen for the networking because it provides a low level interface with a minimum of overhead but is accessible by standard system calls on any host computer running Berkeley UNIX. The UDP data packet structure is shown in Fig. 4.6. Each packet consists of several layers of data, each of which contains information about the structure of the next one. The data of a typical event is transmitted over the Ethernet in a variable number of packets. The user data of the first packet consists of the energy signals and the miscellaneous information. The length of the first packet (1450+2*N bytes) is used to indicate the total number of packets (N) in the event. The second and subsequent packets contain the trajectory information and each has a fixed length of 1472 bytes. A typical event may fill up two to three packets. The networking is completely modular. If more computing power is needed for analysis, the 11-73 can send alternate events to two or more host machines. Similarly, the front end processing can be sub-divided if necessary.

4.2.2 Host Computer

The host computer is a Tektronix 6130 workstation running UTEK, a version of Berkeley 4.2 UNIX. The 6130 receives data packets from the 11/73, and stores them in buffers with sequentially increasing port numbers. The 6130 has 45 ports altogether, whereas a typical event uses up only two to three packets. The remaining ports thus serve to buffer the input to the host. The 6130 reads and then clears the ports in sequence, and when the port number reaches 23, it sends a handshake signal to the 11/73. Upon receiving the handshake, the 11/73 will send the next data packet to the first port, and the cycle continues. To keep both computers in synchronization all the time, the 11/73 will send

out a blank event to the 6130 whenever there is no data transfer for more than 45 s.

After reading the ports, the 6130 unpacks the data and reconstructs the event. The on-line diagnostic facilities available include trajectory reconstruction and plotting in (X,Z) and (Y,Z) projections, display of the digitized energy signals, statistical histograming of hits for individual channels, plotting of energy spectra and output to a laser printer. The events that survive various on-line data analysis programs will be stored on 61TC01 60 Mbyte cartridge tapes. Each tape can typically archive some 20 k events.

The limiting factor of the data rate is the data compression routine in the 11/73. The maximum data rate achieved (when there is no trajectory to be compressed) is 80 kbytes per second. A designed count rate of five events per second corresponds to a data rate of about 15 kbytes per second. This leaves sufficient CPU time (about 85%) for the on-line analysis programs to execute in the host computer.

4.3 Data Analysis

4.3.1 On-line Data Analysis

The *LAM Trigger* in the CAMAC Interface modules provides the first level of on-line data analysis. The trigger options have been described in Section 4.1.5. The *LAM Trigger*, which defines a valid event to be read, can be any combination of the those options. However, not knowing the exact acceptance and rejection efficiencies of each option, and for future diagnostic purposes, we use only the *Energy Trigger* when data are taken at Gotthard, and read

every event with energy above a certain threshold. The threshold chosen is 300 keV, corresponding to an event rate of about 1 per 10 seconds. All events with *Muon Trigger* are also saved and specially tagged. These vertical muons events are useful for monitoring the drift velocity, and therefore the composition, of the gas.

Moreover, one can have second and third level triggers if necessary, before finally writing data to tape. The PDP 11/73 does simple tests like rejecting events that saturate the electronics or those without tracks. The Tek 6130 has enough CPU time (about 85%) to execute more sophisticated programs. An example of one of such programs, *"boxcheck,"* is outlined in Appendix 4. During the runs at Caltech to measure the energy spectrum of the ^{207}Bi internal conversion source, a program *"esource"* is executed on-line by the Tek 6130. The program selects electrons originating from a certain range of (X,Y) at the cathode. It works very well, and almost all events selected are real ones from the source. For the initial runs at Gotthard, the Tek does not do any on-line data analysis, and writes everything it receives from the PDP onto cartridge tapes.

4.3.2 Off-Line Data Analysis

Work done so far on this problem is only preliminary, and it will be one of the primary focuses when the experiment is running in its final configuration at Gotthard. The cartridge tapes are read by a Tek 4301 at Neuchâtel, and the data can be transferred to the VAXes at Neuchâtel and PSI, via Ethernet.

The track analysis programs already developed emphasize handling the data from the two projections [(X,Z) and (Y,Z)] separately. For instance, the

program *"connect"* checks the continuity of the tracks in a projection, and identifies multiple tracks in an event, with an efficiency of 100% for Monte Carlo trajectories. As noted above, another program, *"boxcheck,"* is outlined and discussed in Appendix 4.

The important quantities of interest for background rejection are the charge depositions at the ends of a track, and to a lesser extent, their curvatures (second derivatives). Therefore, the major problem of data analysis is to fold two 2D projections into one 3D (X,Y,Z) ordered array from one end to the other. However, an algorithm to perform this task is far from simple. From experience with the preliminary programs, there are some subtleties and difficulties. Recorded tracks may be broken where they are continuous, and noise may arise where they should not be. Sharp bends, smearing out of the trajectories in charge multiplication, and energetic delta electrons leaving the main tracks, may also cause confusion. The tracks have no preferred origin, direction and orientation, thus demanding a very general algorithm. Another problem is combinatorial ambiguities. Given a Z-plane at which the track crosses more than once (say two), then it is impossible to decide which two of the four combinations of (X,Y) correspond to the real location of the track. One has to start from a Z-plane where the (X,Y) of the track is uniquely defined and evolve from that point, imposing the continuity condition as the track goes along.

For high energy (> 2 MeV) events, the expected rate is about 10^3 to 10^4 per year. This rate makes it feasible to look into the 0ν region manually or semi-manually. The user can interact with the computer to form the ordered (X,Y,Z) array for each event. Based on this, further programs can be executed to evaluate the charge depositions and second derivatives. A program has been

developed along this line to compare the charge depositions in both ends of an internal conversion electron trajectory. The results are described in more detail in Section 6.2.8. Track reconstruction in the 2ν region ($\sim$1 MeV) will be even more difficult, since the event rate is higher and the trajectories are shorter.

1.	Preamplifiers	
	Gain	270 mVμA^{-1}
2.	Discriminators	
	Lower threshold for anode	5 mV
	Upper threshold for anode	20 mV
	Lower threshold for XY channels	5 mV
	Upper threshold for XY channels	45 mV
	Threshold for the four veto ring channels	15 mV
	Threshold for the integrated anode signals	10 mV
3.	Transient Recorder	
	Memory size	128
	Clock frequency	8 MHz
	Pretrigger fraction	5/8
4.	CAMAC Interface	
	Memory size	128
	Clock frequency	2 MHz
	Continuity cut for anode signals	0 μs
	Post-trigger wait time	4 ms
5.	Networking between Computers	
	No. of ports used in host	23
	Maximum waiting time at each port	100 s
	Maximum waiting time for LAM	45 s

Table 4.1 Working parameters for the electronics and data acquisition system of the TPC.

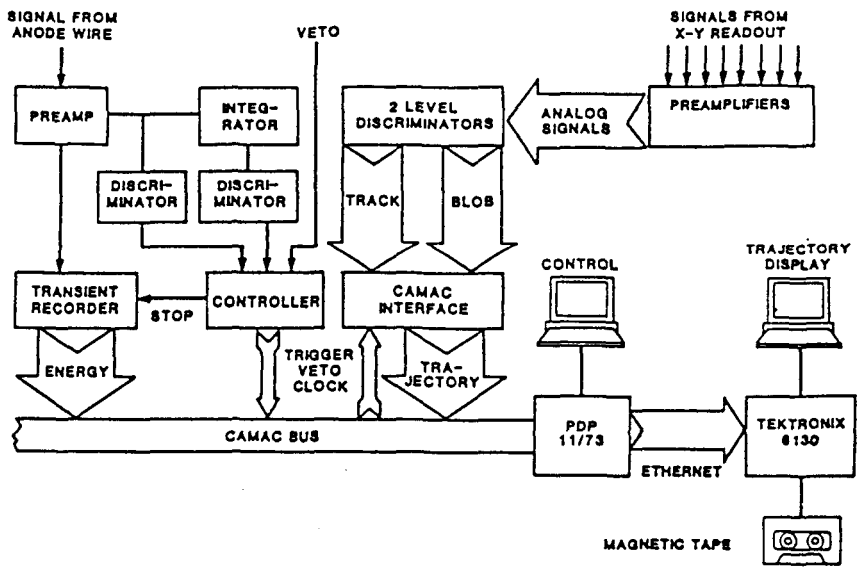

Figure 4.1 The schematic diagram of the electronics and data acquisition system.

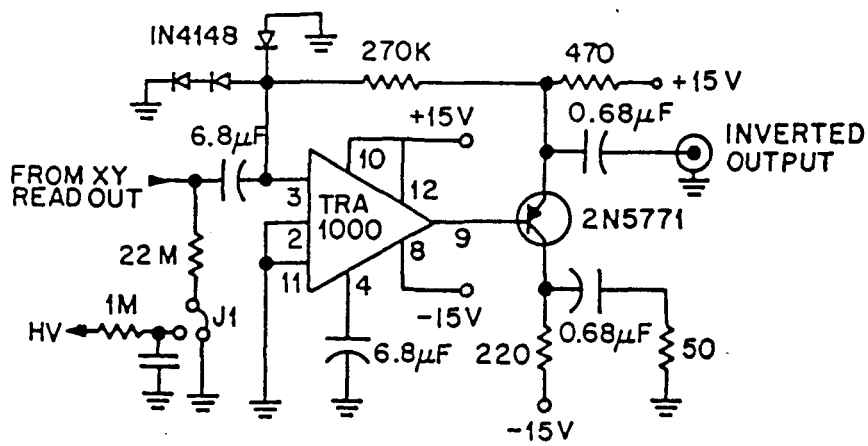

Figure 4.2 Circuit diagram of the preamplifier. For the anode signals, the input capacitor is replaced by a high voltage blocking capacitor, and the jumper J1 is connected to the high voltage instead of ground.

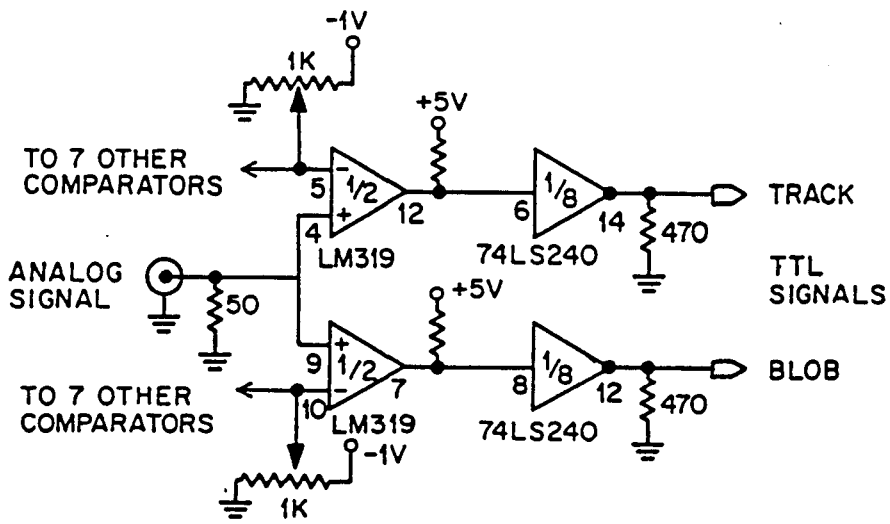

Figure 4.3 The circuit diagram of one discriminator unit. The discriminator with a lower threshold level gives information on "TRACK," while the one with a higher level gives information on "BLOB."

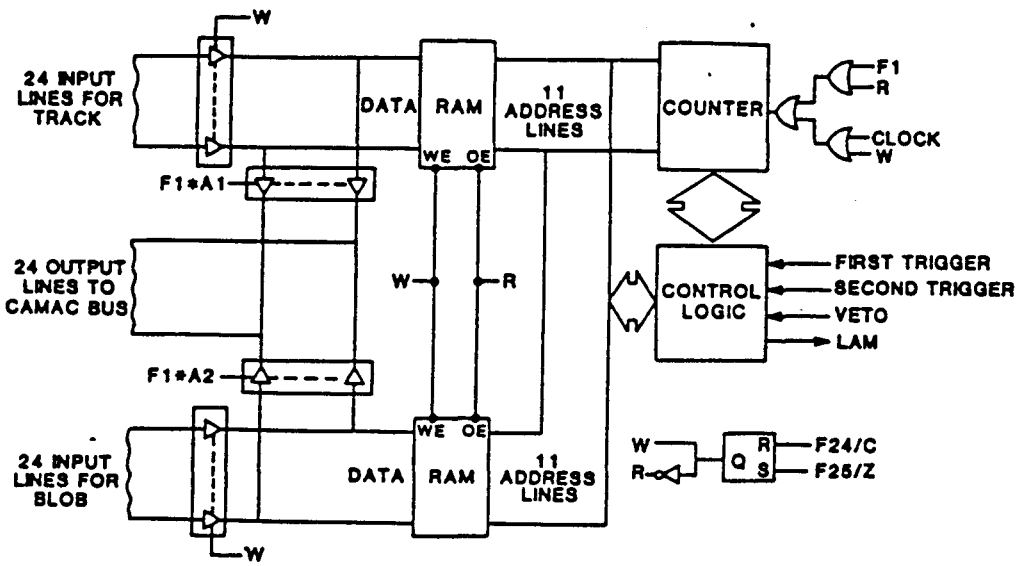

Figure 4.4 The schematic diagram of the CAMAC interface modules.

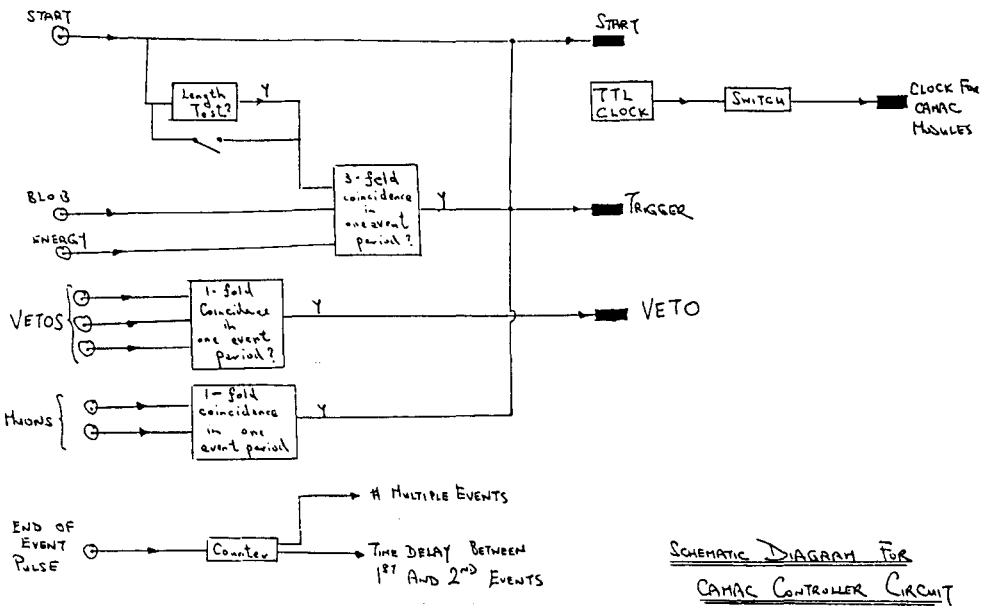

Figure 4.5 The schematic diagram of the CAMAC Controller module.

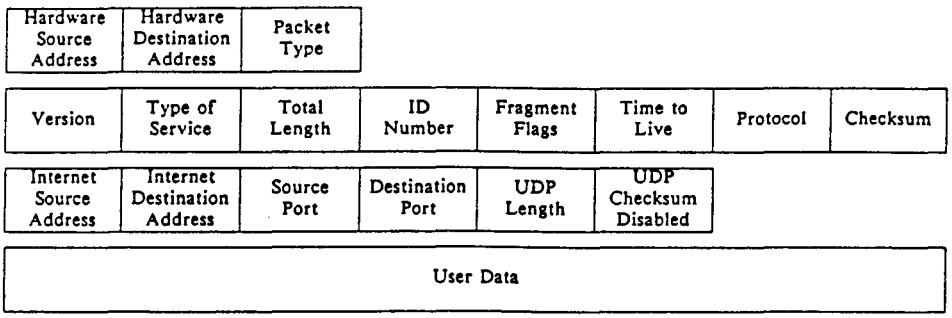

Figure 4.6 The UDP data packet structure. A UDP packet is split into 4 layers. The first is the Ethernet header (14 bytes), the second the Internet header (12 bytes), the third the UDP header (14 bytes), and the last one is the user data (1472 bytes).

CHAPTER 5

BACKGROUND AND EXPECTED LIMIT

5.1 Sources of Background

In low count rate experiments such as double beta decay searches, proper understanding of the background is crucial[42]. The various expected sources of background are discussed below. Measurements and interpretation of the background are presented in Chapter 7.

5.1.1 Cosmic Rays

At ground level, the rate of cosmic rays hitting the TPC is about 100 s^{-1}. The muons usually produce straight minimum ionizing trajectories whereas the nucleon components are heavily ionizing, and have a higher probability of giving rise to showers. During the test runs at Caltech, a scintillator panel is placed on top of the chamber. This, together with the veto ring, can reject about 90% of the events. The remaining events lead to considerable system dead time. Another problem is muon capture by the copper vessel or lead shielding, producing high energy gamma rays and neutrons.

To minimize this muon-induced background, the experiment is conducted in the underground laboratory in the St. Gotthard road tunnel in Switzerland. The overburden is approximately 1000 m of rock from Monte Prosa (3000 m water equivalent), and attenuates the muon flux by a factor of 2×10^5 to 4.4 $hr^{-1}m^{-2}$, as shown in Fig. 5.1. At this flux, and folding in a solid angle efficiency factor, the event rate for vertical muons in the TPC is expected to

be a few per day. These events are stored for diagnostic purposes and are useful for measuring the drift velocity of the fill gas, and hence monitoring the Xe-CH_4 ratio.

Before the TPC is moved underground, cosmic ray fast neutrons interact with the copper vessel, creating radioactive isotopes whose decays will contribute to the background. The list of these isotopes, their decay energies and lifetimes is given in Table 5.1. The reaction ^{63}Cu(n, α + 4n)^{56}Co is a particular problem since the ^{56}Co emits gamma rays of energy up to 3.27 MeV. However, ^{56}Co is relatively short-lived (half-life 78.8 days) and the intensities of these background lines will drop once the experiment is moved underground. As for the long-lived ^{60}Co (half-life 1934 days) from ^{63}Cu(n, α)^{60}Co, it is estimated[43] that over one year of sea-level cosmic-induced interaction, the ^{60}Co activity is 2-3 decays per kilogram of copper per day. Therefore, folding in solid angles and cross-sections, it will not give rise to substantial background.

Similarly, cosmic ray muons can also induce production of unstable or excited nuclei by electromagnetic nuclear reactions[44]

$$\mu + A \rightarrow \mu' + A^* \text{ or } \mu' + X\,.$$

The final isotopes are, however, short-lived or of low energy. Therefore, muon-induced radioactivity is negligible in the Tunnel where there are only a few muons per hour hitting the TPC.

5.1.2 Natural Radioactivity from Surrounding

There is always trace radioactivity in the tunnel walls and the equipment surrounding the TPC. Electrons and alpha particles are short-ranged

and therefore do not give rise to problems. However, gamma rays can penetrate through the shielding and contribute to the background. Whereas the radioactive level of the equipment used is difficult to estimate, the tunnel background is well known from measurements by the Caltech-SIN-Neuchâtel Ge experiment[45]. The rock in the tunnel is primarily red granite, which contains about 10 ppm by weight of ^{232}Th and ^{238}U. Both isotopes are precursors of natural decay chains shown in Tables 5.2a and 5.2b. The radioactivity levels of various gamma lines in both chains measured by an unshielded germanium detector are given in Tables 5.3a and 5.3b. The gamma rays have energies up to 3.27 MeV. All the lines above 2.7 MeV originate from the decay of ^{214}Bi along the ^{238}U series, and are much weaker, as listed in Table 5.3c. The background continuum spectrum is shown in Fig. 5.2. It represents the flux of gamma rays being Compton scattered from the rock before hitting the detector. The measurements show that the gamma flux falls sharply beyond 2.7 MeV.

Besides the contributions from the two decay chains, we also expect to see the gamma lines of ^{125}Sn (427.9 keV) and ^{40}K (1460.8 keV) from equipment, as well as the long-lived ^{137}Cs (661.6 keV) line resulting from the explosion of the Chernobyl nuclear power plant.

The gamma flux at the TPC can be reduced by a factor of 10^{-7} at 2.5 MeV with 30 cm of lead shielding and 5 cm of copper from the chamber wall. The detail of gamma ray induced background is discussed in the next section.

Moreover, both the ^{238}U and ^{232}Th chains may emit radioactive radon gas, ^{222}Rn (half-life 3.8 days) and ^{220}Rn (half-life 55 s). To prevent radon from diffusing to the inside of the shielding, the entire lead house is enclosed in a tight aluminium box slightly pressurized by dry nitrogen.

Another source of external background that requires special attention is

the thermalized neutrons produced by fission and the (α,n) reaction. Thermal neutrons captured by the nuclei are accompanied by the emission of high energy gamma rays. In particular, the reaction $^{136}Xe(n,\gamma)^{137}Xe$ ($\sigma = 0.16$ b) gives rise to the beta decay in the active volume:

$$^{137}Xe \rightarrow {}^{137}Cs + e^- + \bar{\nu}_e \, (Q = 4.1\,\mathrm{MeV}(33\%)/3.6\,\mathrm{MeV}(67\%); T_{\frac{1}{2}} = 3.9\,\mathrm{min}).$$

The thermal neutron flux is attenuated by the lead shielding and copper vessel by a factor of 6×10^{-3}. We expect that this will not be the dominant contribution to the background. If necessary, boron loaded polyethylene can be added to further reduce the flux.

5.1.3 ^{85}Kr

Commercial xenon contains about 15 ppm of krypton, about one part in 10^{12} of which is the radioactive ^{85}Kr, produced in nuclear reactors or bomb tests. The isotope is a beta emitter with end-point energy of 687 keV and half-life of 10.7 yr. This will give a low energy background at the rate of about one per second. This background can be rejected on-line with a hardware energy cut. The amount of ^{85}Kr is expected to be considerably less with enriched ^{136}Xe, as measured by the Milano MPC[28]. This concentration can be further reduced by fractional distillation if necessary.

5.1.4 Natural Radioactivity from Internal Components

To minimize internal background, the TPC is built with low background materials: OFHC copper for all metallic components, and Delrin for all insulators. Materials used inside the chamber other than copper and Delrin

constitute only a very small proportion by mass, and have been tested for trace radioactivity, with the low-background germanium facility at Neuchâtel. Details and results of the test are discussed in Section 6.4.

Emission of radioactive radon gas from the contaminants also requires careful study. Some of the daughters of ^{220}Rn and ^{222}Rn are beta emitters. Therefore, they can contribute to background events if they decay inside the active volume of the TPC, or at the surface of the cathode. The lists of these decays are given in Table 5.2a and 5.2b, for the ^{238}U and ^{232}Th series, respectively.

All the daughter nuclei of ^{220}Rn (^{232}Th series) are short-lived, and therefore will not cause permanent damage to the gas. However, for ^{222}Rn of the ^{238}U series, there is one long-lived daughter, ^{210}Pb (half-life 22.26 yr), whose decay is followed by another beta decay with 1.16 MeV end-point. Therefore, contamination by ^{222}Rn may give rise to additional low energy background.

Quantitative studies of the background contributions from the internal components are not available. This is a crucial piece of information that needs to be extracted from the TPC data.

5.2 Background Events

The powerful track reconstruction abilities of the TPC make it possible to reject most events originating from various background sources. A $\beta\beta$ event will be identified as a continuous trajectory with high charge depositions and large angle scatterings (that is, high second derivatives) at both ends. Under this criterion, most ($> 95\%$) of the single electron tracks can be rejected. Rejection of muons and alpha particles can be achieved with 100% efficiency

just by track reconstruction alone. The possible background events that may mimic real $\beta\beta$ ones are discussed below.

5.2.1 Single Electron Trajectories

Primary electrons may emit energetic (> 50 keV) secondary electrons (δ-electrons) at the beginning portion of its trajectory, thus giving rise to charge *blobs*. Our Monte Carlo simulations suggest that 95% rejection efficiency for single electron tracks of 2.5 MeV at 5 atm of xenon is possible, by summing up and comparing the charge depositions at both ends of the tracks, as shown in Figs. 3.3a and 3.3b. An even higher rejection efficiency can be achieved by considering the second derivatives of the tracks at both ends. Single electron tracks have relatively straight beginnings, whereas both ends of $\beta\beta$ events undergo large angle multiple scatterings and become more staggered.

The mechanisms for producing single electron trajectories include:

1. *Compton Scattering:* This process occurs when a gamma ray scatters off an atom and loses part of its energy to the bound electron. The maximum energy transferred to the electron occurs at a scattering angle of 180° and defines the Compton edge given by

$$E_{edge} = E_\gamma \left[1 - \frac{1}{1 + \frac{2E_\gamma}{m_e}} \right] .$$

Substituting $E_{edge} \sim 2.5$ MeV, one gets $E_\gamma \sim 2.73$ MeV, implying that only gamma rays with energies above 2.7 MeV can produce Compton electrons with energies of 2.5 MeV or above. This is fortunate since the background continuum spectrum of Fig. 5.3. shows that the gamma flux falls rapidly beyond 2.7 MeV.

2. *Photoelectric Effect:* This is the process where the incident photon is completely absorbed by the atom with the ejection of a photoelectron of energy

$$E_e = E_\gamma - E_{binding}$$

where $E_{binding}$ is the binding energy of the electron. For gamma rays above 20 keV, inner shell electrons are most likely ejected so that $E_{binding} \sim$ 35 keV for xenon. Outer shell electrons then undergo a transition, producing a 30 keV X-ray and several soft photons. The X-ray has a mean free path of about 5 cm in 5 atm of xenon, so that it may appear as an isolated charge deposition separated from the main track. The photoelectric cross section varies as E_γ^{-3} and is about a factor of 30 less than that of Compton scattering for $E_\gamma \sim 2.5$ MeV in xenon.

3. *Beta Decays from Internal Radioactivity:* Beta decays of ^{85}Kr will dominate the background at low energies (< 600 keV). Daughter nuclei along the decay chains of ^{220}Rn and ^{222}Rn, emitted from various internal components, may contribute if they undergo beta decays inside the active volume of the TPC, or at the surface of the cathode. Among all the decays, only one has end-point energy higher than 2.48 MeV:

$$^{214}\mathrm{Bi} \rightarrow {}^{214}\mathrm{Po} + e^- + \bar{\nu}_e \, (Q = 3.28\,\mathrm{MeV},\, T_{\frac{1}{2}} = 19.7\,\mathrm{min}),$$

followed by

$$^{214}\mathrm{Po} \rightarrow {}^{210}\mathrm{Pb} + \alpha \, (Q = 7.8\,\mathrm{MeV},\, T_{\frac{1}{2}} = 164\,\mu\mathrm{s}).$$

This reaction can be singled out by looking at any $\sim$100 μs delayed post-trigger activity after the first event. The readout system of the TPC is sensitive to decay chains separated by more than $\sim$5 μs.

5.2.2 Pair Production

Gamma rays above 1 MeV can interact with the nuclear Coulomb field to produce electron-positron pairs. The positron will then stop and annihilate with an atomic electron producing two 511 keV gamma rays.

Since the TPC cannot distinguish positrons from electrons, a pair production event will look similar to a $\beta\beta$ one. However, pair production vertices are more sharply peaked ($< 70°$ if both leptons have comparable energies), so that one can reject events with a sharp vertex near the central portion of the trajectory. Moreover, a 511 keV photon at 5 atm of xenon has a mean free path of about 380 cm, thus having 8% chance of an additional interaction inside the TPC. Therefore, at least 16% of the pair production event can be rejected by looking for multiple tracks within the same event.

To produce a 2.5 MeV pair production event, a gamma ray of 3.5 MeV is needed. However, from the background continuum spectra of Fig. 5.3, the gamma flux at 3.5 MeV is about 10^{-4} times less than that at 2.5 MeV. Contribution to background events by pair production is therefore suppressed.

5.2.3 Double Compton Scattering

This is a higher order process in which the photon resulting from a Compton scattering can scatter again within 1 cm ($\sim 3\times$TPC spatial resolution) of the vertex, so that the two tracks cannot be separated. Compton scattering followed by photoelectric effect can also be included in this category.

5.2.4 ^{208}Tl gamma rays

The 2614 keV ^{208}Tl gamma line is the only intense gamma source near or above the transition energy (T_0=2480 keV) of $O\nu\beta\beta$ for ^{136}Xe, and therefore requires special attention. (There are some weak lines up to 3.27 MeV, following the decays of ^{214}Bi, as listed in Table 5.3c.) The Compton edge is at 2381 keV which is within the energy window

$$(T_0 - FWHM = 2356\,\mathrm{keV}) < (E_{edge} = 2381\,\mathrm{keV}) < (T_0 - \frac{1}{2}FWHM = 2418\,\mathrm{keV}),$$

where $FWHM$ equals 124 keV, from the 5% energy resolution at T_0. Besides, the photo-electrons of the K-shell have energy

$$E_e = E_\gamma - E_K = 2579\,\mathrm{keV}.$$

Together with the absorption of soft photons and a 30 keV X-ray, the total energy deposition is 2614 keV, such that

$$(E_{photo} = 2614\,\mathrm{keV}) > (T_0 + FWHM = 2604\,\mathrm{keV}).$$

Therefore, only the tails of the photo-peak and Compton edge of the ^{208}Tl gamma rays will contribute to background events at the $T_0 \pm \frac{1}{2}FWHM$ (75%) window, when the energy resolution is 5% at T_0. However, as given in Table 5.4, this mode becomes the dominant source of background events in the $T_0 \pm FWHM$ (98%) window.

5.3 Background Estimation at Transition Energy T_0

The estimated contributions to background events from external gamma rays in the energy windows $T_0 \pm \frac{1}{2}FWHM$ and $T_0 \pm FWHM$ for the TPC with 5 atm of xenon is given in Table 5.4.

In the estimation, the gamma flux is calculated from the measured tunnel spectrum as shown in Fig. 5.2, shielded by 30 cm of lead. With this shielding, the intensity of 3 MeV gamma rays is attenuated by a factor of 4.5×10^{-7}. Energy resolution is 5% at 2.5 MeV, so that $FWHM = 124$ keV. From Monte Carlo stimulations, the efficiency for completely enclosing a single electron at 2.5 MeV is 15%, whereas that for pair production and double Compton scattering is 25%. Rejection efficiency for single electron events is 95%, also from Monte Carlo. The cross sections for various interactions are obtained from standard table[46]. The interaction length for the photon is taken to be 60 cm.

For Compton scattering, the energy distribution of the electron is taken to be uniform from zero to the Compton edge. The background estimation involves the summation of a rapidly diminishing series, each term of which represents the contribution from incident photons of a certain energy. The terms are insignificant for photon energy above 2.7 MeV.

Contributions to background events from internal radioactive contaminants are difficult to estimate at this stage. From Table 5.4, one sees that the background events from external gamma rays can be kept at the level of a few per year in the $T_0 \pm FWHM$ window by 30 cm of lead shieldings. This means that understanding and minimizing internal radioactive sources is crucial for the success of the experiment.

5.4 Estimated Lifetime Limits for $0\nu\beta\beta$ in ^{136}Xe

For a system with energy resolution $FWHM$ at transition energy T_0, and

a fiducial number of N ^{136}Xe atoms, the lifetime limit of $0\nu\beta\beta$ in t years of run time is

$$T_{\frac{1}{2}}^{0\nu} > \ln 2 \frac{N\,t}{S_u}$$

where S_u is the upper limit for the signal in the $(T_0 \pm \frac{1}{2}FWHM)$ energy window. A discussion of the evaluation of S_u is given in Appendix 5.

From the background event estimates in Section 5.3, one gets $B_0 = 1.04$ expected background in the 0ν energy window in one year of run time, ignoring contributions from internal sources. As an illustration, if we observed $C = 1$ counts in that range, then from Fig. A5.1, one obtains $S_u = 3.5$ at a 90% confidence level. In natural xenon at 5 atm, the fiducial number of ^{136}Xe (8.9% isotopic abundance) is $N{\sim}6.1 \times 10^{23}$, so that

$$T_{\frac{1}{2}}^{0\nu}(8.9\%\,^{136}\mathrm{Xe}) > 1.2 \times 10^{23}\,\mathrm{yr}$$

in one year of run time. With 60% enrichment, $N{\sim}4.1 \times 10^{24}$, giving

$$T_{\frac{1}{2}}^{0\nu}(60\%\,^{136}\mathrm{Xe}) > 8.1 \times 10^{23}\,\mathrm{yr}\,.$$

The translation from $T_{\frac{1}{2}}^{0\nu}$ to a limit for $\langle m_\nu \rangle$ depends on which specific calculation one chooses. Consider the mass mechanism for $0\nu\beta\beta$, that is,

$$T_{\frac{1}{2}}^{0\nu}\,\langle m_\nu \rangle^2 = \text{constant}\,,$$

one gets for one year run time in 60% enriched xenon,

$$\text{Vogel[13]}: \qquad \langle m_\nu \rangle < 2.8\,\mathrm{eV} \quad .$$

These numbers are competitive with those from the ^{76}Ge experiments[16], which give

$$T_{\frac{1}{2}}^{0\nu}(^{76}\mathrm{Ge}) > 1.2 \times 10^{24}\,\mathrm{yr}\,,\ \text{implying}$$

$$\text{Vogel[13]}: \qquad \langle m_\nu \rangle \ < \ 2.8\,\text{eV} \quad .$$

Conversely, for comparison, in order to reach a lifetime limit of

$$T^{0\nu}_{\frac{1}{2}}(60\%\,^{136}\text{Xe}) \ > \ 10^{23}\,\text{yr}$$

in one year of run time, which is already better than the best measured limit so far ($T^{0\nu}_{\frac{1}{2}} > 2.0 \times 10^{22}\,\text{yr}$, by the Milano MPC), one requires

$$S_u \ = \ 28\,,$$

which is in the large C regime (Case II in Appendix 5). If the background is flat in the range of interest, one can assume $B_0 = C$ and $\sigma_B^2 \ll C$. Following the formula given in Appendix 5, one gets

$$1 - CL \ = \ I(\frac{S_u}{\sqrt{C}})/I(0)$$

where $I(z)$ is the error function. A confidence level of 90% implies

$$\frac{S_u}{\sqrt{C}} \ = \ 1.65\,,$$

or $C = 288$. The experiment should be able to reach this background range with a wide margin.

Reaction	$T_{\frac{1}{2}}$ (day)	E_γ (MeV) [> 1 MeV only]	Branching Ratio (%) [> 1% only]
$^{63}Cu(n,\alpha p)^{59}Fe$	44.5	1.099	56.5
		1.292	43.2
$^{63}Cu(n,\alpha+4n)^{56}Co$	78.8	1.037	14.00
		1.175	2.28
		1.238	67.60
		1.360	4.33
		1.771	15.70
		2.015	3.08
		2.035	7.89
		2.599	16.90
		3.010	1.00
		3.202	3.04
		3.253	7.41
		3.273	1.75
$^{63}Cu(n,\alpha)^{60}Co$	1934.5	1.173	100
		1.332	100

Table 5.1 Long lived isotopes induced by cosmic ray neutrons in copper. Only those gamma rays with energies above 1 MeV and branching ratios above 1% are listed.

Parent	Daughter	Half-life	Decay Mode	Q Value (MeV)
^{238}U	^{234}Th	4.47×10^9 y	α	4.270
^{234}Th	^{234}Pa*	24.10 d	β^-	0.183
^{234}Pa*	^{234}Pa	1.18 min	IT (0.13%)	0.08
^{234}Pa*	^{234}U	1.18 min	β^- (99.87%)	2.207
^{234}Pa	^{234}U	6.70 h	β^-	2.287
^{234}U	^{230}Th	2.45×10^5 y	α	4.856
^{230}Th	^{226}Ra	8.0×10^4 y	α	4.771
^{226}Ra	^{222}Rn	1600 y	α	4.871
^{222}Rn	^{218}Po	3.83 d	α	5.591
^{218}Po	^{214}Pb	3.05 min	α	6.115
^{214}Pb	^{214}Bi	26.8 min	β^-	1.024
^{214}Bi	^{214}Po	19.7 min	β^-	3.270
^{214}Po	^{210}Pb	163.7 μs	α	7.834
^{210}Pb	^{210}Bi	22.26 y	β^-	0.063
^{210}Bi	^{210}Po	5.01 d	β^-	1.161
^{210}Po	^{206}Pb	138.38 d	α	5.408

Table 5.2a The ^{238}U decay chain. The lower part of the table represents decays from the daughter nuclei of ^{222}Rn.

Parent	Daughter	Half-life	Decay Mode	Q Value (MeV)
^{232}Th	^{228}Ra	1.41×10^{10} y	α	4.081
^{228}Ra	^{228}Ac	5.76 y	β^-	0.046
^{228}Ac	^{228}Th	6.13 hr	β^-	2.137
^{228}Th	^{224}Ra	1.91 y	α	5.520
^{224}Ra	^{220}Rn	3.66 d	α	5.789
^{220}Rn	^{216}Po	55.6 s	α	6.405
^{216}Po	^{212}Pb	0.15 s	α	6.907
^{212}Pb	^{212}Bi	10.64 h	β^-	0.573
^{212}Bi	^{212}Po	60.60 min	β^- (64.0%)	2.246
^{212}Bi	^{208}Tl	60.60 min	α (36.0%)	6.207
^{212}Po	^{208}Pb	0.30 μs	α	8.954
^{208}Tl	^{208}Pb	3.05 min	β^-	2.377

Table 5.2b The ^{232}Th decay chain. The lower part of the table represents decays from the daughter nuclei of ^{220}Rn.

a)

E_γ (MeV) [> 1 MeV only]	Flux deduced from Measurements (day^{-1} cm^{-2})
1.120	11396 ± 1841
1.155	1402 ± 240
1.238	5644 ± 693
1.281	757 ± 156
1.378	3220 ± 304
1.385	762 ± 117
1.402	1246 ± 144
1.408	2223 ± 220
1.509	2505 ± 307
1.539	420 ± 96
1.661	1058 ± 213
1.730	3124 ± 695
1.765	16986 ± 3975
1.838	418 ± 129
1.847	2354 ± 598
2.119	1342 ± 289
2.204	6089 ± 1070
2.293	286 ± 95
2.448	1975 ± 234

b)

E_γ (MeV) [> 1 MeV only]	Flux deduced from Measurements (day^{-1} cm^{-2})
1.588	1005 ± 180
1.621	1795 ± 314
1.630	1597 ± 290
1.638	575 ± 124
2.615	52001 ± 5481

Table 5.3 Gamma fluxes deduced from the germanium measurements at Gotthard for the a) ^{238}U, and b) ^{232}Th decay chain.

E_γ (MeV) [> 2.5MeV only]	Branching Ratio per ^{214}Bi decay (%)
2.506	0.006
2.551	4×10^{-4}
2.605	4.6×10^{-4}
2.631	9×10^{-4}
2.662	3×10^{-4}
2.695	0.033
2.699	0.0028
2.719	0.0018
2.770	0.026
2.786	0.006
2.827	0.0025
2.861	3.5×10^{-4}
2.880	0.0094
2.894	0.0065
2.922	0.016
2.929	0.0012
2.935	5.8×10^{-4}
2.940	0.0017
2.979	0.015
2.989	0.0011
3.000	0.009
3.054	0.023
3.082	0.0044
3.092	5.2×10^{-4}
3.136	3.5×10^{-4}
3.143	0.0016
3.161	5.2×10^{-4}
3.184	0.0015
3.233	2×10^{-4}
3.270	1×10^{-4}
Total :	0.173

Table 5.3c A list of all gamma rays with energies above 2.5 MeV in the ^{238}U decay chain. All the lines follow after the beta decay of ^{214}Bi ($Q_{\beta^-} = 3.28$ MeV, branching ratio 97.8%). There is no gamma ray above 2.615 MeV in the ^{232}Th decay chain.

Interaction	Number of Events per Year	
	$T_0 \pm \frac{1}{2}FWHM$	$T_0 \pm FWHM$
Compton Scattering	0.11	0.22
Photoelectric Effect	0.22	0.44
Double Compton Scattering	0.13	0.25
Pair Production	0.10	0.20
Beta Decay of ^{137}Xe	0.19	0.39
^{208}Tl 2614 keV Induced	0.29	1.32
Total:	1.04	2.82

Table 5.4 Background events estimation at $T_0 = 2.48$ MeV for the TPC with 5 atm of xenon. Only backgrounds induced by external sources are considered here.

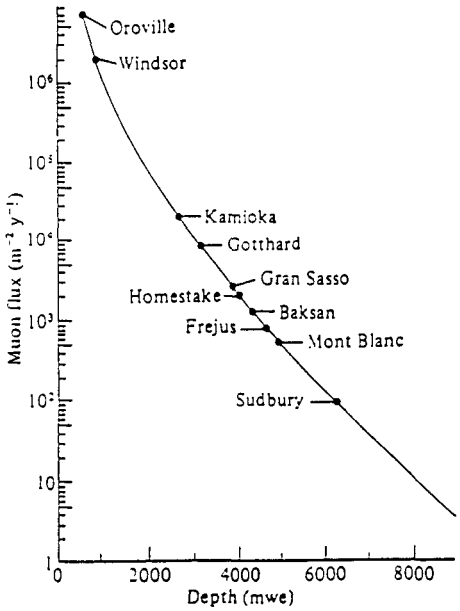

Figure 5.1 Cosmic ray muon flux at various underground laboratories.

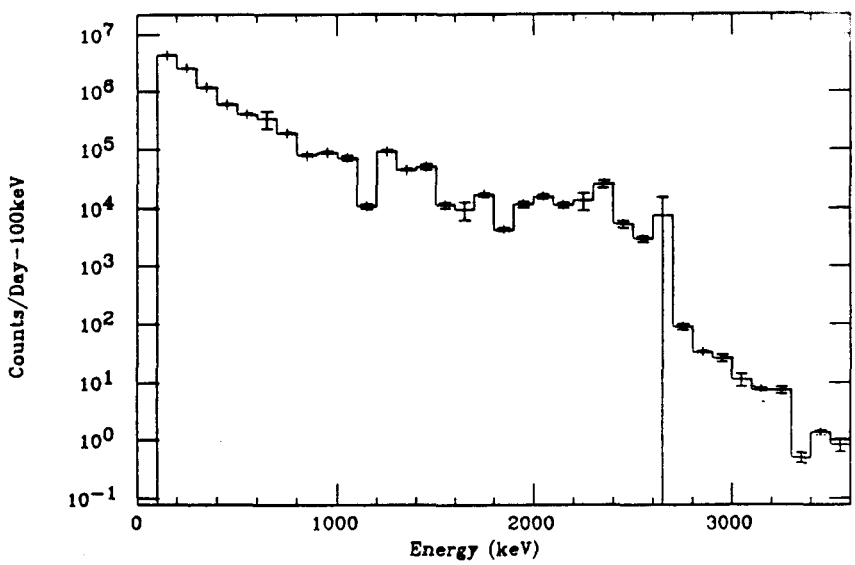

Figure 5.2 Background continuum spectrum measured by the Germanium experiment at Gotthard. It represents the flux of gamma rays being Compton scattered from the rock before hitting the detector.

CHAPTER 6

PERFORMANCE

6.1 Energy Resolution

6.1.1 Prototype Anode

The prototype anode system was constructed and tested at Caltech, to investigate the effects of various parameters on the track quality and energy resolution of the TPC, as well as to learn about the specifications of the final anode system. The design of this prototype and the measurements have been discussed in detail in Ref. 30. The main conclusions are summarized in this section.

The best energy resolution achieved to date is 11% at 1 MeV, with 2.5 atm of xenon. A ^{207}Bi internal conversion source was placed at the center of the cathode, and sampling was triggered by trajectories originating from that point. At this pressure, the length of a 1 MeV electron track is about 60 cm. Therefore the entire anode plane is well covered, and the measurement is sensitive to the gain variation across the plane. The Si-Li and TPC spectra are shown in Figs. 6.1a and 6.1b, respectively. The width of the 1 MeV peak is about 14%, but since there are two electron lines at 975 keV and 1048 keV in an intensity ratio of 3:1, the actual energy resolution is 11%. Assuming $\frac{1}{\sqrt{E}}$ scaling, the energy resolution at 2.5 MeV is expected to be about 7%.

In the course of these studies, it was found that the major determining factor to the energy resolution is the gain uniformity across the entire anode plane. This is also the conclusion from the measurements using a MWPC as described in Ref. 20. The main contribution to this gain variation comes from

insufficient geometrical precision, and the presence of insulating surfaces.

To illustrate this point, energy spectra of alpha particles have been taken. Eight ^{228}Th sources were placed at one quadrant of a specially designed cathode surface. These sources emit alpha particles of energy 6.1 MeV and 8.8 MeV, in the intensity ratio of 35% to 65%, respectively. The cathode was rotated by 90° every time, and the four spectra taken for the four quadrants are shown in Figs 6.2a-d. The fill gas is 2.5 atm P-10 (argon with 10% methane) so that the charge depositions are well localized. Operating voltage for the anode was much lower than normal, to prevent the high charge density from the alphas from saturating the electronics or producing enormous space charge effects. The spectra are all different, and in each of them, multiple peaks are observed. This is a clear signature that the proportional gain varied from point to point on the anode plane.

Charge multiplication is suppressed near an insulating surface. Figure 6.3 shows the histogram of the activity of the XY channels for the prototype anode system. The sense wires are parallel to the X channels. The general profile agrees with what is expected: the activity depends on the length of the channels, and peaks at the center. The seven "fringes" in the Y-histogram correspond to the suppression of charge multiplication due to the presence of the seven supporting nylon wires orthogonal to the sense wires (hence parallel to the Y channels). The effect extends over about six channels (or 2 cm) for each nylon wire. Therefore, the edge of the anode frame must be about 0.5 cm or more away from the veto ring and the active region of the chamber to avoid any edge effect. Such fringes have disappeared with the final anode that does not have supporting nylon wires. It can also be seen that such histograms are useful for tracing down noisy or inactive electronics.

In principle, one can have a map of gain non-uniformity for the anode plane, and then correct subsequent data accordingly. We have tried this procedure but there are no noticeable improvements in the energy resolution measurements. Several reasons may account for that. In our case, where the gain variations are measured by placing alpha sources on 32 locations on the cathode, each position represents an average over an area of 10 cm by 10 cm. This bin size is large enough to average out any possible improvements. In addition, the variations may change with different operating conditions such as pressure and anode voltage. Software programs to correct the gain through the (X,Y) co-ordinate of the tracks are also far from trivial. When the trajectory crosses a certain Z-plane more than once, certain assumptions have to be made to divide the charge depositions between the various positions, and this further reduce the validity of the correction.

6.1.2 Final Anode System

The major improvements of the final anode system, as described in Section 3.3.2, are better geometrical precision (to 25 μm), the lack of supporting insulating wires, and the use of low background materials in the construction. We expect that it will improve both the energy and tracking aspects of the measurement. However, when it is finished, the experiment has proceeded to a point where it is impractical and risky to put alpha or internal conversion sources inside the TPC, as we did with the tests of the prototype. This leads to complications in the analysis of the spectra, especially in the MeV region.

Energy spectra recorded for low energy gamma sources (^{133}Ba and ^{57}Co) are displayed in Figures 6.4a-c, for 2 atm P-10, 1 atm and 5 atm xenon,

respectively. In the case of P-10, the 8 keV copper X-rays are well resolved, whereas in the xenon case, the lowest peaks correspond to the 30 keV xenon X-rays, the middle ones are the escape peaks (energy of the photoelectrons), and the highest ones are the full energy peaks (81 keV for ^{133}Ba and 122 keV for ^{57}Co). Note that ^{133}Ba has a much weaker line at 350 keV, giving rise to an end-point, and ^{57}Co has one at 136 keV which is not resolved but shows up when the spectrum is fitted to several gaussians. From these measurements, the resolution is about 12% at 100 keV (width is 10 keV for the ^{133}Ba 81 keV line, and 15 keV for the ^{57}Co 122 keV line).

The energy spectrum for a ^{22}Na source is depicted in Fig. 6.4d, with a resolution of 10% (width 50 keV) for the 511 keV line. There is a change of slope at about 1.08 MeV, corresponding to the Compton edge of the 1.28 MeV gamma ray. The spectrum extends as far as 1.6 MeV because of the gamma interactions in coincidence. The absence of a photo peak for the 1.28 MeV line requires further thought. At this energy, the Compton cross-section is a factor of ten larger that the photo cross-section. Therefore, multiple scattering of the photons may smear out a less intense peak, especially when the expected resolution is only about 8%. As a comparison, photo and Compton cross sections are comparable at 500 keV, and yet the 511 keV peak is only barely resolved from the background continuum. Monte Carlo studies will be performed to investigate this point.

The spectra presented above were taken by integrating the anode current pulse with an integrator, the output of which is fed to an MCA through a spectroscopy amplifier. An alternative way is to digitize the current pulse with a Transient Recorder, and integrate that numerically by software, a way that can be directly compared to TPC events. For low energy (and hence

short) pulses, both methods give comparable resolution, although the spectra from software integration takes much longer to collect, because of dead time. However, the analogue integration method gives better resolution at higher energy, for instance in the case of the 511 keV peak in ^{22}Na. There is more accurate sampling in the analogue case - measuring one number integrated electrically is better than adding up hundreds of numbers that digitize the pulse. Pursuing this line, plans are being made to expand our data acquisition system. An ADC will be added to the CAMAC bus to record the integrator output, so that there will be two different energy measurements, based on the same anode pulses, for each event.

6.2 Track Reconstruction

6.2.1 Layout

All the TPC trajectories discussed in this section are displayed in the format described below. For each event, the XZ and YZ projections are shown, and on the right is the time evolution of the anode signals (charge collected at the anode after multiplication). The control parameters (like memory size) are given on the lower right corner, the operating conditions on the upper left corner, while the date and time are on the upper left corner. The large black dots on the tracks are due to signals above an upper discriminator threshold and correspond to "charge blobs." The full range for X and Y is 60 cm (diameter of the active volume) in all cases. The scale for Z differs with each event, depending on the drift velocity which varies with operating conditions. The display is upside down relative to the actual experimental set-up. Since there is no absolute time-zero trigger, Z=0 corresponds to the first arrival of

the signals. Except for the alpha particle event in Fig. 6.5, all other events shown here were recorded during background run at Gotthard with 5 atm of depleted xenon and lead shieldings fully installed. The vertical scale is 10 cm per unit.

6.2.2 Alpha Particles

A typical alpha event is shown in Fig. 6.5. It was recorded at 0.5 atm xenon, at an anode voltage much lower than the operational one (or else the huge charge depositions will saturate the electronics). The alpha particle is emitted from the tin-lead solder on the anode frame, following the decay of ^{210}Pb and is 5.4 MeV in energy. The length of the alpha particle is 6 cm, consistent with expectations derived from the tabulated value[47].

6.2.3 Cosmic Rays

Various events due to cosmic rays are shown in Fig. 6.6a-c. Figure 6.6a shows a single muon event. Fluctuations of charge depositions (dE/dx) along its path are conspicuous. Figure 6.6b shows another muon event, with the emission of an energetic delta electron, which stops in a huge charge blob. There is a small isolated charge deposition, due to capture of low energy photon from X-rays or bremsstrahlung. Figure 6.6c depicts a cosmic ray shower. The display is upside down so that the shower cone is pointing "upwards." Information from both XZ and YZ enables us to have a one-to-one matching of the tracks in both projections (except in some exceptionally messy events). The different "prongs" of the showers are labelled to illustrate this point.

6.2.4 Single Electrons

Two examples of single electron events are shown in Fig. 6.7a-b. The trajectories show the expected features: relatively straight and minimum ionizing in the beginning, but staggered track with high charge depositions at the end. The event in Figure 6.7b is in coincidence with a low energy photon from X-rays or bremsstrahlung.

6.2.5 "Two-Electron" Events

Figures 6.8a and 6.8b are examples of "two-electron" events. Both ends of the trajectories exhibit the characteristic "end features": charge blobs and staggered tracks. In both cases, the energy depositions are about 4 MeV. The sharp vertices near the central portion of the trajectories suggest that they are probably events due to pair production.

6.2.6 Multiple Compton Scattering

Figure 6.9 is an event characterized by numerous isolated small charge depositions, together with one more energetic electron. A probable interpretation for this is multiple Compton scattering from an incident high energy gamma ray. The total energy deposition is about 4 MeV.

6.2.7 Cascade in Decay Chain

Figure 6.10 shows a beta decay followed by emission of an alpha particle

after 50 μs, at the same (X,Y) coordinate. This can be interpreted as the beta decay of ^{214}Bi, followed by the alpha decay of ^{214}Po (half-life 164 μs) in the ^{238}U series, as discussed in Section 5.2.1. Note that the pulse shape and "trajectory" of the alpha particle is an artifact due to the saturation of electronics. To see real alpha tracks like the one shown in Fig. 6.5, one needs to operate at a much lower anode voltage, and at a low pressure.

6.2.8 Track/Blob Distinction

A program was developed to enable users to locate the ends of a trajectory manually, and then the charge depositions (as represented by the number of hits from the discrimination) in a box centered at the ends are calculated. This procedure was applied to 350 single electron events from a ^{207}Bi internal conversion source placed at the center of the cathode (so that one can differentiate exactly the *"beginning"* and *"end"* of a track). The results are shown in Fig. 6.11a-b. These are to be compared to the Monte Carlo results in Fig. 3.3a-b. It can be seen that the *"end"* of an electron trajectory is readily distinguishable by its much larger charge deposition, compared to the *beginning*. From the overlap between the two histograms, the rejection efficiency of a single electron, based on the signature of having only one charge blob at one end, should be about 95%. It is anticipated that a similar procedure will be adopted to analyze and identify events at the 0ν energy region.

6.2.9 Efficiency of Veto Ring

By comparing the trigger rate with the veto line ON/OFF for "inclined muons" (events triggered by coincidence signals from two scintillators whose

line of sight makes an angle with the TPC axis), it can be concluded that the efficiency of the veto ring is at the range of 95%.

6.3 Stability

One of the important requirements of the experiment is that the TPC must be able to run continuously and unattended in the Gotthard Tunnel Laboratory, with minimal maintenance. Operating conditions like pressure, temperature, gas purity and gas composition must be kept stable for an extended period of time. The stability of these conditions can be monitored in the measurements of proportional gain, drift velocity and the attenuation of drifting electrons, which are described in the following sections.

6.3.1. Proportional Gain

The stability of the overall gain, due to charge multiplication and electronics, is monitored regularly by the peak position of the 30 keV xenon fluorescent X-rays. The dE/dx value of minimum ionizing muon events provides an additional on-line consistency checks. Typically, at the Gotthard Laboratory and within the lead shielding, the temperature can be kept steady to 1 °C, and the gain is stable to a few percent.

6.3.2 Length of Muon Signals

The length of the vertical muon signals indicates the time taken by the secondary electrons to drift from the cathode to the anode (a distance of 70

cm). The drift velocity is related to this time by

$$v_d = \frac{\text{Drift Distance}}{(\text{No. of Time Bins})(\text{Period of Clock})}.$$

A program was developed to measure the length of muon signals in units of time bins. Fig. 6.12 shows the results with both clean (that is, under continuous purification) and "dirty" xenon (left without purification for two days). The spectrum for clean gas has a well defined peak, corresponding to a drift velocity of 1.48 cm μs^{-1}. The one with dirty gas does not show any peak structure. The length signals are shorter, indicating attenuation of the drifting electrons. However, the cutoffs for maximum drift time are the same in both cases, showing that the drift velocity has not changed. Variations in the drift velocity will give rise to a shift in the peak altogether.

6.3.3 Anode Statistics for Muon Events

Another program was developed to collect the statistics of muon events observed at the anode with respect to Z, that is, to histogram the anode signals as a function of time (Z). A typical spectrum for this analysis is shown in Fig. 6.13a. The fill gas is P-10 fresh from cylinder. The time duration between the two edges is a measure of the drift velocity of the gas. which is 5.4 cm μs^{-1} in this case. The histogram is slightly higher at the low-Z side because some muon events are showers which give larger pulses at small Z (top part of TPC), like the one shown in Fig. 6.7c.

The slope of the histogram also gives a quantitative measure of the purity of the gas. Figure 6.13b shows the same measurement but with 2% of air mixed with the P-10. The attenuation of the drifting electrons is conspicuous.

In addition, such a change in gas composition also gives rise to a decrease in drift velocity, which becomes 4.38 cm μs^{-1} in this case.

6.3.4 Variation of Drift Velocity with Drift Voltage

Using the procedures described in the last two sections, one can determine the dependence of drift velocity on drift voltage. This variation gives information on the composition of the gas. The measurements for xenon-methane are given in Fig. 6.14a, and the 4% and 5% data points can be distinguished readily. A similar plot for P-10 is shown in Fig. 6.14b. The drift velocity is large and also saturates at a much lower voltage in the case of P-10.

6.4 Low Background Components

To minimize background due to internal radioactivity, the TPC is constructed from low background materials: OFHC copper for metallic components and Delrin for insulators. Other materials used constitute only a small proportion by mass, and have been tested for trace radioactivity with the low-background facility at Neuchâtel.

The detector used is a 90 cm^3 germanium crystal originally built as a prototype experiment to look for double beta decay in ^{76}Ge[44]. The crystal is housed inside lead and copper shielding, which are surrounded by veto panels to reject events due to cosmics. The volume inside the shieldings is constantly purged by nitrogen to get rid of the radioactive radon. The samples to be tested are placed inside the shielding directly facing the crystal. In an initial measurement, a source of known activity was placed at the same location for

future calibration. As an illustration, a typical spectrum is shown in Fig. 6.15. The lower and upper curves correspond to the background and the testing sample (in this case, a glass sample), respectively. Some of the more prominent gamma lines are identified. A sample is considered to be "clean" if the spectrum is consistent with the background after several days to one week of data taking. For the glass, it can be seen that the radioactivity from ^{40}K as well as the ^{238}U and ^{232}Th series is conspicuous. The concentration of potassium, uranium and thorium in the sample are 340 ppm, 280 ppb and 410 ppb, respectively.

The list of the materials used in the experiment, which have been tested clean, includes: Rexolite and epoxy for the XY pad, gold-plated tungsten wire, various components (epoxy, stainless steel pins, ...) of the anode frame, cables and mylar foils.

However, some samples have been shown to be dirty, and the details are described below.

1. *Lead bricks for the shieldings:* The lead gives a low energy bump up to several hundred keV in the Ge spectra, due to bremsstrahlung from the beta decay (end-point 1.16 MeV) following decays of ^{210}Pb (half-life 22.26 years). This will not be a problem because the photons produced are low energy and are further shielded by 5 cm of copper before entering the active volume of the TPC.

2. *Tin-lead solder:* There is again a low energy continuum above background, signifying the presence of ^{210}Pb. In addition, there is evidence of alpha particles emission from the solder on the anode frame, as displayed in Fig. 6.5. The (X,Y) co-ordinates of alpha events are clustered around the perimeter with two gaps, exactly the same pattern as the

solder pads of the grid wires. We expect the contribution to background events will not be serious. Only a tiny amount of solder is used (compared to the entire spool tested with the germanium detector), and so background induced by bremsstrahlung should not dominate. The alpha and beta emissions from the surface of the solder are short-ranged. Those from solder on the feedthroughs will not get into the active volume of the TPC, and for those from the anode frame, the event will be vetoed out by the veto ring.

3. *Resistors:* The 10 MΩ resistors on the field-shaping ring assembly are radioactive, showing both the ^{238}U and ^{232}Th series, as well as ^{40}K. This may be the dominant contribution eventually, and further work is under way to look for acceptable replacements. The design of the assembly is flexible enough that the resistors can be replaced with reasonable effort.

4. *O-rings:* The O-rings are radioactive in ^{40}K and the ^{238}U series, but not in the ^{232}Th series. Therefore, they will not contribute to the crucial 0ν region. The gamma background has a slightly less favourable solid angle of reaching the active volume (compared to the resistors), and is partially shielded by copper. However, their replacement will require a major effort.

5. *Getter Materials:* Although the getter materials are well outside the shielding, the uranium and thorium series have to be avoided because the radon outgassing may bring radioactive isotopes into the active volume of the TPC. The HYDROX getter is surprisingly bad in ^{235}U. However, there is no evidence of radon emission that would give rise to an increase in alpha events. The radon (^{219}Rn) of this series is short-lived (half-life 3.96 s), and the decay with highest Q value is a beta decay with

end-point 1.37 MeV. In comparison, the OXISORB getter is radioactive from measurements with the germanium detector in both the ^{238}U and ^{232}Th series, and shows signs of radon emission. In a test with 0.5 bar P-10 to look for "alpha-like" events (which also include some high voltage breakdown and cosmic ray induced activities), the singles and coincidence rates (with a 0.2 s time window) were measured before and after the gas was circulated through the getter. The results are shown in Table 6.1. The increase in the alpha singles rate is evidence of radon emission - radon isotopes in both chains decay by alpha emission. The singles rate did not return to the original level after circulation stopped, showing that the dominant radon emitted is long-lived (^{222}Rn from the ^{238}U series, of half-life 3.8 days). There was also an increase in coincidence rate, signifying emission of the ^{232}Th radon (^{220}Rn of half-life 56 s, whose decay is followed by another alpha emission with half-life of 0.14 s) as well, though with a lower rate. Based on this observation, the HYDROX getter is being used for the experiment.

	Counts per 100 s		
	Start	Circulation ON	Circulation OFF
Singles	15.0±0.7	19.9±0.7	19.8±0.8
Doubles (0.2 s window)	0.68±0.08	1.35±0.18	0.90±0.17
Randoms Expected	0.45±0.04	0.80±0.06	0.78±0.06

Table 6.1 Measured count rates for "alpha-like" pulses to test the radon emission from the OXISORB getter.

a)

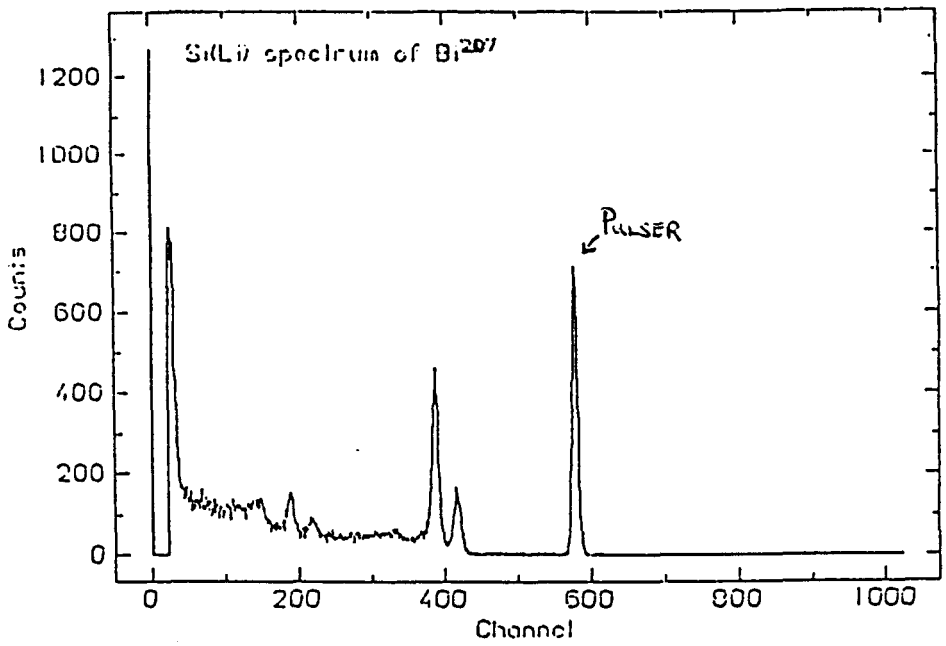

b)

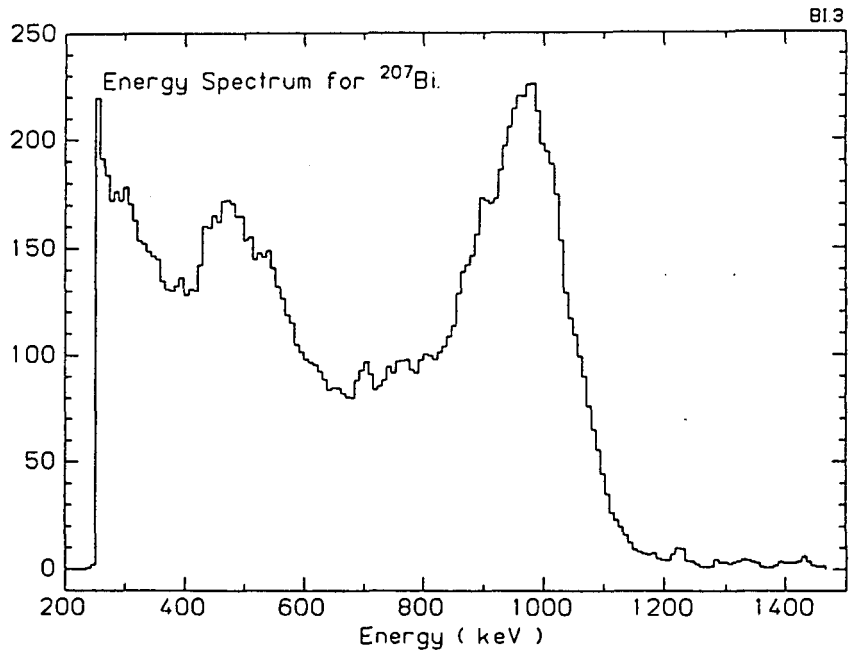

Figure 6.1 Energy spectra of the ^{207}Bi source with (a) a Si-Li detector, and (b) TPC prototype anode.

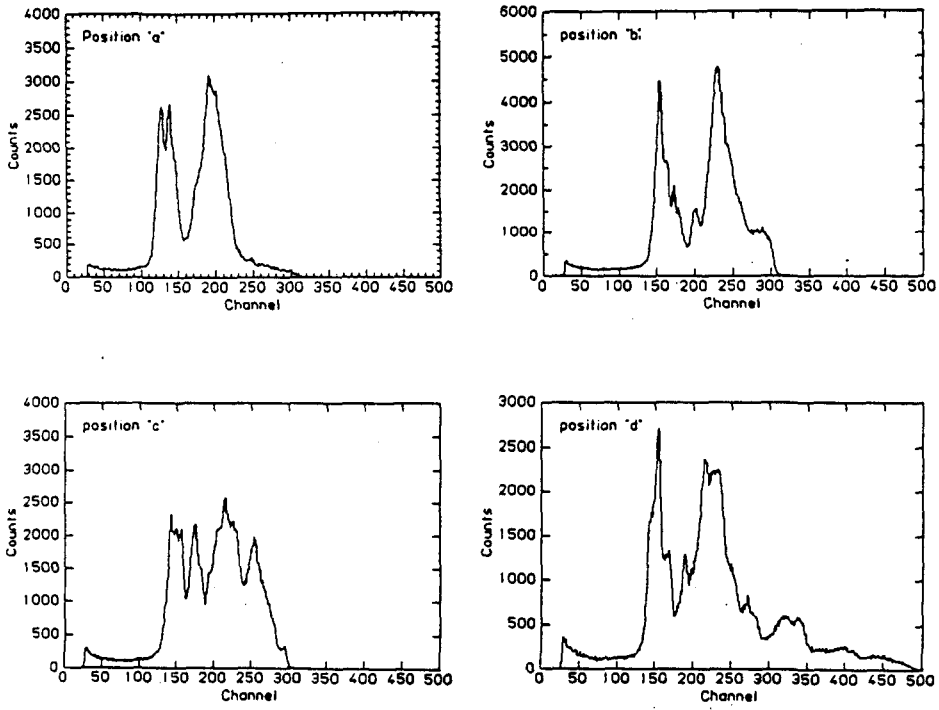

Figure 6.2 Energy Spectra of alpha particles from eight ^{228}Th sources : (a) to (d) are spectra with sources placed at the four quadrants. Fill gas is 2.5 atm of p10.

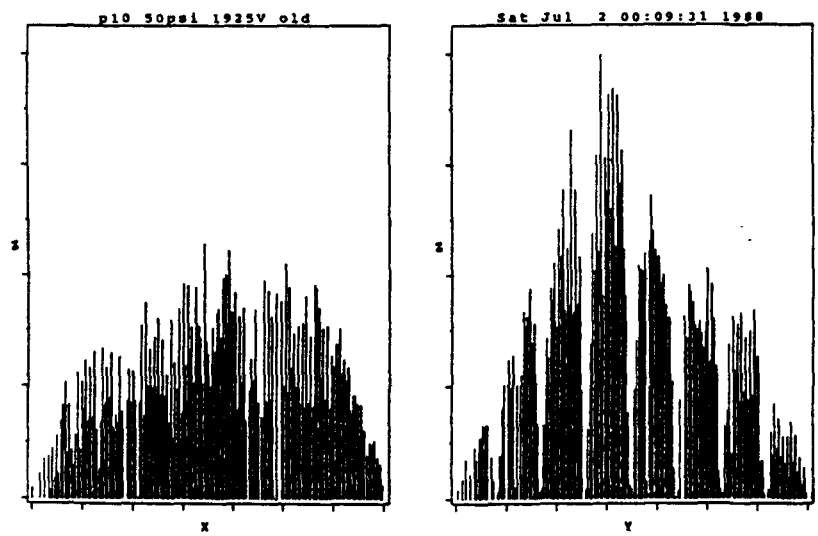

Figure 6.3 Histogram showing the activity of the X and Y channels for prototype anode. Effects from the seven supporting nylon wires are conspicuous.

4.a)

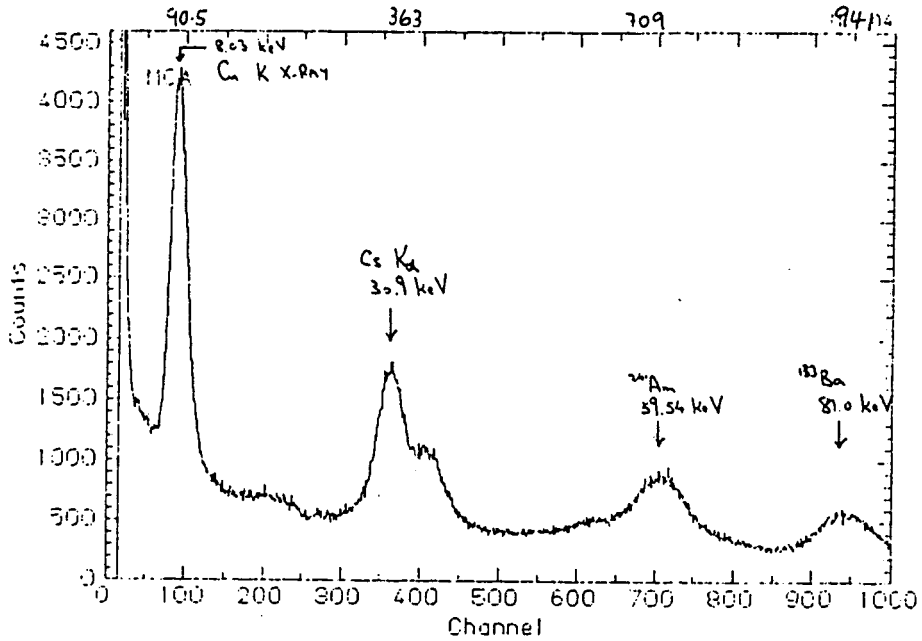
90.5
363
709
8.03 keV
Cu K X-Ray
Cs Kα
30.9 keV
241Am
59.54 keV
133Ba
81.0 keV
Counts
Channel

4.b)

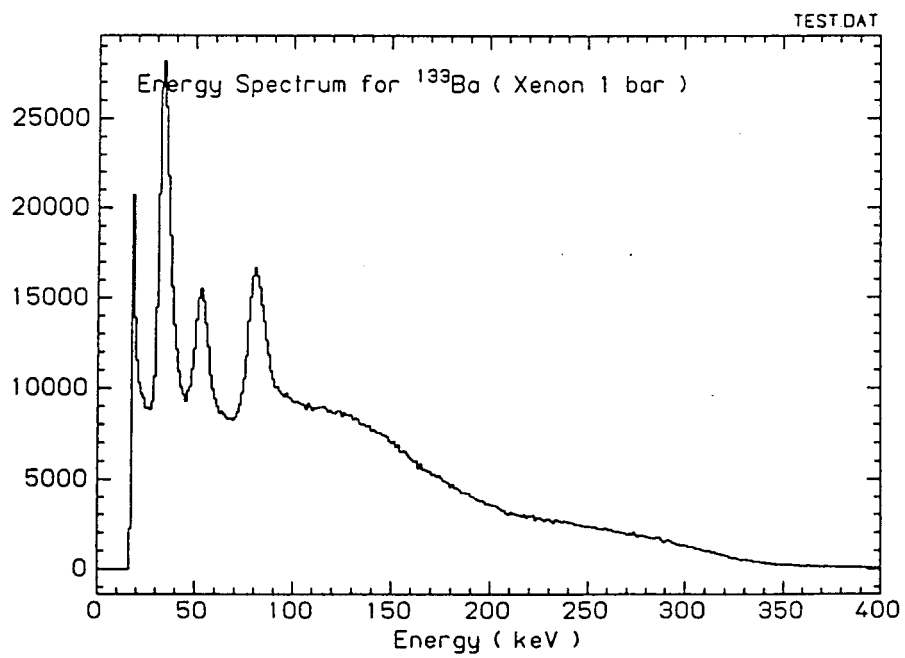
TEST.DAT
Energy Spectrum for 133Ba (Xenon 1 bar)
Energy (keV)

c)

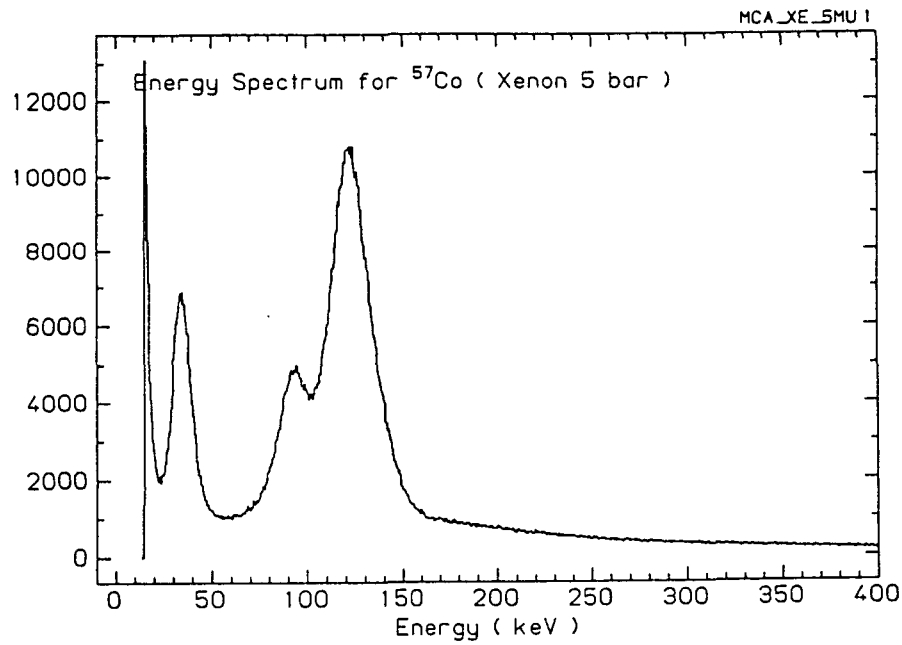

d)

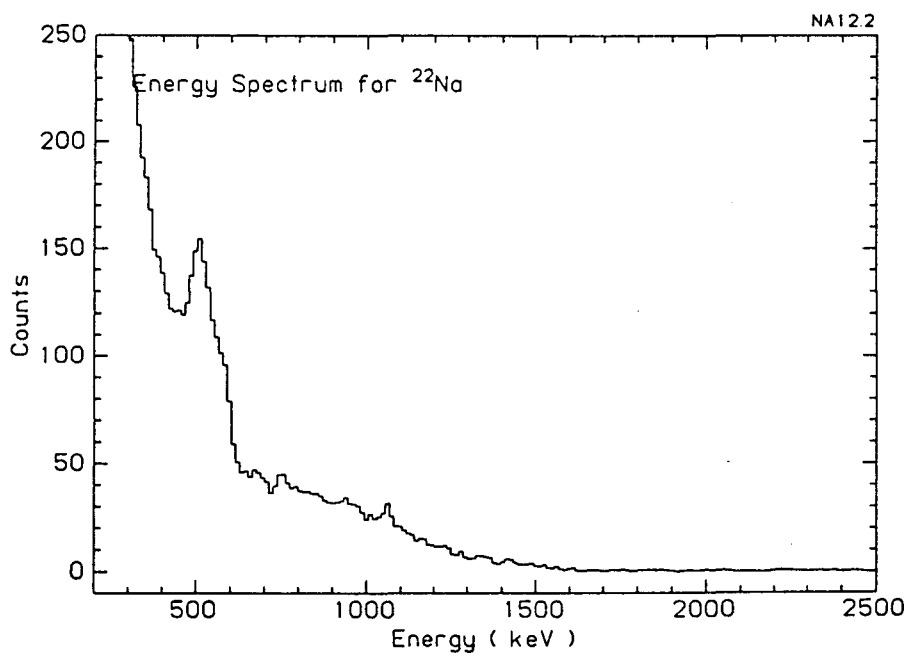

Figure 6.4 Energy spectra for the final anode: (a) ^{133}Ba and ^{241}Am on 2 atm P-10, (b)^{133}Ba on 1 atm xenon, (c)^{57}Co on 5 atm xenon, and (d) ^{22}Na on 5 atm xenon.

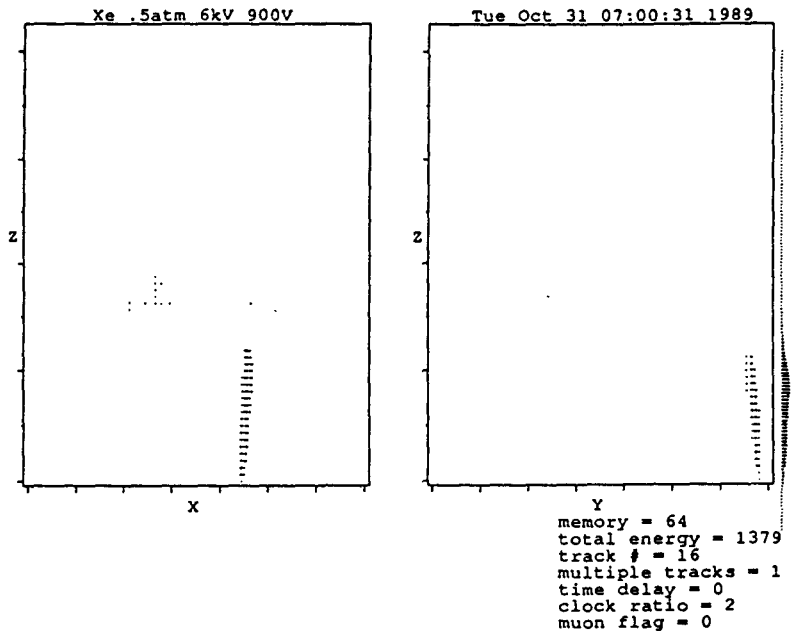

Figure 6.5 A typical alpha event, originated from solder on anode frame.

6.a)

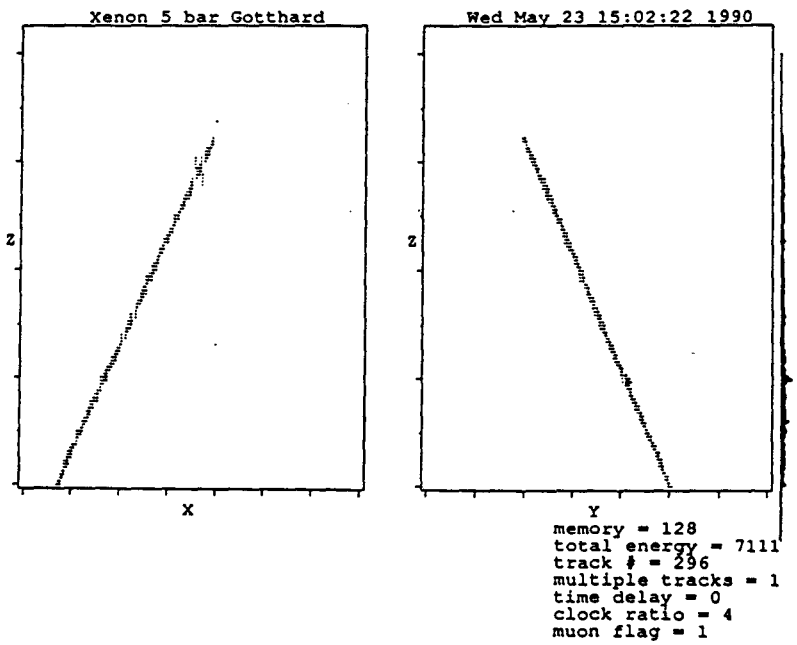

b)

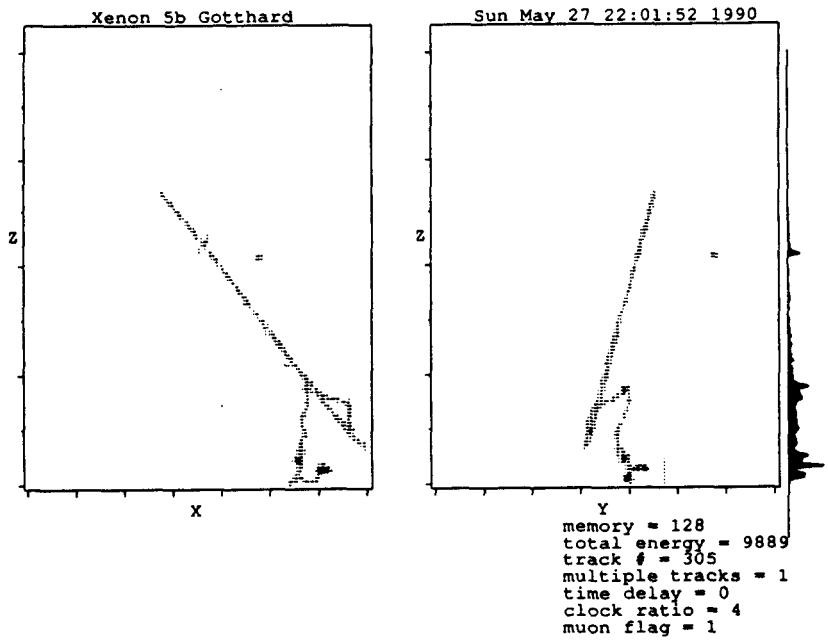

c)

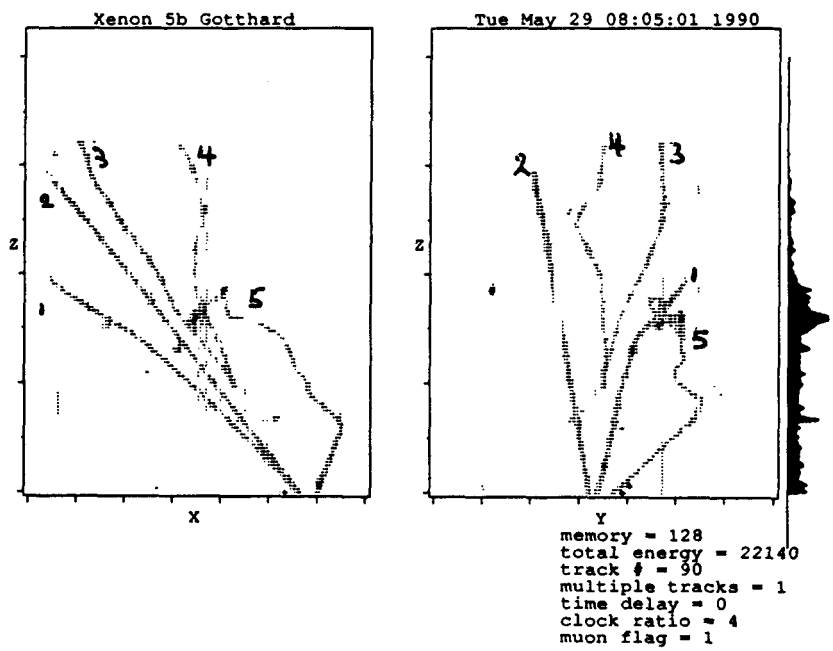

Figure 6.6 Typical cosmic ray events: (a) single minimum ionizing muon, (b) muon with energetic delta electron, and (c) shower.

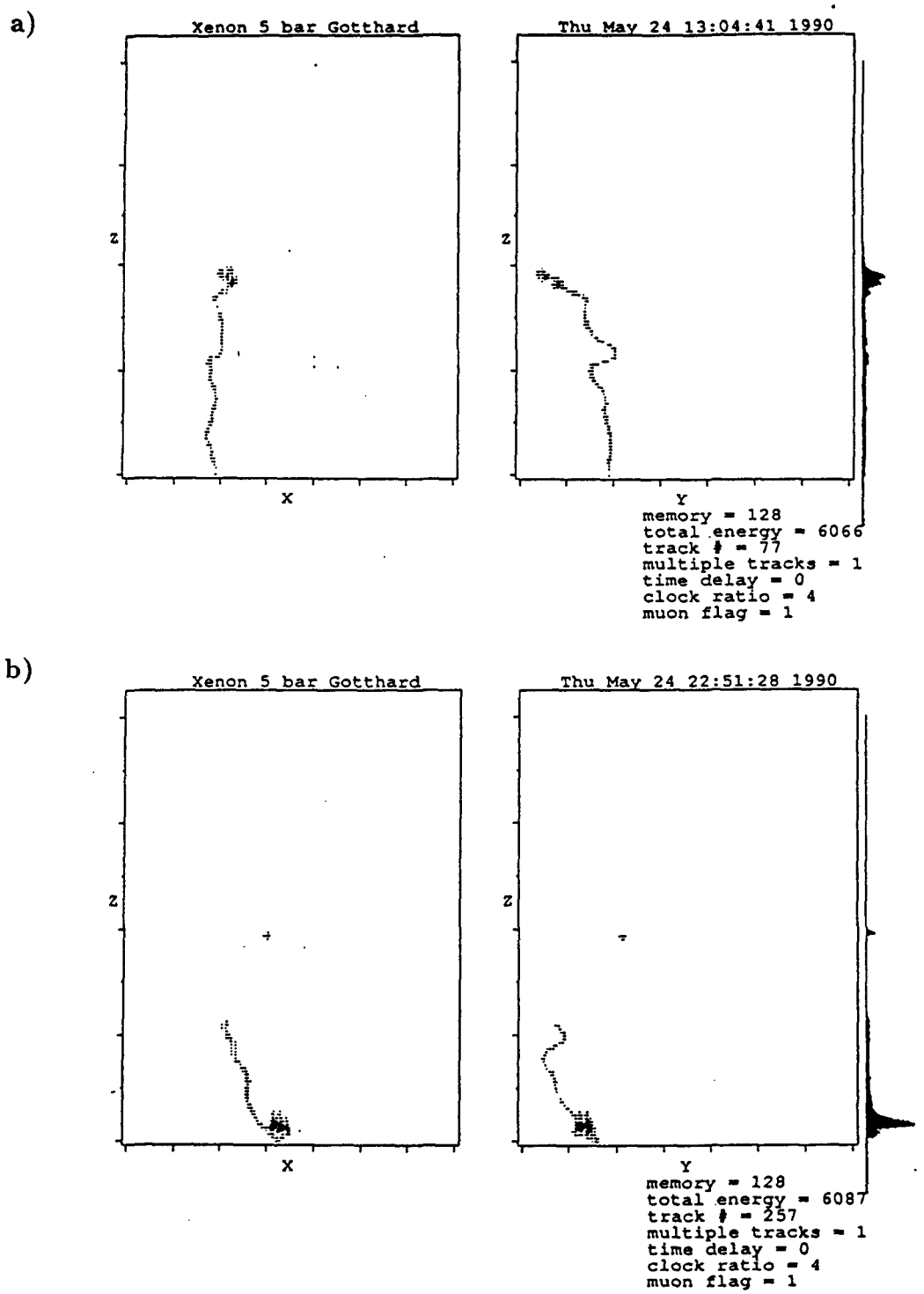

Figure 6.7 Typical single electron events.

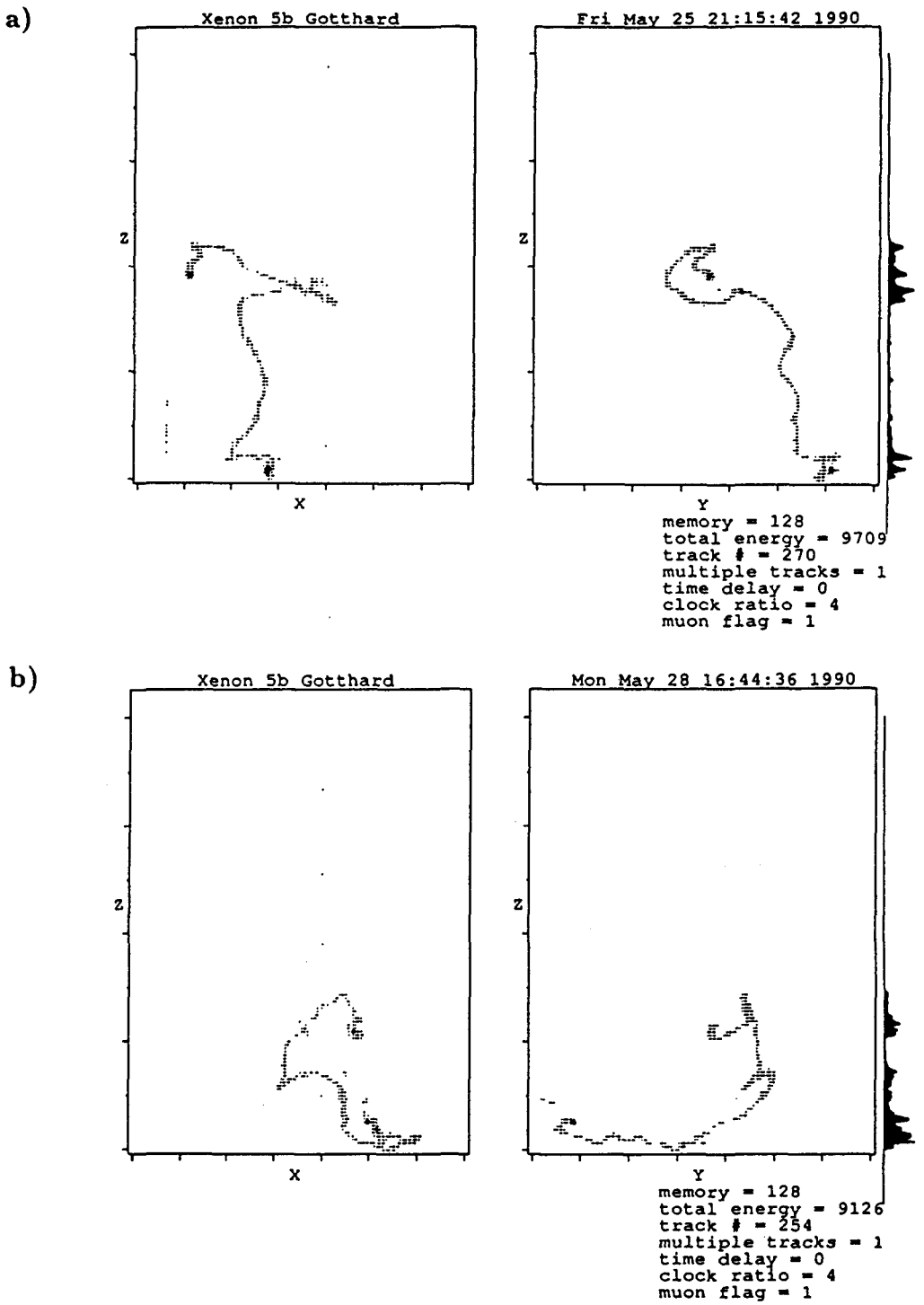

Figure 6.8 Typical "two electron" events.

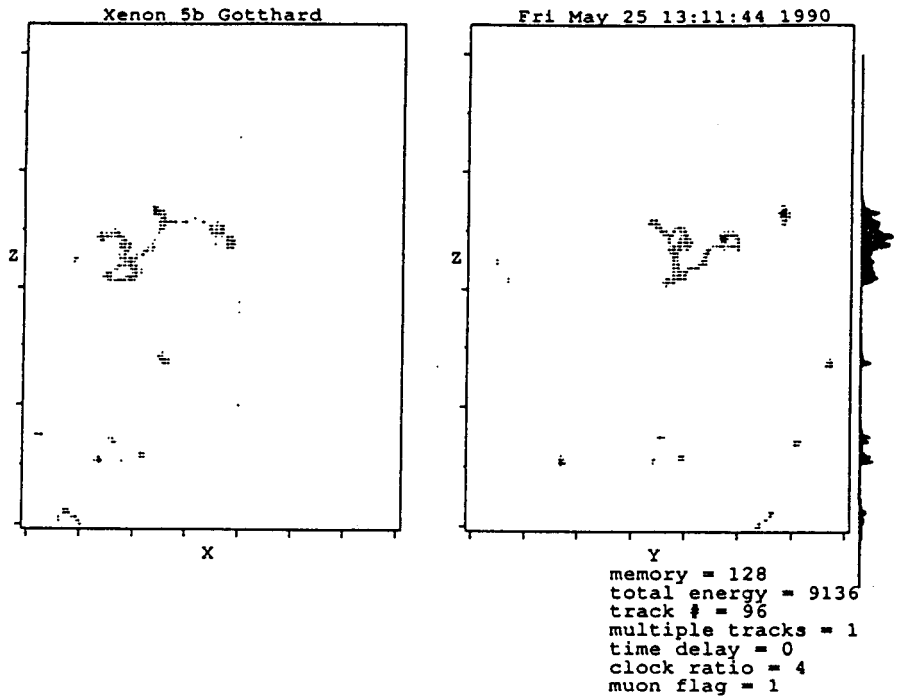

Figure 6.9 An example of a multiple Compton scattering event.

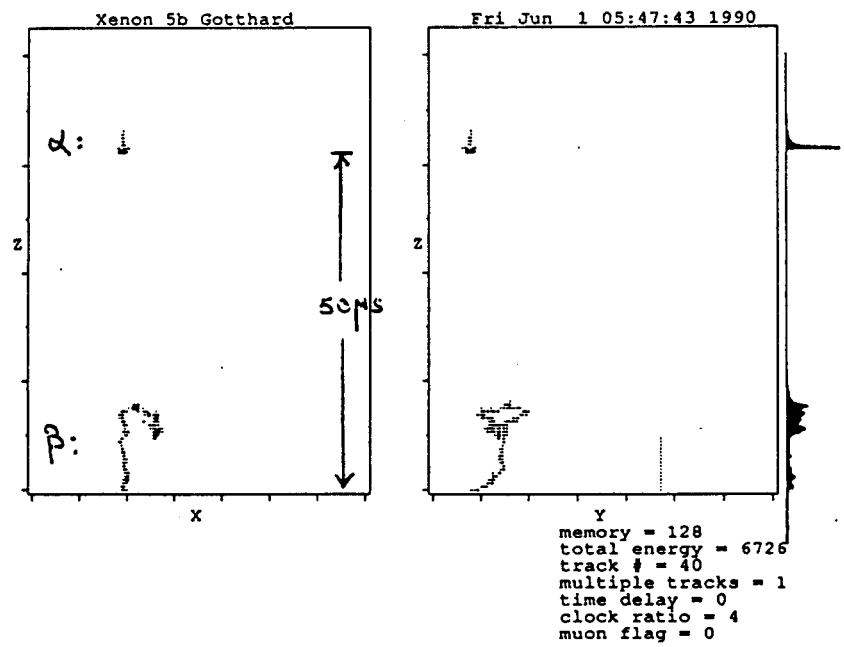

Figure 6.10 An example of a cascade event: beta decay followed by the emission of an alpha particle.

a)

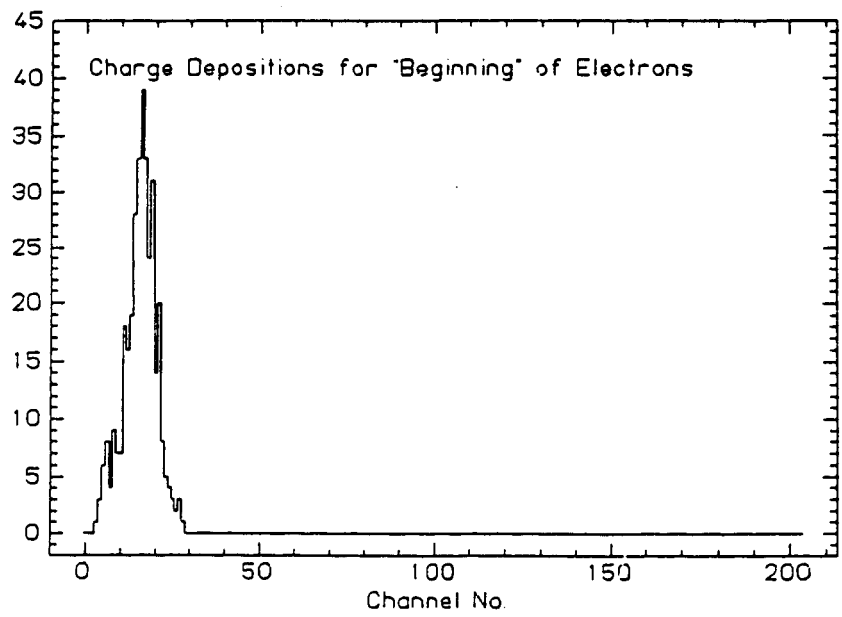

b)

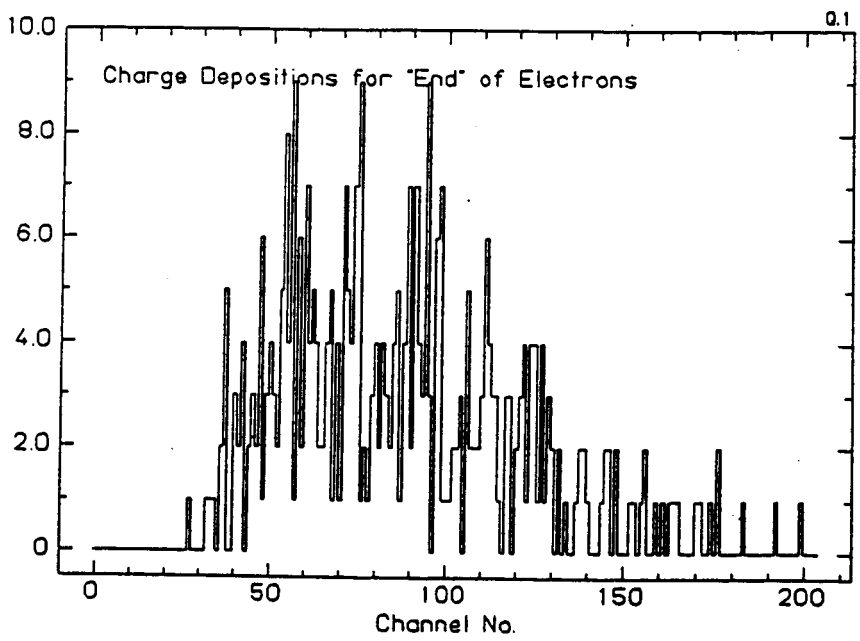

Figure 6.11 Charge depositions at the (a) beginning and (b) end of ^{207}Bi internal conversion electrons. A volume of 2 cm^3 was sampled. Weight of second level trigger was 10, compared to 1 for the first level trigger.

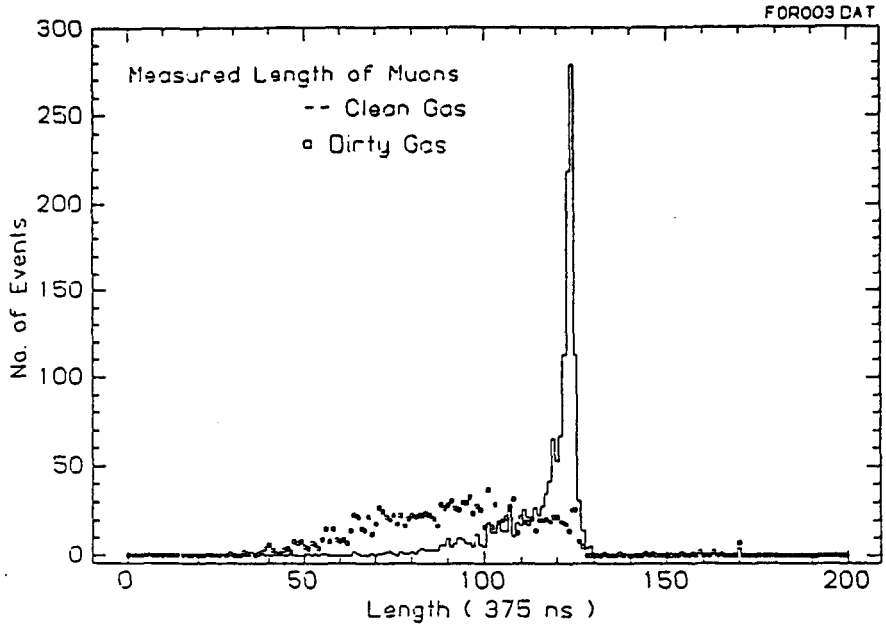

Figure 6.12 Spectrum for the length of vertical muon, for clean and dirty xenon.

a)

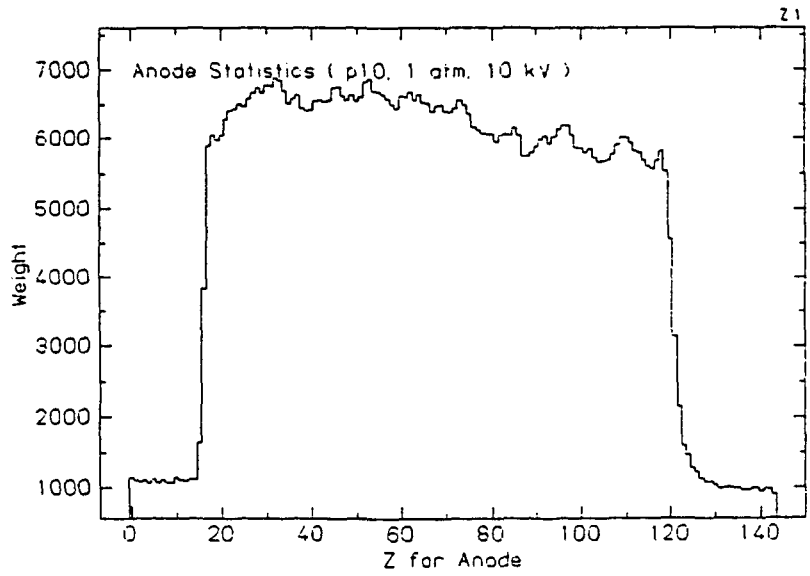

b)

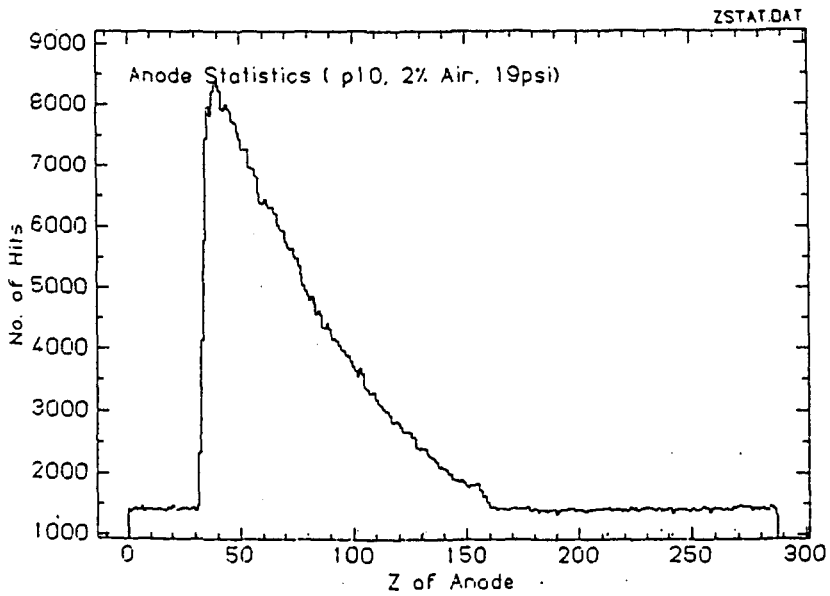

Figure 6.13 Histograms for the anode statistics : (a) for p10 at 1 atm fresh from cylinder, and (b) for p10 mixed with 2% of air.

a)

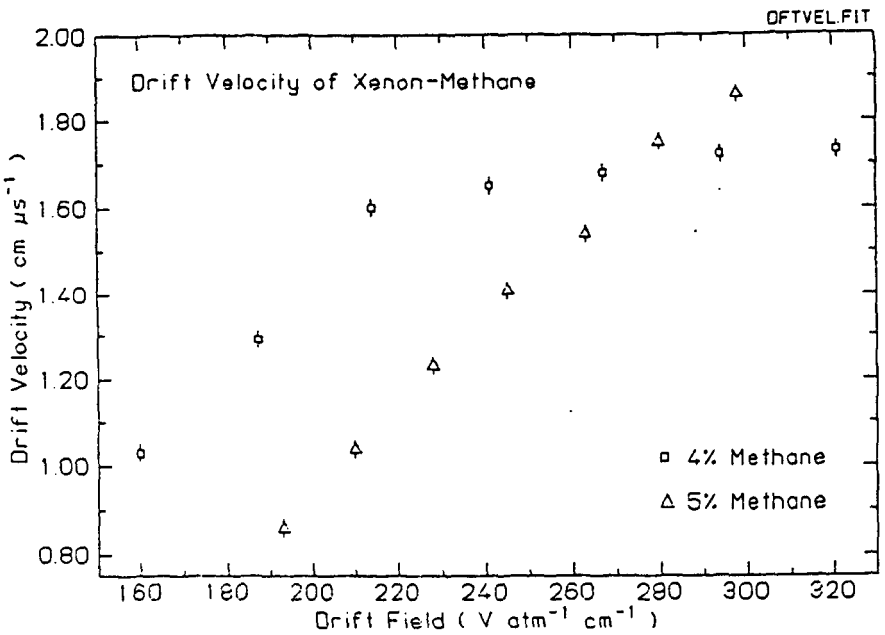

b)

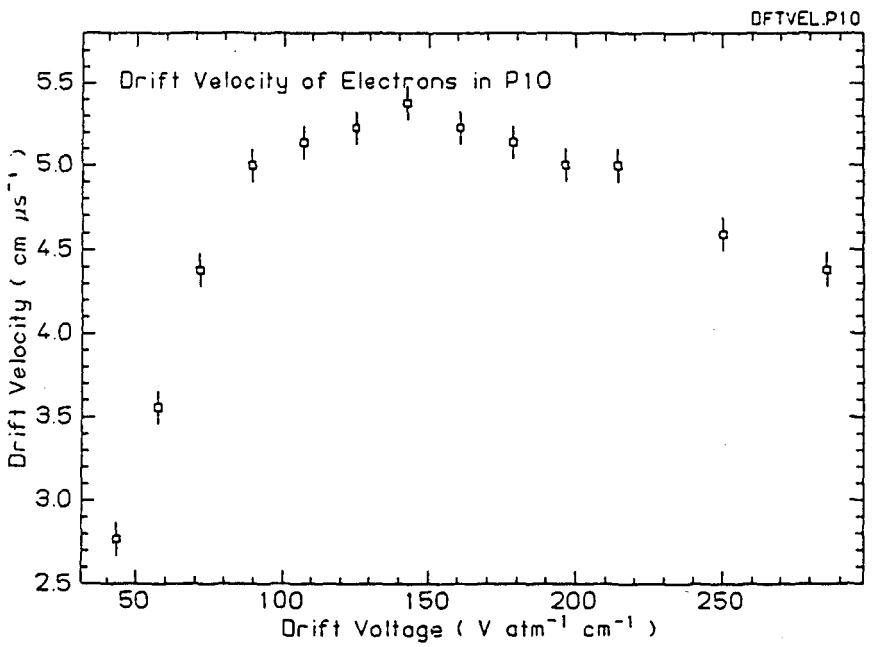

Figure 6.14 Variations of drift velocity with drift voltage : (a) shows xenon with 4% and 5% methane; (b) is for p10.

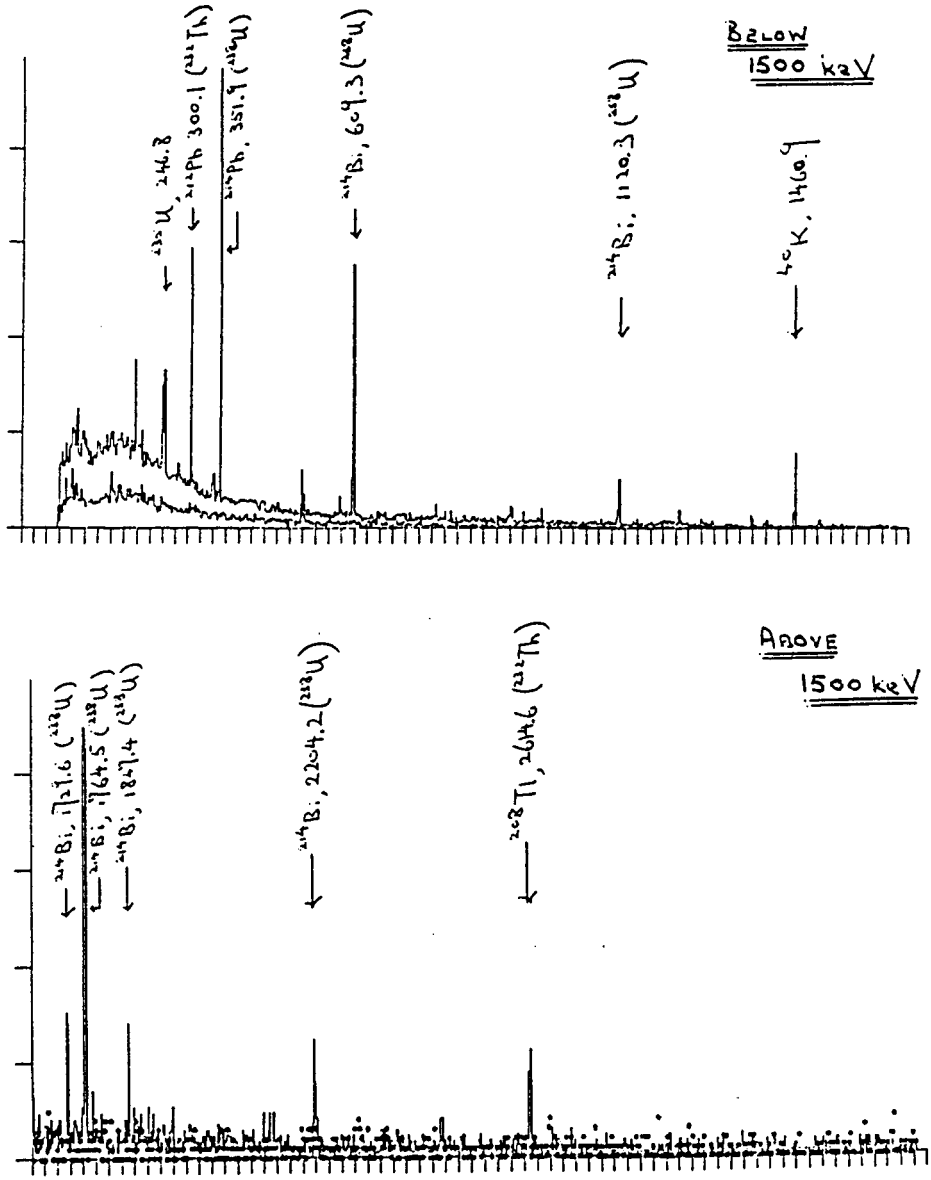

Figure 6.15 Spectrum of a sample of glass with a low background germanium detector, compared to background.

CHAPTER 7

EARLY BACKGROUND MEASUREMENTS

After the TPC with its lead shielding has been installed at the Gotthard Underground Laboratory at mid-May, 1990, data were collected with 5 atm of depleted xenon for a period of 620 hours. This data sample was analyzed with emphasis on the high energy portion (> 1.5 MeV) of the background spectrum. The main objective of this work is to study the background level, as well as to optimize the operation parameters and trigger conditions. In this chapter, the background measurements are presented. Event identification is done by inspection, based on the criterion that two electron events must have "charge blobs" at both ends. At a later stage, software programs will be implemented, to assist and complement this task, and to make it more rigorous and quantitative. Nevertheless, the efficiencies are expected to be comparable.

7.1 Energy Calibration

The energy calibration is shown in Fig. 7.1. The vertical scale is in the unit as measured by integrating numerically the anode pulses digitized by the Transient Recorder. The various data points are described below:

1. The "0 keV" point corresponds to the d.c. offset, sampled by a random trigger.

2. The "511 keV" point is determined by the peak of the ^{22}Na spectrum (^{22}Na is a gamma source with two lines at 511 keV and 1280 keV).

3. The "750 keV" point corresponds to the end-point of the beta decay of ^{85}Kr (Q value is 690 keV) present in the xenon. As discussed in detail in Section 7.3.3, the low energy background increases sharply below this energy. This point is consistent with the end-point of a spectrum taken with ^{137}Cs (gamma source of 660 keV energy).

4. The "1400 keV" point is determined by the end-point of the ^{22}Na spectrum.

5. The "2500 keV" point corresponds to the average energy deposited for ten minimum ionizing muon events recorded during the 240 hour run. The length is measured, and the energy is calculated from the known dE/dx values[48] for minimum ionizing muons. The cosmic ray background is discussed in detail in Section 7.2.

There is undoubtedly much room for improvement in this calibration scheme. The problems are closely related to those of the measurement of energy resolution, as discussed in Section 6.1.2. A major step towards the solution will be to resolve a photo-peak in the 1-3 MeV range. With the present scheme, it is estimated that the calibration is accurate up to about 15% (about $\pm$200 keV at the 0ν region, 2.5 MeV).

7.2 Cosmic Ray Background

From a data sample of 240 hours, 51 cosmic ray events are observed, giving a rate of 5 events per day. This is consistent with expectations shown in Fig. 5.1, as well as the MACRO measurement[49] of 15 cosmic events m^{-2} day^{-1} (both underground sites have roughly the same depth of 3000 mwe).

Out of this sample, ten events are "minimum ionizing" muons, like the one shown in Fig. 6.7a. The length of these 10 muons is measured, and the energy deposited is calculated from the dE/dx values given in Table[48] which, in 5 atm of xenon, correspond to 35 keV cm^{-1}. The average of this energy contributes to the "2500 keV" point on the calibration line discussed above. The incident muons have a spread of energy from 1 GeV to 1 TeV[50], and this gives rise to an intrinsic uncertainty of about 30% in the dE/dx values. Nevertheless, this procedure is important to provide a consistency check, and as an on-line monitor for the gain stability.

The time duration of the vertical muon pulses is important as a monitor of the drift velocity of that gas, as discussed in Section 6.3.2. This gives the composition of the gas, and provides a calibration for the z-axis of the trajectories. In this measurement, the drift velocity is about 1.35 cm μsThe attenuation of the pulses with drift distance is a measure of the purity of the gas from electronegative contaminants, as discussed in Section 6.3.3.

7.3 Single and Two Electron Background

7.3.1 The 0ν Range

The single and double electron spectra from depleted xenon are shown in Fig. 7.2a-b, with a data sample from 620 hours run time. The threshold is 1.6 MeV. It can be seen that, in the 2.50±0.25 MeV window, there are 121 single and 8 two electron candidate events. The rejection efficiency for single electrons is thus at least 94%, as expected from Monte Carlo results shown in Fig. 3.3, as well as with the software analysis discussed in Section 6.2.8.

In the singles spectrum, background increases below about 2.6 MeV, as expected from the end-point of natural radioactive decay chains (2614 keV gamma rays from ^{208}Tl).

From the the doubles spectrum at the 0ν energy range, one obtains a background rate of 0.15 counts keV^{-1} kg^{-1} yr^{-1}, expressed in the background unit usually adopted in double beta decay searches. This is a factor of eight improvement from the best number achieved so far in the germanium double beta decay experiments[16] (1.2 keV^{-1} kg^{-1} yr^{-1}). However, the life-time sensitivities will still be comparable in both cases, since germanium detectors have much better energy resolution than the TPC (2.5 keV compared to 100-200 keV).

7.3.2 The 2ν Range

A data sample of 72 hours was analyzed with an energy threshold of 900 keV, and the singles and doubles background spectra are depicted in Fig. 7.3a-b. In both cases, there is a rise in the background below 1.4 keV, which corresponds to the gamma energy of some common long-lived isotopes: ^{56}Co and ^{40}K. There are 41 candidate events above 0.9 MeV, and 16 counts above 1.1 MeV for the two electron background.

7.3.3 Low Energy Background

The total background (singles, doubles, multiple Comptons....) has been measured in a data sample of 19.5 hours with an energy threshold of 300 keV, and the spectrum is shown in Fig. 7.4. No attempt has been made to identify

individual events. The large number of events makes it impractical to scan through them one by one. The tracks are short and the structures unresolved in the energy range near 500 keV, so that rejection efficiency will not be good in any case.

There are 6279 counts in total, giving a background trigger rate of 5.4 per minute, above 320 keV. The background increases rapidly below about 750 keV, corresponding to the end-point of the beta decay from ^{85}Kr (Q value of 690 keV). The trigger rate below this is 0.083 Hz (5 per minute), implying about 2×10^{-18} ^{85}Kr in the depleted xenon. This number is of the same order of magnitude as the estimate for natural xenon, as discussed in Section 5.1.3.

7.4 Projected Sensitivities

Although the background measurements with depleted xenon discussed above cannot lead to lifetime limits for 0ν and 2ν double beta decay in ^{136}Xe, they do give a good basis for estimating the sensitivities of the experiment when the enriched xenon is put in. The two electron background level above 900 keV per day is summarized in Table 7.1.

Background originating from thermal neutron capture in ^{136}Xe with the formation of beta-emitting ^{137}Xe (end-point 4 MeV), as discussed in Section 5.1.2, may give rise to an additional contribution not included in the measurements with depleted xenon. However, it should be noted that the Gotthard germanium experiment shows no signature of neutron capture, and that the Milano xenon experiment[28] gives identical background levels above the ^{85}Kr end-point for both enriched and natural xenon.

Owing to the uncertainty in our calibration, as well as the difficulty in resolving a photo-peak in the MeV range, we take an energy window of 20% ($\pm$ 250 keV) at the 0ν energy 2.5 MeV. There are 8 background two electron events in 620 hours, implying $C = 113$ events in one year. Following the prescription in Section 5.4 and Appendix 5, one gets, at the 90% confidence level,

$$S_u = 1.65 \times \sqrt{C} = 17.5 .$$

With 60% enriched xenon ($N = 4.1 \times 10^{24}$) and one year run time,

$$T_{\frac{1}{2}}^{0\nu} > 1.6 \times 10^{23} \text{ years.}$$

At the target resolution of 5%, one can restrict the energy window by a factor of 4, then C equals 28.3 in one year, so that

$$T_{\frac{1}{2}}^{0\nu} > 3.2 \times 10^{23} \text{ years.}$$

Adopting the nuclear matrix elements from Vogel[13], this limit implies

$$\langle m_\nu \rangle < 4.5 \text{ eV} .$$

This sensitivity is an order of magnitude improvement from the limit achieved by the Milano xenon experiment[28]. It is not as good as the "no internal background" estimates given in Sections 5.3 and 5.4, because of various known internal sources such as the ^{238}U and ^{232} Th series in the resistors, ^{56}Co from cosmic induced activities in the copper vessel, and the beta decay of ^{214}Bi.

For the 2ν range, there are 16 background events above 1.1 MeV in three days, or 1947 events per year. Folding in an efficiency factor of $\sim$ 50% and a factor of 30% due to the energy threshold, one gets the fiducial number of ^{136}Xe to be 2.4×10^{24}. The life-time limit can then be estimated to be

$$T_{\frac{1}{2}}^{2\nu} > \frac{\text{Fiducial No. of Atoms}}{\text{Background Events per Year}} = 1.2 \times 10^{21} \text{ years.}$$

This sensitivity is again one order of magnitude better than the limits achieved by the Baksan[27] and Milano groups, and is in the range of theoretical predictions (Table 1.1).

It is expected that both sensitivities should improve with time, when we understand the background better, when the radon shield is installed, and when the cosmic induced activities (like ^{56}Co in copper) diminish further. In addition, when comparison experiments with depleted xenon and at a lower pressure (in which case tracks are longer and background rejection efficiency higher) are conducted, these sensitivities can still be further improved.

With these improvements in mind, we hope to achieve sensitivities of 10^{24} years for the 0ν mode and 10^{22} years for the 2ν mode, with two to three years of data taking.

Energy Window (keV)	No. of Counts per Day
0.9-1.25	9.33±1.76
1.25-1.75	2.67±0.94
1.75-2.25	0.54±0.14
2.25-2.75*	0.31±0.11
2.75-3.25	0.17±0.08
3.25-3.75	0.11±0.06
3.75-4.25	0.22±0.09

Table 7.1 Measured two electron background rates per day. The entry marked $*$ is the 0ν energy window.

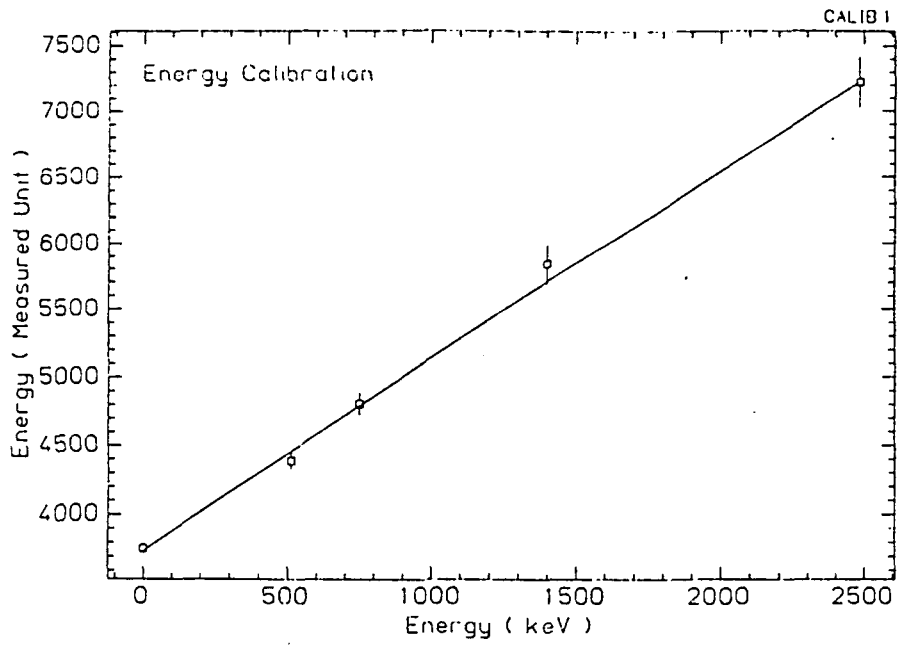

Figure 7.1 The energy calibration line. The data points are discussed in Section 7.1.

a)

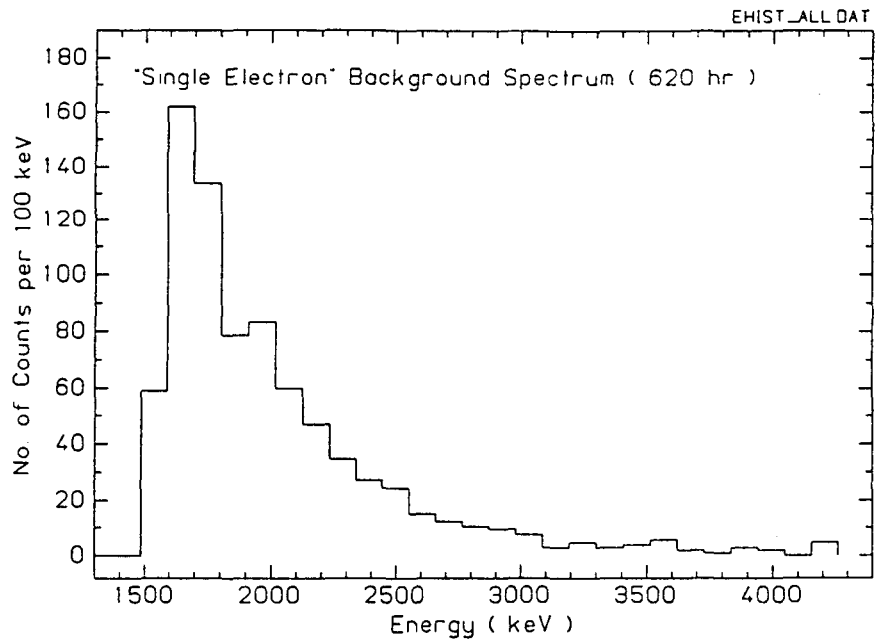

b)

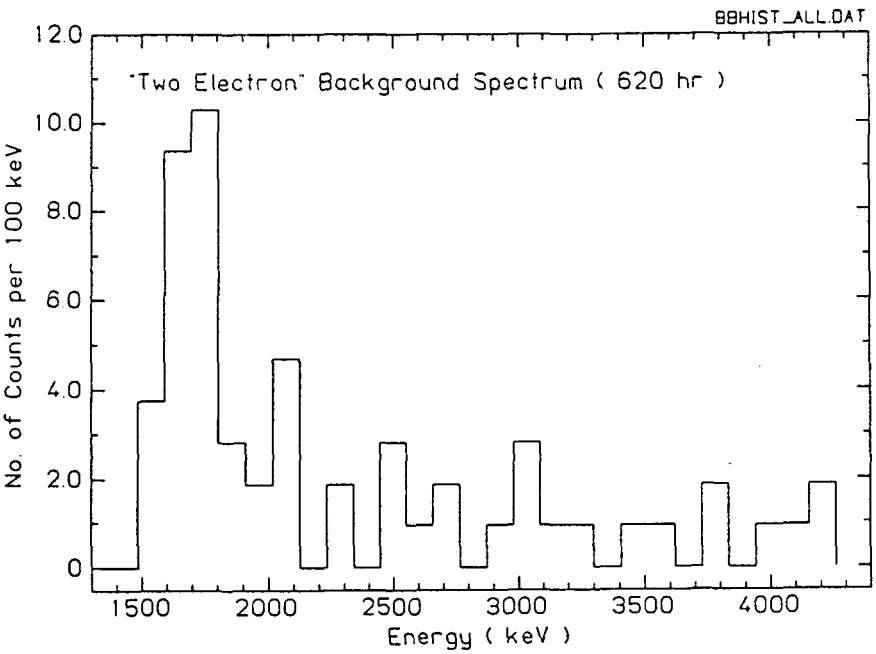

Figure 7.2 Background spectra for (a) single and (b) two electron. Threshold is 1.6 MeV and run time is 620 hours.

a)

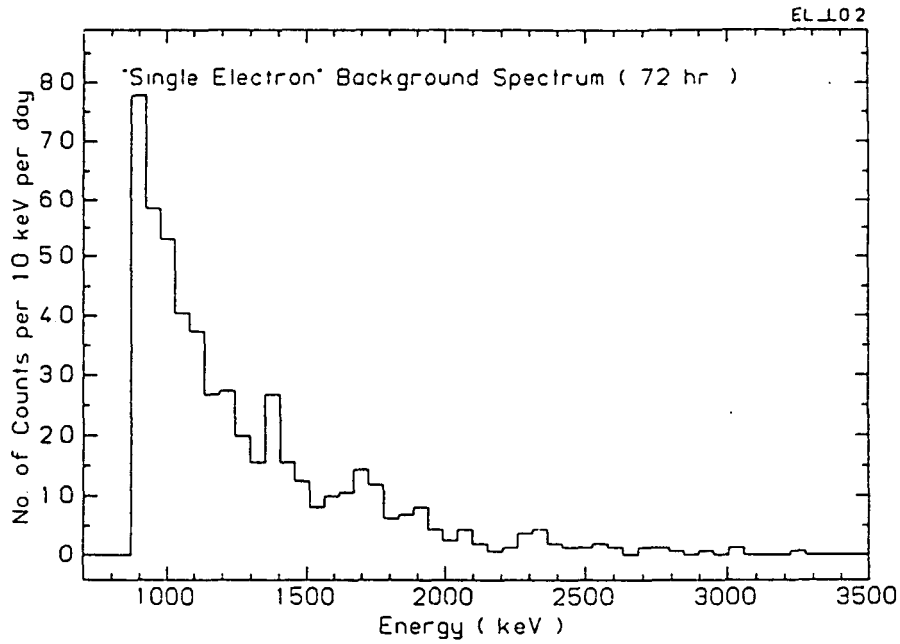

b)

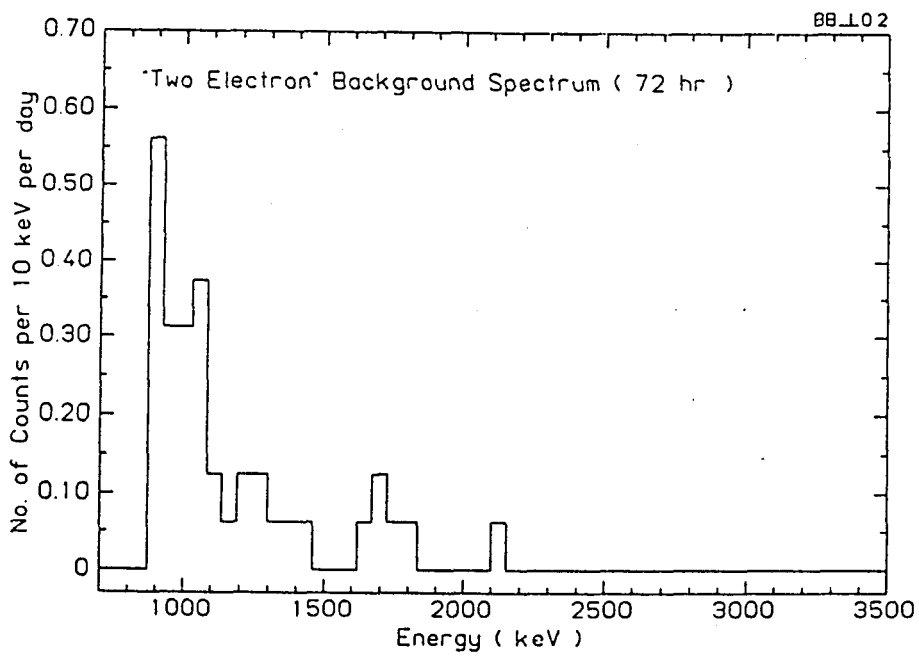

Figure 7.3 Background spectra for (a) single and (b) two electron. Threshold is 900 keV and run time is 72 hours.

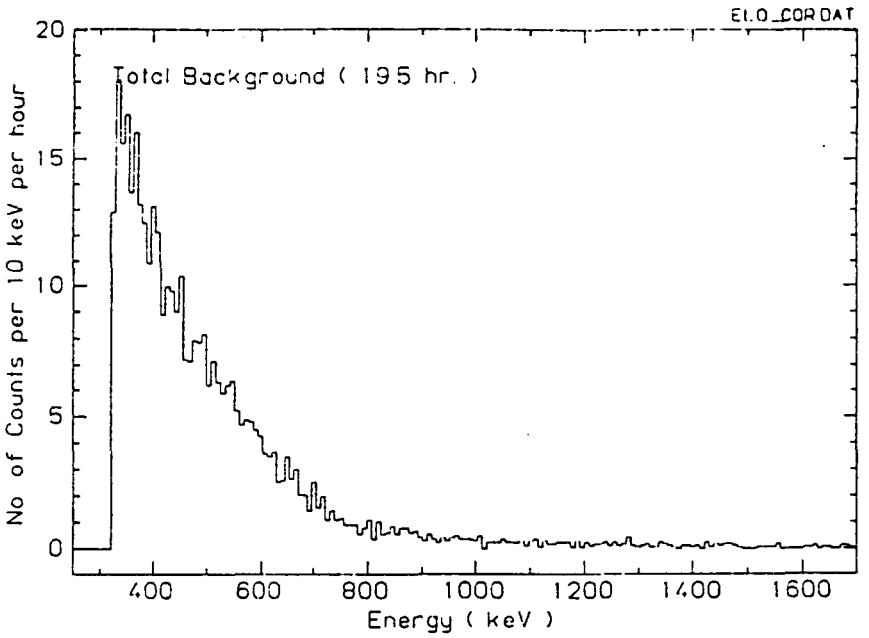

Figure 7.4 Total background spectra. Threshold is 300 keV and run time is 19.5 hours.

CHAPTER 8

EPILOGUE

What we call the beginning is often the end .....

The end is where we start from.

T.S. Eliot

8.1 Present Status

At the time of completion of this thesis (July 90), data taking has ended with 5 atm of depleted xenon, and preparations are under way for the filling and purification of the enriched xenon.

As described in detail in this thesis, we have accomplished building a low background, high pressure xenon Time Projection Chamber capable of running with minimal maintenance in an underground laboratory. Utilizing the tracking capabilities of the TPC, we have demonstrated the powerful background rejection technique of distinguishing the beginning from the end of an electron trajectory based on its difference in charge deposition per unit path length. During the course of construction, a lot of information has been learned on the radio-purity level of typical components used in detector systems.

The early background data indicate a factor of eight improvement over the germanium experiments at the 0ν energy range. With enriched xenon, we expect to reach a lifetime sensitivity of 10^{22} years in 20 days - a limit achieved by the Milano xenon experiment after 260 days run time. With a year of data taking, our experiment should reach the sensitivity level of 10^{23} years with a

comfortable margin. Based on the background data, the projected sensitivities with one year of data taking for the two modes of double beta decay in ^{136}Xe are:

$$T^{0\nu}_{\frac{1}{2}}(\text{at } 5\% \text{ energy window}) \sim 3 \times 10^{23} \text{ years}, \text{ and}$$

$$T^{2\nu}_{\frac{1}{2}} \sim 10^{21} \text{ years}.$$

This is the only double beta decay experiment, besides those on ^{76}Ge, which can achieve a sensitivity of 10^{23} to 10^{24} years for the 0ν lifetime. Other experiments have been limited by source size (like ^{82}Se and ^{100}Mo), or background (like other ^{136}Xe detectors), or both. Considering that ^{76}Ge has less favourable nuclear matrix element predictions than ^{136}Xe, our experiment should be able to set in setting more stringent limits on the Majorana neutrino mass parameter. The expected 2ν sensitivity is also within the range of the predictions, and therefore this experiment may also be able to measure the half-life of this mode.

8.2 Future Tasks and Direction

Future improvements will be pursued along several lines:

1. *Energy Resolution:* An energy resolution of 10% at 500 keV has been achieved, and it is expected that the percentage resolution at higher energy should at least be the same if not better. However, this assertion has to be demonstrated convincingly. It may not be a straightforward task to extract a photopeak at the MeV range from a general background of multiple Compton scattering. Monte Carlo simulations will be made to study this point. Software analysis (for instance, selecting only those single track events) will be pursued. Detailed studies will be made to in-

vestigate how the signals should be sampled by the Transient Recorder. The data acquisition system will be modified by adding an ADC to sample the integrated anode signals, in parallel with recording the current signals. Once photopeaks are sorted out from the background, the energy calibration can be done more accurately as well.

2. *Event Identification:* More analysis programs will be implemented to make the task of background rejection more organized, rigorous and quantitative, and to extend it to lower energy. The possibility of identifying pair production events as those with sharp vertices near the central portion of the track will be investigated.

3. *Background:* Radioactivity level due to the cosmic ray induced ^{56}Co in copper will decrease with time. The ^{85}Kr concentration is expected to be substantially reduced in the enriched xenon. A radon shield will be installed shortly to prevent radon gas from diffusing into the lead shieldings. The search for radio-clean resistors is under way.

The first phase of data taking will last for one year with 5 atm of enriched xenon. Meanwhile, the tasks mentioned above will be pursued. The next phase depends on the results of the first one. There are several possible options:

1. Repeat the measurement with 5 atm of depleted xenon as a control experiment, to increase sensitivity mainly on the 2ν mode. Differences in the thermal neutron cross section between the various xenon isotopes, as well the possible changes in radioactivity level of the various background sources with time, must be carefully studied.

2. Repeat the measurement with enriched xenon at a lower pressure. This will improve the single electron rejection efficiency at the 2ν range be-

cause the trajectories are now longer. The 2ν mode is background limited rather than statistics limited, so that one can afford to have a smaller numbers of candidate isotopes and worse enclosure efficiency.

3. Repeat the measurement with enriched xenon at a higher pressure, to enhance the sensitivity for the 0ν mode. Both the fiducial number of candidate isotopes as well as the enclosure efficiency will increase. However, rejection for single electron events may not be as good.

With all these improvements implemented and more information on background extracted from various control experiments, we expect to achieve ultimately the target lifetime sensitivities of 10^{24} years for the 0ν mode and 10^{22} years for the 2ν mode.

8.3 Implications

This experiment is unique in its approach. What we have learned and demonstrated may contribute to other areas of research, as outlined briefly below.

1. *TPC Development:* There are several characteristic features for this TPC that are different from the more conventional ones. The fill gas is xenon-methane at high pressure. All the anode wires are connected together electrically, and the total charge depositions are measured by integrating the anode signals. An ingenious XY pad design enables readout of both coordinates from the same circuit board, thus ensuring uniform responses in both projections. Excellent tracking capabilities have been demonstrated for low energy (MeV range), completely stopped electrons.

Based mainly on this work, there is a proposal[51] to measure low energy (hundreds of keV) $\bar{\nu}_e$-e scattering of reactor neutrinos with a very similar TPC. Some background rejection can be achieved by relating the scattering angle (angle subtended between the beginning of the track with the line of sight from the reactor core) of an electron event with its energy. The physics motivation is to measure the neutrino magnetic moment that has been proposed as an explanation for the Solar Neutrino Puzzle and for the possible anticorrelation between the solar neutrino flux and sunspot activities[52].

2. *Xenon Gas Handling:* Gaseous and liquid xenon are being utilized more and more frequently as detector media in particle physics, astrophysics and even medical physics, because of its higher Z (compared to the other common detector materials) and hence enhanced photon absorption cross section. This work has demonstrated the feasibility of using xenon in a large detector, with continuous purification and minimal maintenance. The two-stage recovery technique developed in this experiment is applicable to other systems in which a large quantity of xenon is used.

3. *Track/Blob Distinction:* We have demonstrated the powerful technique of measuring the directionality of low energy electrons by tracing the changes in the dE/dx values and, to some extent, from the general profile of the trajectory. This is particularly relevant to the other double beta decay experiments in which the distinction between single electron and two electron events is a great asset. Based on this work, ideas are considered to deploy this "track/blob" differentiation in scintillating fibres[53] (for isotopes like ^{150}Nd) and cryogenic detectors[54] (for isotopes like ^{100}Mo).

4. *Low Background Components:* Extensive efforts have been made to test and look for detector components (like solder, cables, circuit board, epoxy, getter materials ...) with low radioactivity levels. This information is particularly crucial to all other low count rate experiments with energy ranges of interest below 2.6 MeV, the end-point for natural radioactivity.

As a concluding remark, T.S. Eliot's confusion has been addressed experimentally - we can differentiate unambiguously the *"beginning"* from the *"end"* (see Figures 6.7a and 6.7b). Nevertheless, Eliot was correct in his physical insights[55]. The characteristic features at the *"end"* are indeed the starting basis for this (and possibly some other) experiment. Certainly, the *"end"* of this thesis marks the starting point of some even more exciting ventures in physics.

APPENDIX 1

QUASIPARTICLE RAMDOM PHASE APPROXIMATION OF DOUBLE BETA DECAY MATRIX ELEMENTS

In Ref. 13, Engel, Vogel and Zirnbauer use the quasiparticle random phase approximation (QRPA) to evaluate the double beta decay matrix elements $M^{2\nu}_{GT}$, $M^{0\nu}_{GT}$ and $M^{0\nu}_{F}$ given in Section 1.2.2. Since the neutrino propagator $H(\bar{E}, r)$ favors small internucleon separations, the effect of short range nucleon-nucleon correlations created by the nuclear hard core is included so that the expression $K_{k,l}$ can be approximated by

$$K_{k,l} = \rho(r_{k,l}) \frac{e^{-1.5\bar{E}r_{k,l}}}{r_{k,l}} \rho(r_{k,l}), \text{ where}$$

$$r_{k,l} = |\vec{r}_k - \vec{r}_l|, \text{ and}$$

$$\rho = 1 - e^{-\gamma_1 r^2}(1 - \gamma_2 r^2),$$

with the parameters chosen to be $\gamma_1 = 1.1\,\mathrm{fm}^{-2}$, $\gamma_2 = 0.68\,\mathrm{fm}^{-2}$.

A1.1 Formulation

Assuming harmonic nuclear motions, the excited states of the intermediate odd-odd nuclei can be described by the solutions of the QRPA eigenvalue equations

$$\begin{pmatrix} A & B \\ -A & -B \end{pmatrix} \begin{pmatrix} X \\ Y \end{pmatrix} = \omega \begin{pmatrix} X \\ Y \end{pmatrix},$$

where the matrices A and B are given by

$$A^J_{pn,p'n'} = (\epsilon_p + \epsilon_n)\delta_{pn,p'n'} + \tilde{V}^J_{pn,p'n'}(u_p v_n u_{p'} v_{n'} + v_p u_n v_{p'} u_{n'})$$

$$+V^J_{pn,p'n'}(u_p u_n u_{p'} u_{n'} + v_p v_n v_{p'} v_{n'}), \text{ and}$$

$$B^J_{pn,p'n'} = (-)^J[\tilde{V}^J_{pn,p'n'}(v_p u_n u_{p'} v_{n'} + u_p v_n v_{p'} u_{n'})$$

$$-V^J_{pn,p'n'}(u_p u_n v_{p'} v_{n'} + v_p v_n u_{p'} u_{n'})].$$

Here ϵ are the quasiparticle energies obtained by solving the BCS equations for the nuclear Hamiltonian $\hat{H}$. $X = X^J_{pn}(m)$ and $Y = Y^J_{pn}(m)$ are the forward and backward QRPA amplitudes, and $\omega = \omega^J(m)$ are the QRPA frequencies, m being used to distinguish various solutions of the QRPA equations. The vacant and occupied pairing amplitudes are given by u and v respectively, such that $u_j^2 + v_j^2 = 1$ for any orbital j, and p/n denotes proton/neutron particle orbits.

V^J and $\tilde{V}^J$ are the particle-particle and particle-hole interaction matrix elements respectively. In Ref. 13, they are both parametrized by the respective matrix elements of a δ-function interaction, such that

$$V^J_{pn,p'n'} = \frac{1}{2}(\alpha_0' V^{J;0,1}_{pn,p'n'} + \alpha_1' V^{J;1,0}_{pn,p'n'}), \text{ and}$$

$$\tilde{V}^J_{pn,p'n'} = \frac{1}{2}(\alpha_0 \tilde{V}^{J;0,1}_{pn,p'n'} + \alpha_1 \tilde{V}^{J;1,0}_{pn,p'n'}),$$

where the matrix elements $V^{J;S,T}$'s are given in the Appendix of Ref. 13, and the coefficients α 's are adjustable parameters determined from experiments. Two of them are in the particle-particle channel: $\alpha_0' = g_{pp}^{S=0,T=1}$ and $\alpha_1' = g_{pp}^{S=1,T=0}$, and two in the particle-hole channel: $\alpha_0 = g_{ph}^{S=0,T=1}$ and $\alpha_1 = g_{ph}^{S=1,T=0}$. Other authors[13] (Klapdor, Faessler) have used different nuclear potentials and obtained qualitatively similar results.

For any one-body operator T^{JM} that transforms a neutron to a proton, the matrix element connecting the ground state $|0\rangle$ of the even-even nucleus (N, Z)

to the one-phonon excited state $|m;JM\rangle$ of the adjacent odd-odd nucleus $(N-1,Z+1)$, within QRPA, is given by

$$\langle m;JM|T^{JM}|0\rangle_{QRPA} = \sum_{pn}[t^{-,J}_{pn}X^J_{pn}(m) + t^{+,J}_{pn}Y^J_{pn}(m)]\,, \text{ where}$$

$$t^{-,J}_{pn} = \frac{u_p v_n}{\sqrt{2J+1}}\langle p \parallel T^J \parallel n\rangle\,, \text{ and}$$

$$t^{+,J}_{pn} = (-)^J\frac{v_p u_n}{\sqrt{2J+1}}\langle p \parallel T^J \parallel n\rangle\,,$$

$\langle p \parallel T^J \parallel n\rangle$ being the reduced matrix element. Similarly, the transition matrix element from (N,Z) to $(N+1,Z-1)$, induced by $T^{JM\dagger}$, is given by

$$\langle m;J-M|T^{JM\dagger}|0\rangle_{QRPA} = (-)^M\sum_{pn}[t^{-,J}_{pn}Y^J_{pn}(m) + t^{+,J}_{pn}X^J_{pn}(m)]\,.$$

A further approximation is made by replacing the charge-lowering transition amplitudes for the final nucleus with those of the initial nucleus, or the charge-raising transition amplitudes for the initial nucleus with those of the final ones. Then a generic matrix element can be written in the form

$$M \equiv \sum_{pn,p'n';Jm} Z^{Jm}_{pn,p'n'}[u_p v_n Y^J_{pn}(m) + v_p u_n(-)^J X^J_{pn}(m)]$$

$$\times\,[u_{p'}v_{n'}X^J_{p'n'}(m) + v_{p'}u_{n'}(-)^J Y^J_{p'n'}(m)]\,,$$

where the different decay modes are described by different forms of the coefficient Z, such that

$$Z^{Jm}_{pn,p'n'}(M^{2\nu}_{GT}) = \delta_{J,1}\frac{\langle p \parallel \sigma\tau^+ \parallel n\rangle\langle p' \parallel \sigma\tau^+ \parallel n'\rangle}{\omega(m) - \frac{1}{2}(M_i + M_f)}\,,$$

$$Z^{Jm}_{pn,p'n'}(M^{0\nu}_F) = (2J+1)\sum_{J'}\sqrt{2J'+1}(-)^{j_p+j_{n'}+J'}W(j_p j_n j_{p'} j_{n'};JJ')$$

$$\times\langle j_{p_1}j_{p'_2};J' \parallel RK_{1,2}\tau^+_1\tau^+_2 \parallel j_{n_1}j_{n'_2};J'\rangle\,, \text{ and}$$

$$Z^{Jm}_{pn,p'n'}(M^{0\nu}_{GT}) = (2J+1)\sum_{J'}\sqrt{2J'+1}(-)^{j_p+j_{n'}+J'}W(j_p j_n j_{p'} j_{n'};JJ')$$

$$\times \langle j_{p_1} j_{p_2'}; J' \parallel RK_{1,2} \vec{\sigma}_1 \cdot \vec{\sigma}_2 \tau_1^+ \tau_2^+ \parallel j_{n_1} j_{n_2'}; J' \rangle ,$$

with W being the standard Racah's W-functions. Summation over parities is implicit in the 0ν matrix elements.

A1.2 Evaluation of M

The reduced matrix elements given in the previous section are calculated by approximating the single-particle wavefunctions to those of the harmonic oscillator eigenstates. The quasiparticle energies ϵ and the pairing amplitudes u and v are determined by solving the BCS equations[56]. The single-particle energy levels are obtained from standard schemes like the Coulomb-corrected Woods-Saxon potential. The residual pairing interaction g_{pair} is chosen to be about -260 to -290 MeVfm^3. The pairing energies are determined from the experimental binding energy differences of the odd- and even-A nuclei.

The evaluation of X, Y and ω requires knowledge of V and $\tilde{V}$, which in turn depend on the four adjustable parameters. The particle-hole parameters α_0 and α_1 are determined by fitting to the measured energies of the isobaric analog and Gamow-Teller giant resonances over a wide range of nuclei. The best values are $\alpha_0 = -890$ MeVfm^3 and $\alpha_1 = -1010$ MeVfm^3. The particle-particle parameter α_1' is fixed by the measured β^+ strengths in five neutron-deficient nuclei(^{94}Ru, ^{96}Pd, ^{148}Dy, ^{150}Er and ^{152}Yb). The value is restricted to a window between -390 and -432 MeVfm^3. Furthermore, the relation $\alpha_0' = 0.6\alpha_1'$ is chosen, based on data from low-energy two-nucleon scattering that suggests the spin-singlet force is about 60% of the spin-triplet one.

A1.3 Results

Calculations show that inclusion of the particle-particle interactions in QRPA lead to an increase in ground-state correlations, and as a result, to a suppression of β^+ strength. This explains naturally why the experimental β^+ ft values for neutron-deficient nuclei with a magic number of neutrons are approximately 7 times smaller than those predicted by single-particle calculations. This decrease in β^+ strengths also suppresses the $2\nu\beta\beta$ rate. Fig. A1.1 shows the dependence of $M_{GT}^{2\nu}$ in ^{76}Ge on α_1'. Since $M_{GT}^{2\nu}$ passes through zero, the decay rates may become sensitive to other nuclear phenomena in that range of α_1'.

Figures A1.2a and A1.2b show the contributions of individual multipoles to $M_{GT}^{0\nu}$ and $M_F^{0\nu}$ in ^{76}Ge. There is also a suppression of $M_{GT}^{0\nu}$ caused by the cancellation of the contribution from 1^+ state by those from all others. Predictions of $\beta\beta$ lifetimes in various nucleus are given in Table 1.1. The suppression of $0\nu\beta\beta$ decay rates implies that neutrino mass deduced from experimental lifetime limits are less stringent than those suggested by other authors.

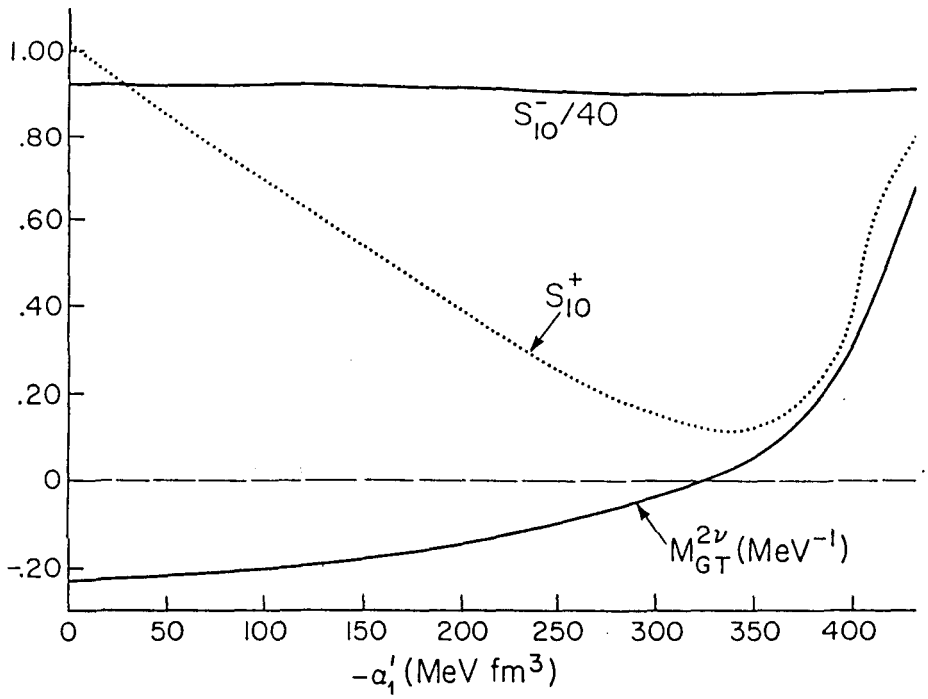

Figure A1.1 The β^+ strength, β^- strength (scaled by 1/40), and $M_{GT}^{2\nu}$ for the decay $^{76}Ge \rightarrow ^{76}Se$ as a function of α_1'.

a)

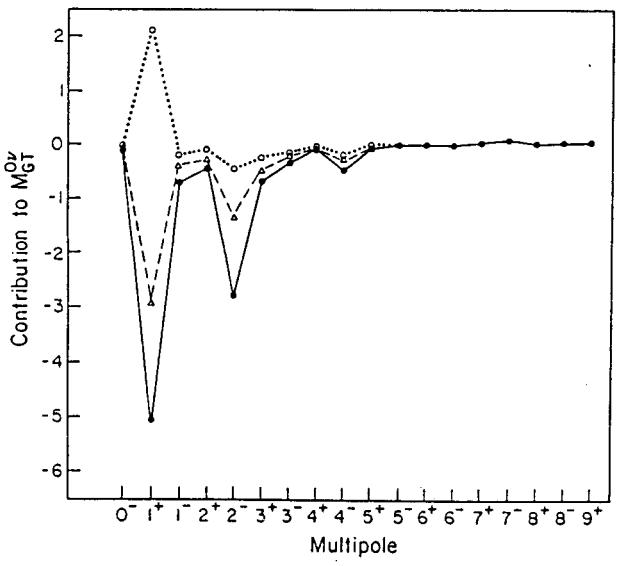

b)

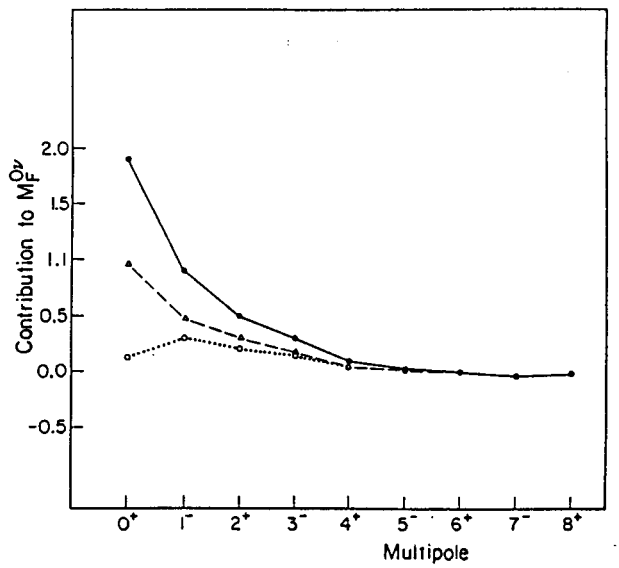

Figure A1.2 Contributions of individual multipoles to (a) $M_{GT}^{0\nu}$ and (b) $M_{F}^{0\nu}$ for the nucleus ^{76}Ge. The dark circles are the independent quasiparticle results, the triangles are those including particle-hole interaction, and the open circles are results with additional particle-particle interaction.

APPENDIX 2

MONTE CARLO STUDIES OF DELTA ELECTRONS AND BREMSSTRAHLUNG EFFECTS IN THE TPC

A2.1 Delta (or "Knock-On") Electrons

The spirit of the experiment is the rejection of single electron events, based on the observation that the dE/dx values at the ends of electron trajectories are much higher than those at the origins. However, the dE/dx(ionization) calculated from the Bethe-Bloch formula only gives the average energy loss of a charge particle per unit length, and does not take into account the fluctuations of this value. The manifestation of these fluctuations is the emission of energetic (relative to minimum ionizing) secondary electrons, commonly called delta electrons. Fig. 6.6a. shows a cosmic ray muon measured by the TPC. The fluctuations of dE/dx along the track are prominent. One must therefore incorporate these into the Monte Carlo stimulations to study their effects on background rejection.

The number of secondary electrons of energy ϵ emitted per unit distance, created by an incident electron of kinetic energy T, in a medium with electron density N_e, is given by[48]

$$N_\delta(\epsilon, T) = \frac{W(T)}{\epsilon^2}, \text{ where}$$

$$W(T) = \frac{2\pi r_e^2 m_e N_e}{\beta^2}, \text{ taking } \hbar = c = 1\,.$$

This formula is valid within the range $I \ll \epsilon \ll T$, where the parameter I characterizes the binding of the electrons of the medium. Typically, $I \sim 16 Z_{med}^{0.9}\,\mathrm{eV} \sim 580\,\mathrm{eV}$ for xenon.

The prescriptions for the simulations are as follows:

1. Fix the parameter $\epsilon_0(T)$ by

$$\frac{dE}{dx}(T) = \int_{\epsilon_0}^{T} \epsilon N_\delta(\epsilon, T) d\epsilon$$

where $\frac{dE}{dx}(T)$ is calculated from the Bethe-Bloch formula or obtained from Table[33].

2. Generate energy loss $\Delta E(T)$ in a given distance Δx, by splitting the above expression into two terms:

$$\frac{\Delta E}{\Delta x} = \int_{\epsilon_0}^{\epsilon_{cut}} \epsilon N_\delta(\epsilon, T) d\epsilon + \sum_{i=1}^{N_{MC}} \epsilon_{MC_i}$$

where the parameter $\epsilon_{cut}(T)$ is fixed through

$$N_{MC} = \int_{\epsilon_{cut}}^{T} W(\epsilon, T) d\epsilon\,,$$

and N_{MC} is an input parameter chosen such that $I \ll \epsilon_{cut} \ll T$. The values of ϵ_{MC_i} are generated by Monte Carlo according to a $\frac{1}{\epsilon^2}$ distribution in the range $\epsilon \in [\epsilon_{cut}, T]$.

3. The energy loss in distance Δx is then ΔE, and the electron energy becomes $(T - \Delta E)$. If $\Delta E > \frac{1}{2}T$, then the energy loss is $(T - \Delta E)$ while the electron has energy ΔE. The program returns to step #1 and reiterates until the incident electron loses all its energy.

With this effect incorporated, there are 4 or 5 delta electrons (> 30 keV) ejected for a typical 2.5 MeV electron trajectory at 5 atm of xenon. In particular, about 6% of these events would have a delta electron ejected at the first cm of the tracks (total length about 68 cm).

To study the difference between the beginning and the end of an electron track, the following analysis is done. The two ends of a trajectory are located,

and the charge depositions in a $(17.5)^3$ cm^3 volume centered at the ends are calculated and displayed in histograms. The results are shown in Figs. 3.3a and 3.3b. For a single electron track, the spectrum for the origin is very different from that of the end. This can serve as a basis for background rejection, with an efficiency of about 97%. With a two-level readout system, the volume being sampled is divided into a $5 \times 5 \times 5$ box. With a threshold level of 30 keV, and weights for *track* and *blob* being 1 and 2, respectively, one can still get a rejection efficiency of about 94%.

A2.2 Bremsstrahlung Effects

The bremsstrahlung yield (ratio of energy loss by radiation to the incident energy) of a 2.5 MeV electron is about 8%, or 200 keV, large enough to change the energy spectra at a resolution of 5%. One, therefore, has to study how much of the photons created by bremsstrahlung would escape the volume of the TPC. This process will contribute to some inefficiency factor.

The procedure for the simulation is as follows:

1. The formula for the bremsstrahlung differential cross section $\frac{d\sigma}{dk}$[34], where k is the photon energy, is far too complicated for practical simulations. However, by fitting the numerical values of $\frac{d\sigma}{dk}$ given in Table[34], it can be seen that the differential cross section can be approximated to a $(\frac{1}{x} - 1)$ distribution, in the energy range of interest (500 keV to 3 MeV), where $x = \frac{k}{T}$, T being the energy of the incident electron. The fit of the spectrum at 2 MeV is shown in Fig. A2.1.

2. Take

$$\frac{d\sigma}{dk} = A(T)(\frac{1}{x} - 1),$$

where the normalization $A(T)$ is fixed by

$$(\frac{dE}{dx})_{rad} = N_{Xe}\int_0^T k\frac{d\sigma}{dk}dk,$$

N_{Xe} being the number density of xenon atoms, and $(\frac{dE}{dx})_{rad}$ is obtained from Table[33].

3. Choose a low energy cut-off of $k_0 = 10$ eV, and calculate the total cross section

$$\sigma(k > k_0) = \int_{k_0}^T \frac{d\sigma}{dk}dk,$$

and the mean free path

$$\lambda = \frac{1}{N_{Xe}\sigma}$$

The probability of having a bremsstrahlung interaction while the electron traverses a distance of Δx, is then

$$P = 1 - exp(-\frac{\Delta x}{\lambda}).$$

4. Generate a random number u in [0,1]. If u<p, generate $E_\gamma \in [k_0, T]$, according to a $(\frac{1}{x} - 1)$ distribution. Then $\Delta E_{total} = \Delta E_{ion} + \Delta E_\gamma$, and the electron energy becomes $T - \Delta E_{total}$. The probability of the photon escaping the TPC is then

$$p' = exp(-\frac{l}{\lambda_\gamma}),$$

where l is taken to be 35 cm (half TPC linear dimension), and λ_γ is the photon absorption mean free path deduced from Table[46]. Generate another random number v in [0,1] so that if $v < p'$, the photon will escape the chamber.

5. Return to #2 and follow the electron until it stops, using Bethe-Bloch formula for ΔE_{ion}. The total energy measured by the TPC $[T_0 - \Sigma E_\gamma(escaped)]$ is calculated.

The average energy escaped per event due to bremsstrahlung is given in Fig. A2.2. With 5 atm of xenon, $\Sigma E_\gamma(escaped) \sim 147$ keV for electrons at 2.5 MeV, and ~ 85 keV for double beta events of the same energy. The percentage of events completely captured is shown in Fig. 3.2b. This capture efficiency for electrons is 68% while that for double beta events is 76%, both also at 2.5 MeV. Including the efficiencies for completely enclosing the trajectories (22% for electrons and 33% for double beta), one can conclude that the overall efficiencies for the TPC for events at 2.5 MeV at 5 atm of xenon at STP are

$$\eta(e^-) \sim 15\%, \text{ and}$$

$$\eta(\beta\beta) \sim 25\%.$$

Furthermore, bremsstrahlung also affects the definition of an "event." One has to include those events with random charge depositions (< 100 keV) inside the chamber and disconnected from the main tracks. It is estimated that about 43% of the fully captured events will exhibit this feature. Events that can be interpreted as an electron track and a muon with the emission of bremsstrahlung photons are given in Figs. 6.7b and 6.6b, respectively.

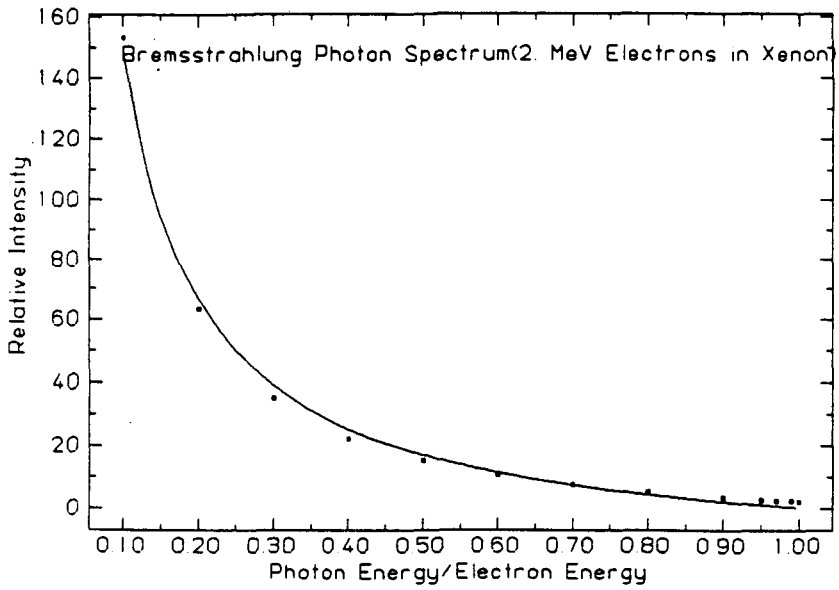

Figure A2.1 The bremsstrahlung differential cross section at an electron energy of 2 MeV in xenon. The boxes are values adopted from Table, while the line is the fit to a $(\frac{1}{x} - 1)$ distribution, where x equals photon energy divided by electron energy.

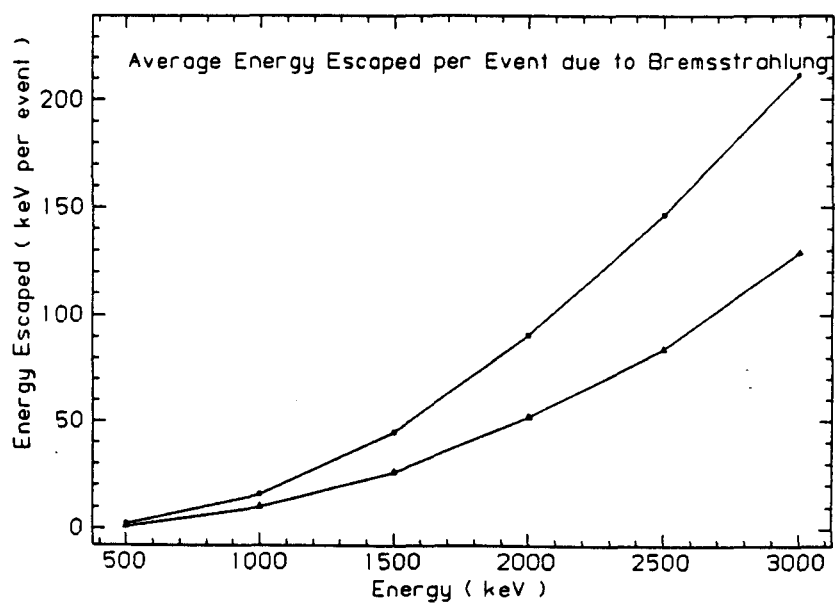

Figure A2.2 Average energy escaped from the TPC in the form of bremsstrahlung photons, as a function of the transition energy. Double beta decays and single electrons are represented by the lower and upper curves, respectively.

APPENDIX 3

ATTACHMENT OF DRIFTING ELECTRONS TO OXYGEN

Electronegative contaminants can attenuate the drifting secondary electrons and thus degrade the signals in drift chambers. Among the contaminants, oxygen (electron affinity 0.43 eV) is the most commonly found in drift gases. It is present in commercial gas supplies and also produced by "*outgassing*" from the chamber materials. The reaction for electron attachment to oxygen is[57]

$$(1) \qquad O_2 + e^- \rightarrow O_2^{-*},$$

followed by two competing processes:

$$(2a) \qquad O_2^{-*} + M \rightarrow O_2 + M + e^-$$

$$(2b) \qquad O_2^{-*} + M \rightarrow O_2^- + M^*$$

where M denotes a buffer gas molecule. The relative probabilities of the two processes, and hence the attenuation length of the drifting electrons λ_e, depends strongly on the nature of the buffer gas. Electrons will be quenched if process (2b) takes place and M^* undergoes transition to the ground state through heat (phonons) dissipation. Complex molecules with dense vibrational energy levels favor process (2b), whereas noble gases are basically inert to electron attachment, and hence, favor process (2a). Water and methanol do not have a sizable attachment to the electrons, but can act as buffer molecules that substantially enhance the cross section for process (2b). The consequence of this two-step mechanism is that given the same contamination level, the attenuation length is inversely proportional to gas pressure squared.

Adopting the simplifying assumption that the mean electron energy is con-

stant, the attenuation length varies as

$$\lambda_e \propto \frac{v_d}{P(\mathrm{M})P(\mathrm{O_2})}$$

where v_d is the drift velocity of the electrons, and $P(\mathrm{M/O_2})$ is the partial pressure of the buffer gas/oxygen. Measurements[58] for that in 1 atm Xe-10%CH_4 give

$$\lambda_e/\mathrm{cm} = \frac{7.8 \times 10^{-3}}{f(\mathrm{O_2})}$$

at v_d =2.3 cmμs^{-1}, where $f(\mathrm{O_2})$ is the fraction of oxygen in the gas. From this, it can be deduced that in order to keep attenuation below a 5% level with 5 atm Xe-5%CH_4, over a drift distance of 70 cm and at $v_d \sim$1 cmμs^{-1}, $f(\mathrm{O_2})$ must be less than 0.2 ppm.

APPENDIX 4

AN EXAMPLE OF TRACK ANALYSIS ALGORITHM

After the hardware construction and installation of the TPC at Gotthard, the main task of the experiment is to analyze the data, and to extract a "Double Beta Decay Candidate Events" energy spectrum out of it. Whereas differentiating a single electron trajectory from a double beta one is relatively easy by the eye, developing a software algorithm general enough for all track geometries, taking into account possible dead or noisy channels, is a complicated, but interesting, problem.

A preliminary program *"boxcheck"* has been written to do the track analysis. It is developed not so much to fully solve the problem, but rather to familiarize ourselves with the subtleties and difficulties involved. The program only handles the trajectory data in 2D projection, and is optimized with respect to computer time consumed, so that it can be used for on-line analysis if necessary.

The flow chart of the algorithm is given in Fig. A4.1. The prescription of the analysis is as follows:

1. Check the number of data bins of the XY channels that are above the second threshold level, and group them into *blobs*. If the number of *blobs* is less than two, then that projection is NOGOOD.

2. A box is drawn around each *blob*. If the number of data bins above the first threshold level occupy more than a certain fraction of the box, then this *blob* is at an end (very staggered tracks), and the program proceeds

on to the next *blob*. Otherwise, the algorithm deduces the number of times the track crosses the boundary of the box (*ncross*), and proceeds to #3.

3. If $ncross \geq 2$, the program will try to move in and out of the box for each crossing. If that cannot be done, that point is not a real crossing and the value of *ncross* is reduced by one.

4. If $ncross < 2$, then that *blob* is situated at an end. Go back to #2 again until all the *blobs* have been checked.

5. The projection is GOOD if it has at least two blobs situated at the ends. The definition of a GOOD event depends on which mode is used - AND mode, requiring both projections to be GOOD; and OR mode, requiring either one of the projections to be GOOD.

The efficiency of the program depends on the fine tunings of the various parameters used as well as the mode adopted. For 2.5 MeV tracks at 5 atm of xenon, the best rejection efficiencies achieved are 80% for single electrons and 19% for double beta events, in AND mode and with a speed of 3.7 events per second. For 1 MeV tracks, the rejection efficiencies are 65% for single electrons and 14% for double betas, in OR mode and with a speed of 11 events per second.

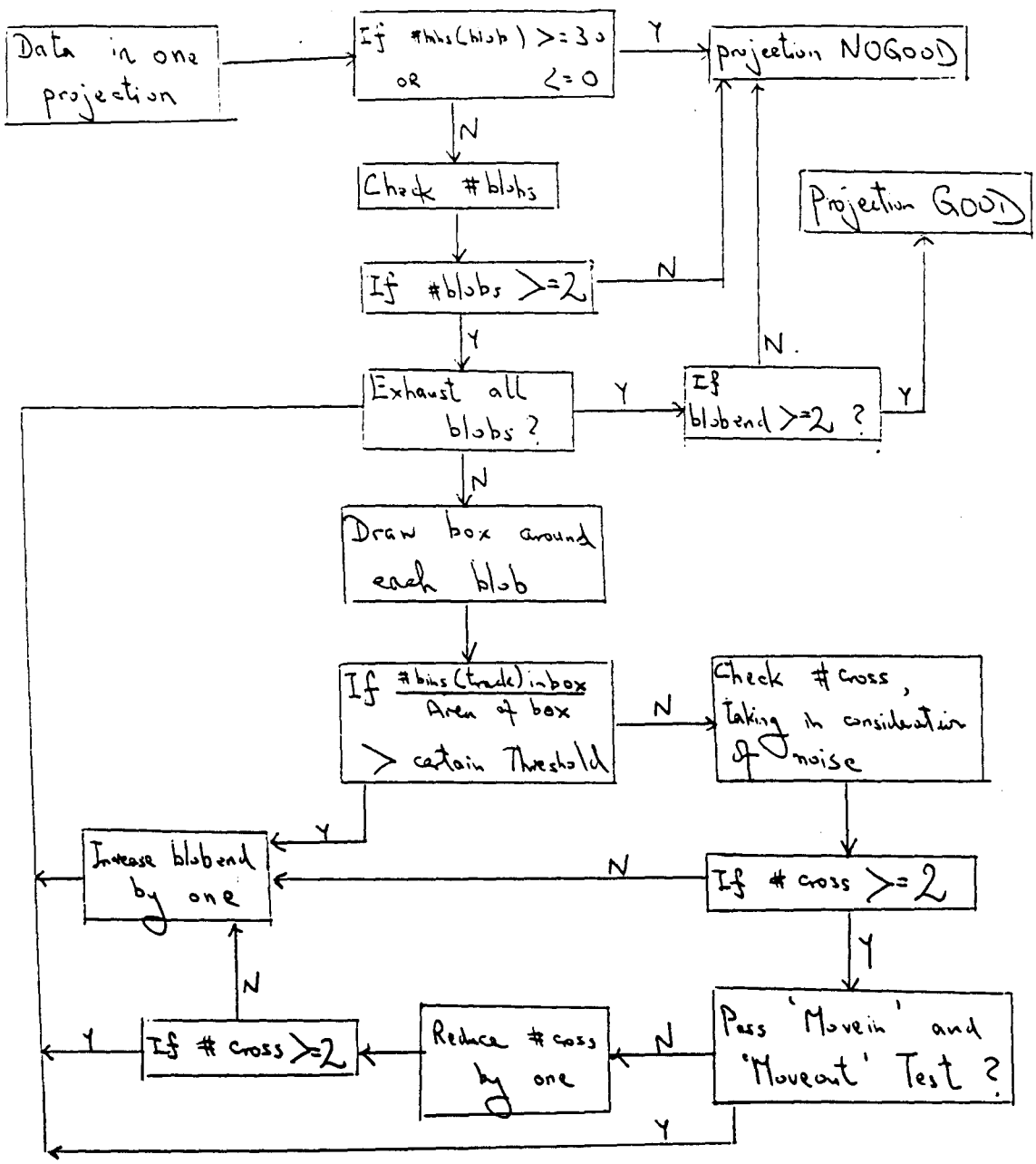

Figure A4.1 The flow chart for algorithm "boxcheck."

APPENDIX 5

EVALUATION OF UPPER LIMITS FOR SIGNALS

In a certain experiment, let S, B and C be the signal, background and the actual number of counts observed, respectively. In some cases (like searches for double beta decay), one does not observe a peak of statistical significance at the range of interest, and would like to evaluate an upper limit for S. The first step is to determine the probability distribution function (p.d.f.) of S given C[59], which by Bayes theorem[60], can be written as

$$g(S|C) = N\,P(C|S)\,P(S),$$

where N is a normalization constant to make

$$\int g(S|C)\,dS = 1\,.$$

In the formula, $P(S)$ is the p.d.f. of S prior to the experiment. Usually, one has no prior knowledge of S except that it cannot be negative, so that

$$P(S) = \begin{cases} 0 & \text{if } S < 0 \\ 1 & \text{if } S \geq 0 \end{cases}.$$

The p.d.f. of observing C counts given a signal S is $P(C|S)$, and can be described by Poisson statistics with mean $(S+B)$

$$P(C|S) = P(C; S+B) = \frac{e^{-(S+B)}(S+B)^C}{C!}.$$

Therefore the p.d.f. of S is

$$g(S) = g(S|C) = N\,\frac{e^{-(S+B)}(S+B)^C}{C!} \quad \text{for } S \geq 0\,.$$

This expression is valid only if the background B is known accurately (through, for instance, Monte Carlo or control experiments). If this is not the case, the formula must be modified to

$$g(S) = N \int_0^\infty \frac{e^{-(S+B)}(S+B)^C}{C!} f(B)\, dB \quad \text{for } S \geq 0\,.$$

where $f(B)$ is the background p.d.f.

With the knowledge of $g(S)$, the upper limit of the signal S_u at a confidence level CL can be evaluated through

$$1 - CL = \int_{S_u}^\infty g(S)\, dS\,.$$

For illustration, two special cases are considered here.

Case I: C is small (< 10), and $f(B)$ is approximated to a delta function centered at $B = B_0$. Then

$$1 - CL = \frac{\displaystyle\int_{S_u}^\infty \frac{e^{-(S+B_0)}(S+B_0)^C}{C!}\, dS}{\displaystyle\int_0^\infty \frac{e^{-(S+B_0)}(S+B_0)^C}{C!}\, dS}\,.$$

Upon integration, it can be shown that the above formula can be expressed in the equivalent form quoted in Particle Data Table[48]

$$1 - CL = \frac{e^{-(S_u+B_0)} \displaystyle\sum_{r=0}^{C} \frac{(S_u+B_0)^r}{r!}}{e^{-B_0} \displaystyle\sum_{r=0}^{C} \frac{{B_0}^r}{r!}}\,.$$

Figure A5.1 shows the relationship between S_u at $CL = 90\%$ with B_0 and C. In the extreme case where $C = 0$, one gets $S_u = 2.30$ at 90% confidence level, independent of B_0. This means that whatever the experimental results may be, one can never conclude that a signal does not exist.

Case II: For large C (> 10), Gaussian approximation can be used. Furthermore, if $f(B)$ follows a Gaussian distribution with mean B_0 and standard deviation σ_B, one gets

$$g(S) \simeq \frac{N}{\sqrt{2\pi}\sigma} e^{-(S-\bar{S})^2/2\sigma^2},$$

where $\bar{S} = C - B_0$, and $\sigma^2 = \sigma_B^2 + C$. Then the relationship between S_u and CL can be readily obtained from the standard table, through the formula

$$1 - CL = \frac{I(\frac{S_u - \bar{S}}{\sigma})}{I(\frac{-\bar{S}}{\sigma})},$$

where $I(z)$ is the error function

$$I(z) = \frac{1}{\sqrt{2\pi}} \int_z^\infty e^{-x^2/2}\, dx\,.$$

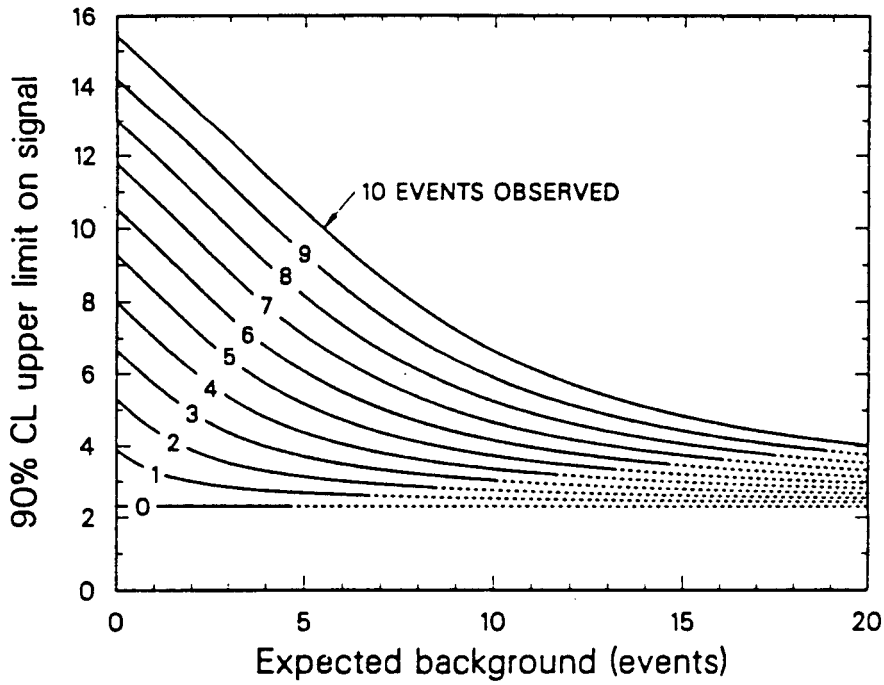

Figure A5.1 The variation of the 90% confidence level of upper limit on signal (S_u) with expected background (B_0) and actual number of events observed (C), for small C in which Poisson statistics are used.

References

1. W. Pauli, in *Letter to the Physical Society of Tubingen*, unpublished (1930); reproduced in L.M. Brown, Physics Today **31**, No. 9, 23 (1978).

2. C.L. Cowan et al., Science **124**, 103 (1956).

3. E. Fernandez, talk presented in *Neutrino '90 Conf.*, CERN (1990).

4. For an overview of the subject, see F. Boehm and P. Vogel, *Physics of Massive Neutrinos*, Cambridge University Press, Cambridge, (1987).

5. For example, see F. Halzen and A.D. Martin, *Quarks and Leptons*, John Wiley & Sons, New York, (1983).

6. J. Wilkerson, talk presented in *Neutrino '90 Conf.*, CERN (1990);
H. Kawakami et al., in *Proc. of the XXIII Yamada Conf. on Nuclear Weak Process and Nuclear Structure, Osaka, Japan, 1989*, World Scientific, Singapore (1989).

7. For example, A. Burrows, in *Fifth Force and Neutrino Physics, Proc. of the XXIII Recontre de Moriond*, eds. O. Fackler and J. Tran Thanh Van, Editions Frontières, Paris (1988).

8. E. Majorana, Nuovo Cimento **14**, 171 (1937);
B. Kayser, Comm. Nucl. Part. Phys. **14**, No. 2, 69 (1985).

9. M. Goeppert-Mayer, Phys. Rev. **48**, 512 (1935);
W.H. Furry, Phys. Rev. **56**, 1148 (1939).

10. For reviews of the subject, see
H. Primakoff and S.P. Rosen, Annu. Rev. Nucl. Part. Sci. **31**, 145 (1981);
W.C. Haxton and G.J. Stephenson Jr., Prog. Part. Nucl. Phys. **12**, 409 (1984);
M. Doi, T. Kotani, and E. Takasugi, Prog. Theor. Phys. Suppl. **83**, 1 (1985).

11. H.M. Georgi, S.L. Glashow, and S. Nussinov, Nucl. Phys. **B193**, 297 (1981).

12. M. Gell-Mann, P. Ramond, and R. Slansky, in *Supergravity*, eds. P. van Nieuwenhuizen and D.Z. Freedman, Amsterdam, North Holland (1979).

13. For example,
W.C. Haxton, S.P. Rosen, and G.J. Stepenson Jr., Phys. Rev. **D26**, 1805 (1982);
T. Tomoda, and A. Faessler, Phys. Lett. **B199**, 475 (1988);
J. Engel, P. Vogel, and M.R. Zirnbauer, Phys. Rev. **C37**, 731 (1988);
J. Engel et al.,Phys. Lett. **B225**, 5 (1989);
K. Muto, E. Bender, and H.V. Klapdor, Z. Phys. **A334**, 177 & 187 (1988).

14. T. Kirsten, in *Proc. of the Int. Symp. on Nuclear Beta Decay and Neutrinos, Osaka, Japan, 1986*, eds. T. Kotani, H. Ejiri, and E. Takasugi, World Scientific, Singapore (1986);
O.K. Manuel, in *Proc. of the Int. Symp. on Nuclear Beta Decay and Neutrinos, Osaka, Japan, 1986*, eds. T. Kotani, H. Ejiri, and E. Takasugi, World Scientific, Singapore (1986);
K. Marti and S.V.S. Murty, Phys. Lett. **B163**, 71 (1985).

15. C.A. Levine, A. Ghiorso, and G.T. Seaborg, Phys. Rev. **27**, 296 (1950);
W.C. Haxton, G.A. Cowan, and M. Goldhaber, Phys. Rev. **C28**, 467 (1983).

16. For example,
D.O. Caldwell et al., in *Tests of Fundamental Laws in Physics, Proc. of the XXIV Recontre de Moriond*, eds. O. Fackler and J. Tran Thanh Van, Editions Frontières, Paris (1989);
P. Fisher et al., Phys. Lett. **B218(2)**, 257 (1989);
F.T. Avignone, III et al., Phys. Rev. **C34**, 666 (1986).

17. S.R. Elliott, A.A. Hahn, and M.K. Moe, Phys. Rev. Lett. **56**, 2582 (1986);
S.R. Elliott, A.A. Hahn, and M.K. Moe, Phys. Rev. Lett. **59**, 2020 (1987).

18. M. Alston-Garnjost et al., Phys. Rev. Lett. **63**, 1671 (1989);
A.A. Pomansky et al., in *Tests of Fundamental Laws in Physics, Proc. of the XXIV Recontre de Moriond*, eds. O. Fackler and J. Tran Thanh Van, Editions Frontières, Paris (1989);
M. Moe, talk presented in *Neutrino '90 Conf.*, CERN (1990).

19. G. Charpak et al., Nucl. Instrum. Methods **62**, 235 (1968);
F. Sauli, CERN **77-09** (1977).

20. W.W.M. Allison et al., Nucl. Instrum. Methods **119**, 488 (1974);
W.W.M. Allison and P.R.S. Wright, in *Formulae and Methods in Experimental Data Evaluation*, **2**, E1, eds. R.K. Bock et al., EPS/CERN (1984).

21. D.R. Nygren, **PEP-198** (1975);
A.R. Clark et al., *Proposal for a PEP facility based on the TPC*, **PEP-4** (1976).

22. For various applications of the TPC, see *The Time Projection Chamber*, ed. J.A. Macdonald, AIP Conf. Proc. **108**, New York (1984).

23. G.E. De'Munari and G. Mambriani, Nuovo Cimento **33A**, No. 2, 299 (1976).

24. E. Bellotti et al., in *The Time Projection Chamber*, ed. J.A. Macdonald, AIP Conf. Proc. **108**, New York (1984);
A. Forster et al., in *The Time Projection Chamber*, ed. J.A. Macdonald, AIP Conf. Proc. **108**, New York (1984).

25. F. Boehm and M.Z. Iqbal, in *FestiVal - Festschrift for Val Telegdi*, ed. K. Winter, Amsterdam, North Holland (1988);
H.T. Wong et al., in *Fundamental Symmetries in Nuclei and Particles*, eds. H. Henrikson and P. Vogel, World Scientific, Singapore (1990).

26. M.Z. Iqbal, B.M. O'Callaghan, and H.T. Wong, Nucl. Instrum. Methods **A253**, 278 (1987).

27. A.S. Barabash et al., Nucl. Instrum. Methods **B17**, 450 (1986);
A.S. Barabash et al., Phys Lett. **B223(2)**, 273 (1989).

28. A. Alessandrello et al., Nucl. Instrum. Methods **A252**, 227 (1986);
E. Bellotti et al., Phys. Lett. **B221(2)**, 209 (1989).

29. For example,
K. Masuda et al., Nucl. Instrum. Methods **174**, 439 (1980);
E. Aprile and M. Suzuki, IEEE Trans. Nucl. Sci. **36(1)**, 311 (1989).

30. B.M.G. O'Callaghan, Ph. D. thesis, Caltech (1989).

31. M.Z. Iqbal et al., Nucl. Instrum. Methods **A243**, 459 (1986).

32. H.A. Bethe, Phys. Rev. **89**, 1256 (1953).

33. U. Fano, Ann. Rev. Nucl. Sci. **13**, 1 (1963);
L. Pages et al., Atomic Data Table **4**, 1 (1972).

34. W. Heitler, *The Quantum Theory of Radiation*, pg. 242, Clarendon Press, Oxford (1954);
S.M. Seltzer and M.J. Berger, Atomic Data and Nuclear Data Tables **35**, 345 (1986).

35. C.K. Hargrove et al., Nucl. Instrum. Methods **219**, 461 (1984).

36. A. Peisert and F. Sauli, CERN **84-08** (1984).

37. W.W.M. Allison et al., Nucl. Instrum. Methods **133**, 325 (1976).

38. M. DiStasio and W.C. McHarris, Am. J. Phys. **47(5)**, 440 (1979).

39. M.Z. Iqbal et al., Nucl. Instrum. Methods **A259**, 459 (1987).

40. M.Z. Iqbal, B.M. O'Callaghan, and H.T. Wong, Nucl. Instrum. Methods **A263**, 387 (1988).

41. J. Thomas et al., IEEE Trans. Nucl. Sci. **NS-34**, 845 (1987).

42. H.T. Wong et al., in *Tests of Fundamental Laws in Physics, Proc. of the XXIV Recontre de Moriond*, eds. O. Fackler and J. Tran Thanh Van, Editions Frontières, Paris (1989).

43. C.J. Martoff, talk presented in *Berkeley Workshop on Ultra-Low Radioactive Background Experiment* (1989).

44. J.S. O'Connell and F.J. Schima, Phys. Rev. **D38**, 2277 (1988).

45. P. Fisher, Ph. D. thesis, Caltech (1988).

46. E. Storm and H.I. Israel, Nuclear Data Table **A7**, 565 (1970).

47. J.F. Ziegler and W.K. Chu, Atomic Data and Nuclear Data Tables **13**, 463 (1974).

48. G.P. Yost et al., *Review of Particle Properties*, Phys. Lett. **B204** (1988).

49. G. Giacomelli, talk presented in *Neutrino '90 Conf.*, CERN (1990).

50. M. Calicchio et al., Phys. Lett. **B193(1)**, 131 (1987).

51. C. Broggini, talk presented in *Third Neuchâtel Workshop on Low Count Rate Experiments*, Yverdon (1990).

52. M.B. Voloshin, M.I. Vysotskii and L.B. Okun, Sov. Phys. JETP **64**, 446 (1986).

53. V. Zacek, talk presented in *Third Neuchâtel Workshop on Low Count Rate Experiments*, Yverdon (1990).

54. D. Caldwell, talk presented in *Third Neuchâtel Workshop on Low Count Rate Experiments*, Yverdon (1990).

55. For more examples, see J. Lowell, *Mr. Eliot's Guide to Quantum Theory*, Physics Today **42**, No. 4, 46 (1989).

56. M.A. Preston and R.K. Bhaduri, *Physics of the Nucleus*, pg. 309, Addison-Wesley, Massachusetts (1975).

57. M. Huk, P. Igo-Kemenes, and A. Wagner, Nucl. Instrum. Methods **A267**, 107 (1988).

58. Y. Chiba et al., Nucl. Instrum. Methods **A269**, 171 (1988).

59. O. Helene, Nucl. Instrum. Methods **212**, 319 (1983).

60. For example, see W.T. Eadie et al., in *Statistical Methods in Experimental Physics*, North Holland, Amsterdam (1971).